UNIVERSITY OF SOUTHAMPTON

FACULTY OF ENGINEERING, SCIENCE &
MATHEMATICS

Optoelectronics Research Centre

HIGH-AVERAGE-POWER PLANAR WAVEGUIDE LASERS

by

Jing Wang

Thesis submitted for the Degree of Doctor of Philosophy

July 2007

UNIVERSITY OF SOUTHAMPTON

ABSTRACT

FACULTY OF ENGINEERING, SCIENCE & MATHEMATICS

OPTOELECTRONICS RESEARCH CENTRE

Doctor of Philosophy

HIGH-AVERAGE-POWER PLANAR WAVEGUIDE LASERS

By Jing Wang

Reported in this thesis is some progress towards high-average-power diode-pumped planar waveguide lasers. As a format of the laser active medium, planar waveguides take advantage of their extreme slab geometry, which is compatible with that of high-power diode lasers, offer a great degree of versatility of the pump arrangement, have excellent thermal handling capability, and deliver high optical gains per unit pump power. Pumped with different schemes, three kinds of planar waveguides are investigated herein: direct-bonded double-clad planar waveguides, ion-exchanged tapered waveguides, and thick films fabricated by pulsed laser deposition, of which a double-clad planar waveguide produced laser output power of up to 58W.

The tapered waveguide structure allows diode pumping at its multimode broad channel end and ensures fundamental-mode laser output at the single-mode channel end, with adiabatic operation achievable through careful design of the interconnecting taper. Linear and parabolic taper shapes are compared. The two types of waveguides expanding to various widths over the same lengths were fabricated on the same Nd:BK7 substrate and characterised with Ti:sapphire pumping. The linear tapers show superior operation for larger guiding sizes up to taper widths of 250μm, and therefore are more compatible with high-average-power broad-stripe diode pumping.

Double-clad planar waveguides, fabricated by direct bonding YAG and sapphire, have features that are very attractive in this work: they are ideally suited to high-power diode bar/stack pumping owing to their high *NA* (0.46) slab-like geometry; and they are shown to robustly maintain single-mode operation by gain mode selection. Both diode bars and stacks were used to side-pump a 30μm double-clad Nd:YAG waveguide. For diode-bar pumping, an extended cavity was used to control the output spatial mode in the non-guided axis. Multimode output power larger than 10W was obtained from the waveguide with a slope efficiency of 56%, which was reduced to 33% when the external cavity was optimised for beam quality, obtaining M^2 values of 1.1 (in the guided axis) by 2.8 (in the non-guided axis). For diode-stack pumping, 58W of output power was obtained from a monolithic cavity with a slope efficiency of 62%. With an extended cavity, 20W of output power and a minimum M^2 value of ~7 in the non-guided axis were obtained, although the optimum results were not found as a result of waveguide damage. Further designs are discussed for power scaling to very high powers.

PLD planar waveguides are investigated as a flexible alternative in high-power planar waveguide laser systems. As an initial demonstration, a slope efficiency of 11.2% was obtained from a diode-stack-pumped 50μm Nd:GGG PLD waveguide. The effect of self-imaging was observed with a 27μm Nd:GGG PLD waveguide.

To my brother,

for whom I cannot wait to read this thesis

"Humans have a knack for choosing precisely
the things that are worst for them."

— Prof. A. D

List of Contents

Abstract i

List of Contents iii

List of Figures viii

List of Tables xiii

Author's Declaration xiv

Acknowledgements xv

Symbols and Abbreviations xvi

Chapter 1

Introduction 1

1.1 High-power diode-pumped solid-state lasers 1
- 1.1.1 Pump source 1
- 1.1.2 Active ion and host material 3
- 1.1.3 Thermal considerations 5

1.2 High-power planar waveguide lasers 8
- 1.2.1 Motivations 9
- 1.2.2 Waveguide fabrication 10
- 1.2.3 Pump scheme 11

1.2.4 Historical review 13

1.3 Structure of this thesis 15

1.4 References 16

Chapter 2
Theory 24

2.1 Introduction 24

2.2 Laser performance 24
- 2.2.1 Spatial rate equation analysis 25
  - 2.2.1.1 Mode dependent gain 28
  - 2.2.1.2 Threshold and slope efficiency 29
- 2.2.2 Plane-wave analysis 31
  - 2.2.2.1 Rate of excitation 34
  - 2.2.2.2 Rate of de-excitation 34
  - 2.2.2.3 Slope efficiency and laser threshold 35

2.3 Laser beam quality 36
- 2.3.1 Gaussian beam propagation 36
- 2.3.2 Definition of the M^2 factor 37
- 2.3.3 Defining beam width 38

2.4 Thermal modelling 40
- 2.4.1 Temperature distribution 40
- 2.4.2 Stress distribution 42

2.5 Waveguide theory 43
- 2.5.1 Maxwell’s equations 45
- 2.5.2 A general asymmetric slab waveguide model 47
  - 2.5.2.1 TE modes 47
  - 2.5.2.2 TM modes 49
  - 2.5.2.3 The symmetric slab waveguides 50
- 2.5.3 A graded-index asymmetric waveguide model 51

2.6 References 55

Chapter 3
Tapered waveguide lasers 57

3.1 Introduction 57

3.2 Theoretical study 59
  3.2.1 Tapered waveguide theory 59
  3.2.2 Design of the tapered waveguides 64
  3.2.3 Modelling by the Beam Propagation Method 66

3.3 Fabrication 68
  3.3.1 Thermal ion exchange 68
  3.3.2 Fabrication process 69

3.4 Laser characterisation 73
  3.4.1 Comparison of linear and parabolic tapers 73
    3.4.1.1 Discussion 76
  3.4.2 Broad-stripe diode pumping 78

3.5 Summary 80

3.6 References 82

Chapter 4
A diode-bar side-pumped waveguide laser with an extended cavity 84

4.1 Introduction 84
  4.1.1 Diode pumping of planar waveguides 84
  4.1.2 Diode coupling 85
  4.1.3 Spatial mode control 88

4.2 Mode-selection in double-clad waveguides 90
  4.2.1 Modelling of the propagation modes 90
  4.2.2 Gain mode selection 94

4.3 Laser operation 97
  4.3.1 Extended cavity design 97
  4.3.2 Experimental set-up 99
  4.3.3 Laser characterisation 100
  4.3.4 Discussion 102

4.4 Summary 104

4.5 References 105

Chapter 5

Diode-stack side-pumped planar waveguide lasers 107

5.1 Introduction 107

5.2 Design of coupling optics 109

5.3 Laser operation 114
    5.3.1 Pump and cooling set-up 114
    5.3.2 Laser operation with a monolithic cavity 116
        5.3.2.1 Laser performance 116
        5.3.2.2 Discussion 119
    5.3.3 Laser operation with an extended cavity 121

5.4 Further power scaling expectations for planar waveguide lasers 124
    5.4.1 Laser performance 125
    5.4.2 Thermal characteristics 127

5.5 Summary 128

5.6 References 129

Chapter 6

Diode-stack-pumped pulsed-laser-deposited planar waveguide lasers 130

6.1 Introduction 130

6.2 Fabrication process 131

6.3 Laser operation with diode-stack pumping 133
    6.3.1 Experimental set-up 133
    6.3.2 Laser performance 134
    6.3.3 Discussion 137

6.4 Multimode interference and self-imaging 138
    6.4.1 Theory 138
    6.4.2 Experimental characterisation 139

6.5 Summary 141

6.6 References 142

Chapter 7
Conclusions and future work 143

7.1 Conclusions 143
    7.1.1 Conclusions of the introductory chapters 143
    7.1.2 Conclusions of the experimental chapters 144

7.2 Future work 147
    7.2.1 High-brightness >100W planar waveguide lasers 147
    7.2.2 Towards 1kW planar waveguide lasers 147

7.3 References 148

Appendix A
Publications 149

A.1 Journal articles 149

A.2 Conferences 149

List of Figures

Figure 1.1 Energy level diagram of Nd:YAG lasing at 1064nm. 4

Figure 1.2 Energy level diagram of Yb:YAG laser system. 4

Figure 1.3 Schematic of the heat removal of the four basic host medium geometries: (a) rod, (b) fibre, (c) thin-disk, and (d) slab. 7

Figure 1.4 A typical planar waveguide structure and guiding condition. 8

Figure 1.5 Possible diode-pumping configurations for planar waveguide lasers. 12

Figure 2.1 (a) Idealized energy-level scheme and (b) a practical quasi-three-level energy diagram. 26

Figure 2.2 (a) A quasi-three-level energy scheme for a laser system , (b) Stark level spectroscopy of Yb^{3+} : YAG, and (c) a sketch for the processes of excitation and de-excitation of the lasing ions in the laser medium for an Yb^{3+} : YAG laser. 32

Figure 2.3 A linear slope efficiency diagram, where the slope efficiency is the gradient with P_{out} plotted against P_p. 33

Figure 2.4 The geometries of imbedded Gaussian beam and multimode beam. 37

Figure 2.5 Schematic structure of a diode-side-pumped double-clad waveguide laser which has a one-dimensional temperature profile. 40

Figure 2.6 Basic structure of an optical waveguide. 44

Figure 2.7 Planar optical waveguide structure. 46

Figure 2.8 An asymmetric waveguide structure. 47

Figure 2.9 Permittivity (refractive index) profile of (a) a step-index waveguide structure and (b) a graded-index asymmetric waveguide structure........... 51

Figure 2.10 Ray path through a graded-index asymmetric waveguide. χ_A and χ_B are the boundary positions along the y-axis where the ray is parallel to the z-axis [20].. 52

Figure 3.1 Schematic diagram of a tapered waveguide. 57

Figure 3.2 Ray path within a two-dimensional tapered waveguide........................... 59

Figure 3.3 Rate of change of waveguide width with the taper angle......................... 62

Figure 3.4 A schematic diagram for the linear tapered waveguide structure. 63

Figure 3.5 One round-trip of (a) the linear tapered waveguide structure and (b) the refractive-index profile applied in the BPM modelling. 66

Figure 3.6 Evolution of the intensity in the one round-trip through the tapered waveguide, with higher intensities denoted by whiter colours. 67

Figure 3.7 Fabrication procedure.. 70

Figure 3.8 Cleaning procedure... 71

Figure 3.9 Top view of the experimental cavity set-up for the Ti:sapphire pumped channel and tapered waveguide lasers... 74

Figure 3.10 Absorbed pump power threshold against maximum taper width for the linear and parabolic tapered-waveguide lasers, alongside the standard channel waveguide lasers. 75

Figure 3.11 Slope efficiency against maximum taper width for the linear and parabolic tapered- waveguide lasers, alongside the standard channel waveguide lasers... 76

Figure 3.12 Imaged mode profiles for the 200μm-wide linear (upper) and parabolic (lower) tapers.. 77

Figure 4.1 Typical pump configuration of a diode end-pumped waveguide laser: (a) coupling scheme for the diode “slow” axis, and (b) for the “fast” axis. ... 87

Figure 4.2 Schematic representation of diode to waveguide proximity coupling. 88

Figure 4.3 Schematic of double-clad planar waveguide structure............................. 89

Figure 4.4 Cross-section comparison of a "classical" single-mode double-clad fiber and a large-mode-area double-clad planar waveguide. 89

Figure 4.5 Schematic structure of a double-clad planar waveguide. 91

Figure 4.6 One-dimensional step-function doping of a double-clad planar waveguide, with the doping ratio t_{core}/t_{w}. 95

Figure 4.7 Relative gain for the first four guided modes at 1064nm against doping fraction for a resonating one-directional power 100 times greater than the saturation power. 96

Figure 4.8 Doping fraction at which the gain for mode 1 becomes equal to that for mode 0, relative to value of I/I_{sat}. 96

Figure 4.9 Extended stable cavity resonator design. 97

Figure 4.10 A computer modelling on the real lens extended cavity with two cylindrical lenses, showing beam radii for the two axes with the change of the cavity length. 98

Figure 4.11 Pump set-up of a diode-bar side-pumped Nd:YAG double-clad planar waveguide laser. 99

Figure 4.12 Output beam quality factor against relative position of the output coupler, with T=19% and an optimum cavity length of ~120mm. The inset shows the optimized collimated output captured on a CCD camera. 100

Figure 4.13 Output power against absorbed pumped power for the high-brightness and multimode cavities and an output coupling of R_{oc} = 0.70. 101

Figure 5.1 A photo of a typical diode stack structure with the collimating micro-lenses, downloaded from www.nuvonyx.com. 108

Figure 5.2 (a) Photo and (b) schematic for the collimated diode stack structure. 109

Figure 5.3 Procedure of the design of the diode-stack-to-waveguide coupling optics. 110

Figure 5.4 Two lens combination models on the y-axis of the diode and the beam size results given by Zemax. The two lens combinations are: (a) Doublet lens (focal length=60mm) + Cylindrical lens (f=4mm), and (b) Four cylindrical lens with focal lengths 300mm, 100mm, 12.7mm and 4mm from left to right. 111

Figure 5.5 (a) Schematic of coupling optics on the y-axis and waveguide cooling scheme, and (b) coupling optics on the x-axis, for the diode-stack double-side-pumped waveguide laser; (c) the double-clad waveguide structure with the dimensions; and finally (d) a photo of the set-up. 115

Figure 5.6 The 30μm Nd:YAG waveguide laser output power versus incident pump power with single-side pumping from two diode stacks No.1 and No.2, respectively. 117

Figure 5.7 The 30μm Nd:YAG waveguide laser output power versus absorbed pump power with double-side pumping from two diode stacks. 117

Figure 5.8 Some typical areas observed under microscope on (a) the HR-mirror-attached end face, and (b) the 20%-output-coupler end face of the waveguide after the upper sapphire cladding layer dropped off from the rest of the waveguide. 119

Figure 5.9 Schematic of the extended cavity configuration combined with the stack pumping. 121

Figure 5.10 Modelling of the spherical+cylindrical lens extended cavity, showing beam radii for the two axes of the waveguide with the change of the cavity length. 122

Figure 5.11 The output power against absorbed pump power of the diode-stack-pumped 30μm Nd:YAG Waveguide laser with a stable extended cavity. 123

Figure 5.12 Some typical areas on (a) the HR-mirror-attached end face, and (b) the AR-coated end face of the waveguide after laser operation with an extended cavity. 124

Figure 5.13 Design of the 50μm Yb:YAG planar waveguide structure. 125

Figure 5.14 Theoretical modelling on the laser performance of an 50μm Yb:YAG planar waveguide laser pumped by two diode stacks with maximum incident power of 360W. 126

Figure 6.1 Experimental set-up of the PLD chamber apparatus [1]. 132

Figure 6.2 Experimental arrangement for the pump configuration and laser output analysis for the diode-stack end-pumped 50μm-thick Nd:GGG PLD waveguide laser. 133

Figure 6.3 The 50μm Nd:GGG PLD waveguide laser output power versus absorbed pump power by diode-stack end pumping with a R_{oc}=0.8714 output coupler. 136

Figure 6.4 Output beam profile of the 50μm Nd:GGG PLD waveguide laser pumped by a three-bar diode stack... 136

Figure 6.5 Findlay-Clay plot according to the laser threshold measurements of the 50μm Nd:GGG PLD waveguide laser, to estimate the propagation losses. 137

Figure 6.6 Theoretical plot for the field amplitude contours of a self-imaging multimode symmetric step-index Nd:GGG/YAG waveguide of depth 50μm, with an axially symmetric input beam.. 139

Figure 6.7 Schematic of the experimental set-up of the self-imaging effect observing. 139

Figure 6.8 Beam profile of (a) multimode propagation through the Nd:GGG waveguide, and (b) self-imaging propagation through the waveguide when the propagation parameters satisfied the self-imaging condition............ 140

List of Tables

Table 3.1 Design features of the photolithographic mask: linear and parabolic tapers. 65

Table 3.2 Summary of laser performance for the three types of waveguides........... 76

Table 3.3 Design features of sample LT and sample BC.. 78

Table 3.4 Slope efficiency results and spatial overlap calculation of sample LT and sample BC. 79

Table 5.1 A comparison of the experimental results and Zemax modeling on the optimum lens combination for the diode-stack beam focusing, alongside the power delivery efficiency through a 50µm aperture and a 30µm aperture, respectively... 113

Table 5.2 Yb:YAG laser model parameters.. 125

Table 5.3 Thermal parameters used in the Yb:YAG waveguide model described.. 127

Table 6.1 Absorbed pump power threshold with different output coupler transmissions. 135

Table 7.1 The key parameters applied in the experimental chapters (Chapter 3 – 6) relating to the main considerations for developing a high-average-power planar waveguide laser that were introduced in Chapter 1. 144

Author's Declaration

I, **Jing Wang**, declare that the thesis entitled *High-Average-Power Planar Waveguide Lasers* and the work presented in it are my own. I confirm that:

- this work was done wholly or mainly while in candidature for a research degree at the University of Southampton;
- where any part of this thesis has previously been submitted for a degree or any other qualification at this University or any other institution, this has been clearly stated;
- where I have consulted the published work of others, this is always clearly attributed;
- where I have quoted from the work of others, the source is always given. With the exception of such quotations, this thesis is entirely my own work;
- I have acknowledged all main sources of help;
- where the thesis is based on work done by myself jointly with others, I have made clear exactly what was done by others and what I have contributed myself;
- parts of this work have been published (see Appendix A for details).

Signed: ………………………… Date: …………………………

Acknowledgements

Here it comes finally. I've been looking forward to writing this page for years by now, but when the day arrives, I start to realize the difficulty to squeeze everyone that has helped me into one page. Thus first I'd like to say: to each of you, I do feel very grateful.

I'd like to thank my supervisor Dave for being so helpful with my work, being patient with my stupidity, being understanding when I met difficulties during the thesis writing, and never been angry with me even when I broke the waveguide. Thanks to Dave for being a perfect supervisor in every student's dream and choosing me in the first place!

I'd like to thank Jacob for being there helping me throughout the project and being able to give me a smile every time I walked into his office with emergency panic. Thanks also to Cheng and Simon for guiding me in the labs during my first year, which, believe me, is not the easiest job in the world. Thanks to Tim for providing his excellent waveguides and working with me in the labs. Thanks to all of the technicians for making things for me and teaching me "lab English" such like "screwdriver" and "allen key", and in particular thanks to Simon who taught me how to use Autocad and Dave for helping me in the cleanroom. Thanks also go to everyone else at the ORC who helped to make my work possible.

I'd like to thank Yoong for being such a good friend and thank ORC for giving me the chance to know her. Thanks also to my office mates for giving me such a pleasant office to work in. Special thanks to Francesca for helping to print, bind and submit the thesis. Thanks to Lingqian for sending me all the food parcels from China. Thanks also go to Huizhi for all the international phone calls she made to me and listening to me no matter what.

I'd like to thank my family for being my most important reason to go on these years. Thanks to my mother for giving me love, courage, and faith, and to my father for letting me see the optimistic attitude in life. Finally, thanks to my husband Hua for being supportive from beginning to end, and for being the miracle of my life.

Symbols and Abbreviations

1D	One-dimensional
A_1 - A_5	Constants
AR	Anti-reflection
ASE	Amplified spontaneous emission
b and b'	Normalised mode effective indices
BPM, FD-BPM, and FFT-BPM	Beam propagation method, finite difference method, and fast Fourier transformation method
c	Speed of light in vacuum
CW	Continuous wave
d_1 - d_4	Depths
d_{core}	Depth of the doped region
d_x and d_y	Decay of the index profile in the lateral and depth directions respectively
$d(x,y,z)$	Normalized doping profile in the laser medium
D	Diameter
D_v and D_e	"Variance" diameter and "$1/e^2$" diameter
DI	Deionised
E	Electric field
E_x, E_y, and E_z	x, y, and z-components of the electric field respectively
E_Y	Young's modulus
$E(x,y)$	x and y dependence of the electric field function of a guided mode
f	Sum of the occupation factors for the lower (f_1) and upper (f_2) laser Stark levels
f_1 and f_2	Occupation factors for the lower and upper laser Stark levels respectively

f_L^l	Final laser Stark level Boltzmann occupation factor
f_L^p	Initial pump Stark level Boltzmann occupation factor
f_U^l	Initial laser Stark level Boltzmann occupation factor
f_U^p	Terminal pump Stark level Boltzmann occupation factor
F_s	Safety factor (to express the fracture possibility of the host material)
F_A	Fraction of pump power absorbed in a single pass through the width of the laser medium
F_B	Fraction of laser power "absorbed" in a single pass along the length of the laser medium
G_p	Gain for the p^{th} laser mode with spatial distribution ϕ_p
G_{rel}	Relative gain for the p$^{\text{th}}$ laser mode
GGG	Gadolinium gallium garnet ($Gd_3Ga_5O_{12}$)
h	Planck's constant
H	Magnetic field
H_x, H_y, and H_z	x, y, and z-components of the magnetic field respectively
$H(x,y)$	x and y dependence of the magnetic field function of a guided mode
HR	High-reflection
$I(x)$ and $I(y)$	Intensity distribution across the transverse co-ordinates x and y respectively
k_0	Wave vector in free space
k_{2y} and k_{1y}	y-axis wave vector within the waveguide core in Chapter 2 and 4 respectively
k_s, k_y, and k_{dy}	Thermal conductivity of the layers of sapphire, YAG, and doped-YAG respectively
k_z, $k(y)$, and $k_y(y)$	z-axis wave vector, y dependence of the wave vector, and y dependence of the y-axis wave vector respectively
$k(x,y,z)$	Thermal conductivity
l	Length of the laser medium
L	Taper length, in Chapter 3 Round-trip loss exponent, in the rest of the thesis
L_{SI}	Self-image period length
M^2	Beam propagation factor
M_x^2	x-axis beam quality

M_y^2	y-axis beam quality
MMI	Multimode interference
MOPA	Master oscillator - power amplifier
n	Refractive index of the laser medium at the laser wavelength
n_0 - n_5	Refractive indices of different waveguide regions, as defined in respective chapters
n_1^0	Total population in the lower laser level at thermal equilibrium
n_{core} and $n_{cladding}$	Refractive indices of the waveguide core and cladding layers respectively
n'_{eff}	Effective index of the fundamental mode in the channel waveguide with finite width W
n_{eff}	Effective index of the fundamental mode within a planar waveguide of equal depth ($W \to \infty$)
n_A, n_L, and n_U	Active ions in all (n_A) of the laser manifolds, the lower (n_L) and upper (n_U) manifold respectively, in terms of population density
N_1 and N_2	Population density of the lower and upper laser levels respectively
N_1^0	Population density of the lower laser level at thermal equilibrium
N_L and N_U	Total population density of the lower and upper manifolds respectively
N_U^l	Integrated inversion density with respect to the laser crystal length and referenced to the Stark levels coupled by the laser radiation
N_U^p	Integrated inversion density with respect to the laser crystal width and referenced to the Stark levels coupled by the pump radiation
NA	Numerical aperture
OC	Output coupler
P_{abs}	Absorbed power
P_{cav}	Laser power in the cavity
P_h	Uniformly deposited heat
P_{in}	Incident power
P_l	Laser power travelling in one direction inside the laser cavity
P_p, P_{th}, and P_{out}	Laser pump power, threshold pump power and output power
P_{tl}	Thermal load produced by the waveguide core due to quantum defect

PLD	Pulsed laser deposition
PWL	Planar waveguide laser
$q(z)$	Complex beam parameter (as a function of z)
$Q_T(x,y,z)$	Thermal power loading per unit volume
$r_p(x,y,z)$	Normalised pump energy distribution
R	Total pump rate
R_{de-ex}	De-excitation rate of the lasing ions for a double pass in the gain medium
R_{ex}	Rate at which ions are excited into the upper laser manifold by the pumping process
R_{oc}	Reflectivity of the output coupler at the laser wavelength
R_s	Thermal shock parameter
R_{sy} and R_{ss}	Thermal shock parameters of YAG and sapphire respectively
$R(z)$	Radius of wavefront curvature (as a function of z)
RE	Rare earth
S	Degree of saturation caused by the intra-cavity laser power
t_{core}	Waveguide core thickness
t_w	Waveguide thickness
T_a	Average temperature
T_{htsk1} and T_{htsk2}	Fixed temperatures of the lower and upper heat sinks respectively
T_{oc}	Transmission of the output coupler
T_{ow}	One-way cavity transmission
$T(x,y,z)$	Temperature distribution
TE	Transverse electric
TIE	Thermal ion exchange
TIR	Total internal reflection
TM	Transverse magnetic
UV	Ultraviolet
V and V'	Normalised guide widths
w_0 and W_0	Waist radii of the fundamental and higher-order-mode beams respectively
w_c	Width of the laser medium crystal
$w(z)$ and $W(z)$	Spot radii of the fundamental and higher-order-mode beams respectively (as a function of z)
W	Channel waveguide width

W_0 and $W_{\max}$	Initial channel width and maximum taper width of the tapered waveguide
$W_l(z)$, and $W_p(z)$	Widths of the linear and parabolic tapers respectively (as a function of z)
W_x and W_y	Beam sizes of higher-order modes in the x and y directions respectively
YAG	Yttrium aluminium garnet ($Y_3Al_5O_{12}$)
α	Structure expansion coefficient
α_{1y} - α_{5y}	Decay coefficients in regions 1 to 5 of the waveguide
α_p	Absorption coefficient of the laser medium at the pump wavelength
α_L	Propagation loss coefficient
α_T	Thermal expansion coefficient
γ	Additional round-trip loss as a result of the taper structure
δ	Background propagation loss coefficient
Δn	Refractive index difference
ΔN^0	Population-inversion density at thermal equilibrium
$\Delta N(x,y,z)$	Population-inversion density
ε	Electric permittivity
ε_0	Electric permittivity in free space
ε_1 - ε_5	Electric permittivity of regions 1 to 5
η_a	Absorption efficiency (fraction of incident pump power absorbed in the laser medium of length l with absorption coefficient α_p)
η_{del}	Pump delivery efficiency
η_{lo}	Laser overlap with the doped region of the laser medium
η_{mode}	Fill factor of the laser beam with respect to the laser gain cross-sectional area
η_{pl}	Spatial overlap of the pump and laser beams inside the laser medium
η_{po}	Pump overlap with the doped region of the laser medium
η_{slope}	Laser slope efficiency
η_L	Launch efficiency
θ	Beam divergence angle of the fundamental-mode beam
θ_i, θ_g, θ_c, and	Incident angle, guidance angle, critical angle, and maximum acceptance angle respectively

$\theta_{\max}$	
θ_p	Projection angle of the ray of the fundamental mode in the waveguide plane
θ_t	Angle of the taper barrier with the z -axis
Θ	Beam divergence angle of higher-order-mode beams
λ	Wavelength
λ_0	Free-space wavelength
λ_{htsk1} and λ_{htsk2}	Surface heat transfer coefficients of the lower and upper heat sinks respectively
λ_l and λ_p	Wavelengths of the laser and pump radiation respectively
μ	Magnetic permeability
μ_0	Magnetic permeability in free space
μ_1 - μ_5	Magnetic permeability of regions 1 to 5
ν	Poisson's ratio
ν_l and ν_p	Frequencies of the laser and pump radiation respectively
σ	Gain cross section
σ_l	Spectroscopic laser emission cross section
σ_p	Spectroscopic pump absorption cross section
σ_s and $\sigma_{\max}$	Surface stress and stress fracture limit that can be tolerated by the laser host material prior to fracture
σ_x and σ_y	"Variance" width across the transverse co-ordinates x and y respectively
τ	Lifetime of the upper laser-level manifold
τ_{eff}	Effective emission lifetime of the upper laser level
$\phi_0(x,y,z)$	Normalised laser photon distribution
ϕ_p	Normalised spatial distribution of the p^{th} laser mode
ϕ_U and ϕ_L	Phase delays for plane waves propagating through the upper and lower half of the waveguide
Φ	Total cavity photon number
χ_A and χ_B	Effective boundaries
ψ and ψ'	Phase offset
ω	Angular frequency
ω_p and ω_l	Gaussian beam radii for the pump and laser cavity modes respectively

Chapter 1

Introduction

1.1 High-power diode-pumped solid-state lasers

There has been a significant enhancement in the field of high-power solid-state lasers in recent years, largely due to the development of reliable and cheap laser diodes as pump sources with more and more choices of wavelengths and power since the late 1980s [1-3]. The result is compact, efficient and robust laser sources which are attractive in the scientific, industrial, medical and military fields. Solid-state lasers operating at high power from ~1W to ~2kW have been demonstrated with different pumping schemes (end pumping, side pumping, and face pumping), various formats (rods, slabs, thin disks, waveguides, and fibres) for different active media and cavity designs [4-16].

This thesis describes the progress leading to higher-average-power diode-pumped planar waveguide lasers, which take advantage of the slab-like geometry of the planar waveguides. To gain an insight into the motivations and directions of the research, it is useful to start with some key parameters for developing a high-average-power solid-state laser.

1.1.1 Pump source

The growth in the technology of solid-state lasers demands more powerful, efficient, and rugged pump sources with better beam quality. Compared to the conventional lamp pumps, diode lasers are attractive for many reasons, primarily based on increased system efficiency, narrower spectral emission, longer lifetime, reliability, and highly improved output beam quality [17]. Their efficiencies of more than 50% [18] make diode lasers ideal pump sources for solid-state lasers. Moreover, the pump wavelength is selective and can be tuned to precisely match the peak absorption of the active ions, thus reducing the heat load which results from the difference between the pump and laser wavelength and significantly increasing the solid-laser system efficiency and beam quality. Diode lifetime can be on the order of 10^4 hours in continuous wave (CW) operation [19], compared to less than 1000 hours for the lifetime of flash lamps, which enables a reliable laser system. One characteristic feature of diode lasers in contrast to lamps is that their radiation can be focused rather easily to spatially match the solid-state laser mode. Solid-state lasers may be in the form of various geometric configurations: a rigid cylindrical rod, a slab, or an optical fibre, while diode lasers can lend themselves very well as pump sources in all these cases. The good overlap between the pump radiation and the laser mode volume again leads to the high overall system efficiency.

Compared to diode-pumped solid-state lasers, the direct use of diodes gives output with broader linewidth, lower peak powers, and lower brightness, limiting many applications, although it should be noted that they can be directly used in applications such as surface hardening or soldering which need only a moderate power density, about 10^4 W/cm^2, within a relatively broad focal area [20].

There are standard commercial designs available for diode lasers, which include broad-stripe single emitters with a length of 100 or 200μm, 1-cm long emitter arrays known as diode bars, and two dimensional stacked arrays (i.e. diode stacks) [21]. One can select a pump source among them according to the output-power requirement of the laser and the particular pump configuration chosen. The diode bars and diode stacks are applied in the work described in this thesis because their geometries are easily compatible with those of the planar waveguides and can provide adequate pump power – up to >50W per 1-cm bar currently [22] - and reasonable beam quality.

1.1.2 Active ion and host material

With the pump source available, a proper active medium must be chosen, which should provide sharp fluorescent lines, strong absorption, and reasonably high quantum efficiency along with good optical and thermo-mechanical properties.

As mentioned in the last section, the emission wavelengths of diode lasers can be adjusted to match the peak absorption of important solid-state laser ions including, for instance, Nd^{3+} [23, 24], Er^{3+} [25, 26], Tm^{3+} [27, 28], Cr^{3+} [29, 30] and Yb^{3+} [31-33], depending on what laser wavelength is required. Rare earth (RE) ions are used in solid-state lasers as the active ions because of their sharp fluorescent transitions covering much of the near-infrared portions of the electromagnetic spectrum [34], trivalent ions being the most commonly used. The characteristic feature of RE^{3+} ions is that their fluorescence spectra arise from electronic transitions between levels of the partially filled 4*f* electron subshell, which is well shielded by the filled 5*s* and 5*p* outer shells. Electrons present in the 4*f* shell can be raised by the light absorption into unoccupied 4*f* levels.

Nd^{3+} is an excellent dopant for diode-pumped solid-state lasers and remains one of the most important elements among trivalent rare earth ions. The principle host materials are yttrium aluminium garnet $Y_3Al_5O_{12}$ (YAG) and glass, where stimulated emission is gained at a number of frequencies within four spectral regions centred at 0.94, 1.06, 1.35, and 1.83μm [34], due to the $^4F_{3/2} \rightarrow {}^4I_{9/2}$, $^4I_{11/2}$, $^4I_{13/2}$, $^4I_{15/2}$ transitions, respectively. The 4-level transition $^4F_{3/2} \rightarrow {}^4I_{11/2}$ is the one that will be discussed in later chapters, and is shown in Fig. 1.1.

The Yb^{3+} ion has a very simple energy level diagram (see Fig. 1.2) that consists of the $^2F_{7/2}$ ground state and $^2F_{5/2}$ excited state manifolds separated by about 10,000 cm^{-1}. The pumping scheme shown in Fig. 1.2 leads to a smaller quantum defect (see section 1.1.4), and consequently lower thermal loading [35-37], as compared to the Nd:YAG laser system discussed above, which makes the Yb^{3+} ion a promising alternative to the Nd^{3+} ion for high-power laser applications [22, 38]. Therefore, with the emergence of powerful InGaAs laser diodes emitting at 942 nm, Yb:YAG has been of more and more interest [39] for high-power systems, especially where thermal limitations can be the main consideration.

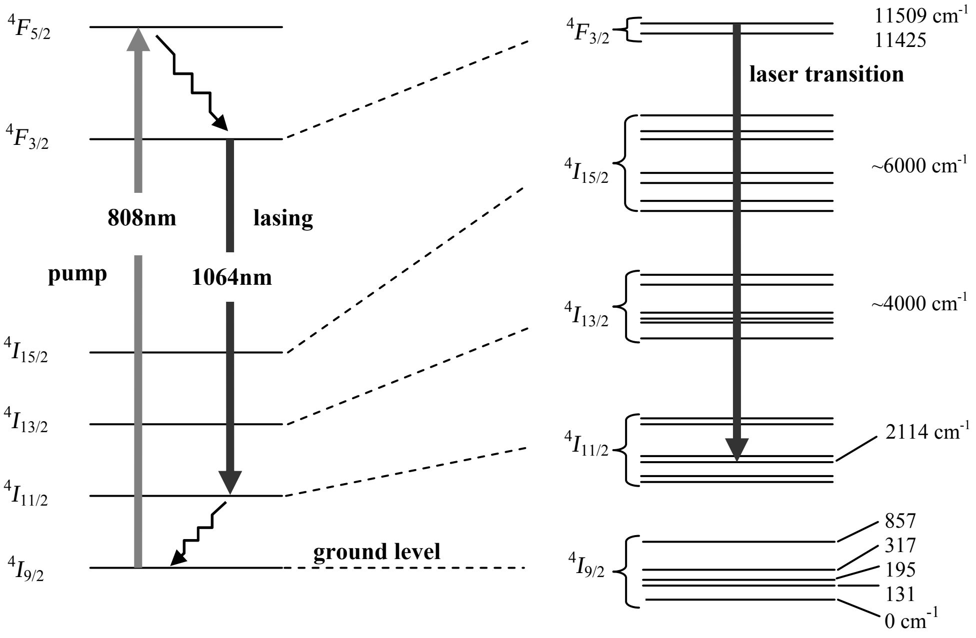

Figure 1.1 Energy level diagram of Nd:YAG lasing at 1064nm.

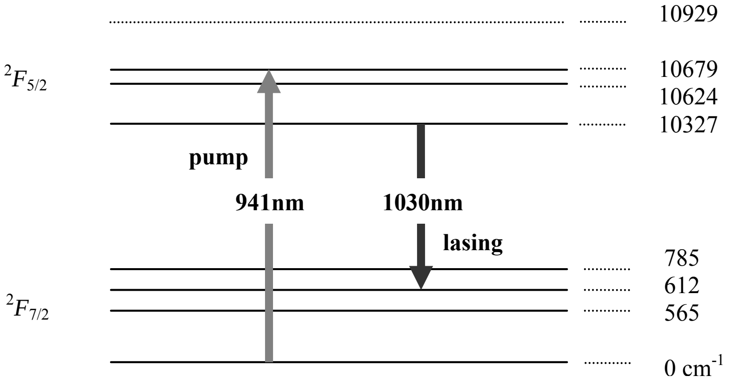

Figure 1.2 Energy level diagram of Yb:YAG laser system.

Other advantages of Yb:YAG are the broad absorption bandwidth (18nm) [40] at the InGaAs wavelength, which is about 10 times broader than the 808nm absorption in Nd:YAG, and that Yb:YAG has a long lifetime of 951μs [34] - about 4 times longer than that of the $^4F_{3/2}$ upper manifold of Nd:YAG. However, it should also be noted that, being a quasi-three-level laser Yb:YAG has higher laser threshold and has to be pumped much higher than threshold to gain an efficient operation.

Solid-state host materials can largely be grouped into crystalline solids and various glasses. To select a host material for a laser ion, optical properties would be the first considerations, avoiding poor beam quality after the beam propagation through the crystal. Most high-average-power laser systems need to take thermal effects into account, so that crystalline materials with high thermal conductance qualities will be a good choice. YAG is a very hard, isotropic crystal and has a good thermal conductivity (with a "thermal shock parameter" R=7.9W/cm [41], for example) and has consequently achieved a position of dominance among solid-state laser host materials.

In this work we will use YAG, glass, and gadolinium gallium garnet $Gd_3Ga_5O_{12}$ (GGG) as host materials, with YAG and GGG used for high-power diode pumping and glass for its cheapness and compatibility with integrated optics.

1.1.3 Thermal considerations

Thermal problems and heat removal are usually a critical issue for designing high-average-power laser systems.

The generation of heat is inevitable in solid-state lasers by the optical excitation process, due to non-radiative transitions inside the gain medium, which is the so-called quantum defect heating. Moreover, in the case of lamp pumping, the broad spectral distribution will cause considerable absorption by the host material, mainly in the ultraviolet and infrared bands [41]. In contrast, diode pumping reduces the heating of the host material by the excellent spectral match between the laser-diode emission and the absorption bands of the active ions. As for Nd:YAG, diode pumping only generates around one quarter of the heat that lamp pumping generates at the same level of power delivered to the upper laser level [42]. However, the heat load can still be significant even with the excitation by diode lasers. For example, the fractional thermal load, i.e. the ratio of generated heat power to the absorbed optical pump power is about 0.3 [43, 44] under conditions of laser extraction for a diode-pumped Nd:YAG laser pumped at 808 nm.

Heat generation takes place in the volume of the gain medium, while surface cooling required for heat extraction functions at the edges, either by a flow of coolant or by the conduction to a heat sink. Therefore, a non-uniform temperature distribution and consequently mechanical stress will occur with the combination of the “hot” laser medium and surrounding cooling devices, which results in a temperature- and stress-dependent variation of the refraction index [41]. Due to this index gradient, the laser beam will be distorted in the laser material, leading to various thermal effects, such as thermal lensing [45-47], stress-induced birefringence [48], and greatly increased surface stress or even fracture [49, 50], etc. These thermally induced problems severely degrade the beam quality and eventually limit the laser output power [51], which makes thermal management an essential part of high-average-power solid-state laser design.

To effectively remove heat from the gain material, sufficient cooling should be applied to the laser system. With reference to cooling techniques, the primary methods include liquid cooling (of which water-cooling is the most commonly used), air or gas cooling, and conductive cooling, which are associated with different host medium geometries. The four basic host medium geometries are the rod, fibre, slab, and thin-disc, the heat removal schematic of which are shown in Fig. 1.3.

The limitations imposed by the conventional rod geometry have long been well known [52] and many techniques were explored to improve the laser performance. For example, thermal lensing can be reduced to some extent by using rods with undoped ends [53, 54] and thermal birefringence produced in the laser rod has to be corrected by insertion of additional optical elements in the laser cavity [55], thus adding to the complexity of the laser cavity. In order to extract the heat more effectively, a higher ratio of cooled surface to the pump volume is preferred. Therefore, starting from the rod cooled at the circumference, two alternative designs emerged: to make the rod very long and thin, leading to fibre lasers [56]; or to make the rod very short with face cooling, resulting in thin-disk lasers [57].

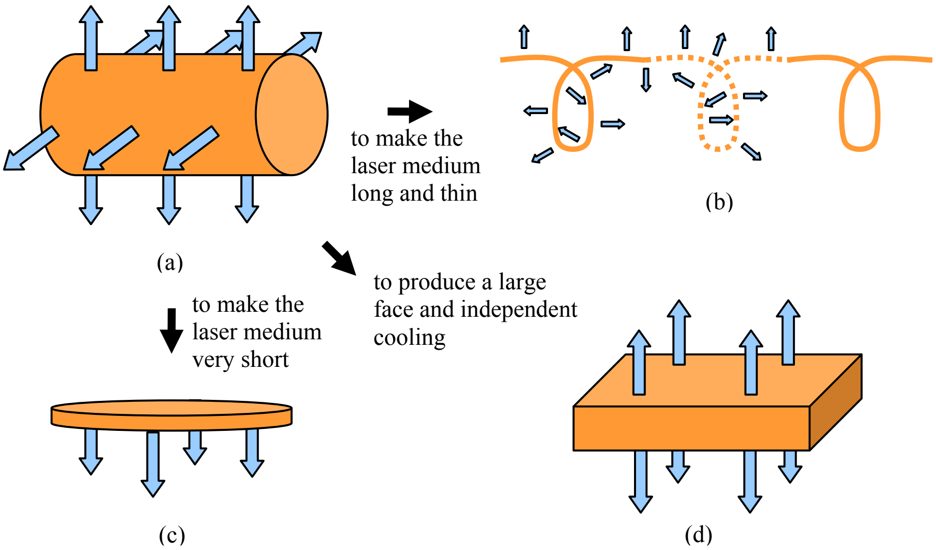

Figure 1.3 Schematic of the heat removal of the four basic host medium geometries: (a) rod, (b) fibre, (c) thin-disk, and (d) slab.

Fibre lasers offer the possibility to overcome the thermal limitations for high-power lasers and to maintain the beam quality. The thermal load caused by the pumping process is spread over a very long region and heat is more efficiently removed, and thus the observed temperature increase in the laser core is small [58] compared to conventional rod lasers. Moreover, the refractive index profile of the fibre is dominantly defined by the geometrical dimensions and the numerical aperture of the waveguide structure itself, so that fibre lasers are nearly immune to the index-related thermal-optical effects. However, coupling optics needs to be chosen carefully, to ensure efficient diode-to-fibre coupling, especially with low-brightness high-power laser diodes.

On the other hand, the basic concept of the thin-disk laser [57] is to use a very thin active medium (thickness about 200µm) with one face mounted closely onto a heat sink. The thin-disk design reduces the pump-volume-to-cooling-surface ratio of the crystal drastically, so that high pump densities can be applied without a high-temperature rise within the crystal. Moreover, the one-dimensional heat flux, which is collinear with the lasing axis, strongly reduces the thermal distortions compared to the rod geometry. As far as the pump configuration is concerned, the pump radiation is imaged onto the disk under oblique angles (to separate it from the laser beam) and needs to multi-pass the disk to exploit the non-absorbed fraction.

The slab lasers take advantage of both the high cooling-surface-to-pump-volume ratio and the one-dimensional temperature gradients in the laser medium. It has been shown that the slab geometry promises a better thermal handling capability [49] compared to the cylindrical rod geometry. The slab structure suggests three possible pump schemes that will be discussed in section 1.2.3, and lends itself well to various solid-state laser systems with different requirements. When it comes to quasi-three-level media, a side pump scheme allows a longer absorption path than the thin disk and hence a lower doping level, which allows greater power scalability [59]. In this work, the planar waveguide, as stated in the next section, has the geometry of an extreme slab and shares the excellent thermal qualities discussed above.

1.2 High-power planar waveguide lasers

Fig. 1.4 shows a typical planar waveguide that might be used for high-power laser operation. The pump and laser light are confined in the RE-doped core, which has higher refractive index than the surrounding substrate and cladding regions.

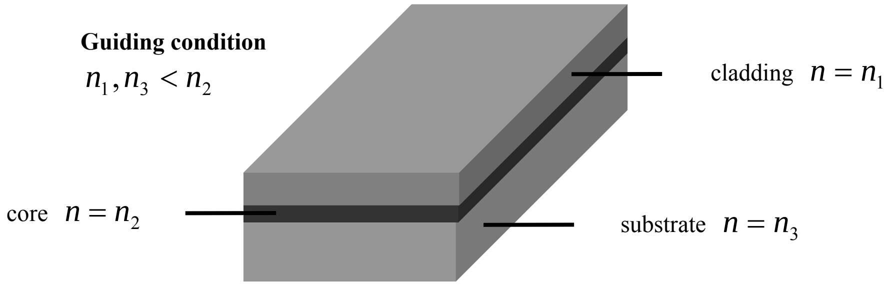

Figure 1.4 A typical planar waveguide structure and guiding condition.

This thesis describes significant progress towards high-average-power diode-pumped planar waveguide lasers.

1.2.1 Motivations

Planar waveguide laser (PWL) devices are of interest for many reasons. For example, planar optical waveguides are the key platform on which to construct integrated optical circuits, with multiple functions such as optical couplers, switches, interferometers, modulators, amplifiers and detectors, etc. Moreover, in recent years [13, 60-63], planar waveguides have been shown to be attractive in high-average-power diode-pumped lasers.

Compared to their bulk counterparts, the optical confinement offered by planar waveguides leads to lowering of the laser threshold pump power, if the waveguide propagation loss is also low, making operation well above lasing threshold achievable for moderate pump powers. The confinement also effectively stops free-space divergence and results in a high pump intensity and therefore a high gain per unit pump power. In addition, the optical guidance dominates the thermal lensing effect in the guided axis, and so the output laser beam quality in this axis is defined by the waveguide structure itself. Furthermore, planar waveguide lasers are very compact, making them convenient for use in many applications where large bulk lasers are not feasible.

As a format of the laser active medium, planar waveguides benefit from their extreme slab geometry. In comparison to bulk and fibre lasers, planar waveguide lasers offer a rectangular pump aperture which is perfectly fitted to the diode-bar geometry, allowing simple coupling optics or even proximity coupling [64] without beam shaping. There is also a greater degree of versatility concerning the pump arrangement, with three possible geometries possible (end-pumping, side-pumping, and face-pumping, see section 1.2.3). With side-pumping, in particular, the slab structure allows unique axes of operation on pumping, lasing and cooling, which leads to a simpler laser system design than thin-disk lasers.

As far as thermal management is concerned, planar waveguides take advantage of their slab structure as well, and have excellent thermal handling capability, which reduces thermally induced problems experienced under high pump powers. Efficient heat removal can be achieved by the effective cooling through the large faces of the waveguide, and the stress fracture limit can be pushed to extreme values [65]. As opposed to the two-dimensional heat flow in bulk and fibre lasers, planar waveguide lasers create one-dimensional heat flow and therefore one-dimensional thermal gradient, which provides well defined birefringence axes avoiding depolarization loss.

It should also be noted that, compared to fibres, planar waveguides can involve almost any type of optical material, whereas fibre materials are mainly limited to types of glass due to fabrication limitations.

1.2.2 Waveguide fabrication

Waveguide fabrication procedures can be broadly grouped into two types: modification of the material refractive index and conjunction of materials with dissimilar refractive indices. The former can be subdivided into techniques such as ion-exchange [66], ion-diffusion [67], ion-implantation [68], and optical writing [69]. As an alternative, waveguides can also be fabricated by the techniques of deposition [70], epitaxial growth [71], and bonding [72]. These latter techniques generally have a stronger capability to produce high numerical aperture (NA) waveguides, which can be preferable for more efficient diode pumping [73], while the former techniques are generally preferred for integrated optical circuits.

Ion exchange has been used to produce a refractive index difference in glass to make waveguides since 1972 [74]. The sample substrate is immersed in a bath of molten salts, so that the alkali ions in the salt bath slowly exchange with the ions in the substrate, leading to a small refractive-index change. The rate of the ion-exchange process can be controlled by the diffusion temperature and the assistance of an electric field across the substrate. Different waveguide patterns (channels, tapers, etc.) can be achieved by using relevant masks, which will be applied to the tapered- waveguide fabrication for diode-stripe-pumped integrated-optics compatible 1W-class waveguide lasers, as discussed in Chapter 3.

To achieve sufficient NA to allow high-power diode bar and diode-stack pumping, co-joining materials with dissimilar refractive index is favoured. An applicable technique is direct bonding [72, 75]. The first step of this fabrication is that the plane surfaces of two pieces of different bulk materials are polished to an optical flatness and free of any dirt or other particles, because they are expected to bond together without the use of any adhesive by Van der Waal's intermolecular forces. To access Van der Waal's forces, the two surfaces have to be brought together within molecular interaction distances, so that high-quality polishing is required to achieve surface flatness figures on the tens to hundreds of nanometre scale. In the case of thermal bonding [76], the process is assisted by a heat treatment. The use of these waveguides for high-power diode bar and diode-stack pumping will be discussed in Chapter 4 and 5, respectively.

Thin film waveguides, fabricated by pulsed laser deposition (PLD) [77], also have the potential for producing garnet waveguides of sufficient NA to allow high-power diode pumping. A pulsed laser (usually at ultra-violet wavelength) is used to ablate a target, and the ejected material forms a plasma plume, which then expands away from the target surface and interacts with the chamber atmosphere until it reaches the substrate where it is deposited as a thin film. In this technique, the substrate can be heated to assist with nucleation and allow crystal growth, and a background gas can be used to help control the film composition. Such waveguides are assessed for their potential for output power scaling with diode-stack pumping in Chapter 6.

1.2.3 Pump scheme

Efficient pump schemes are needed to couple the radiation from a diode laser to the planar waveguide. Three possible pump configurations (face-pumping, side-pumping and end-pumping) are shown in Fig. 1.5, appropriate for the slab/waveguide geometry. These configurations in turn have different requirements on the schemes of diode to crystal coupling: to give focussing in both axes in the case of end-pumping, single axis focussing for side-pumping, and to provide sufficient absorption in face-pumping configurations.

Face pumping, shown in Fig. 1.5.a, lends itself well to high-power diode pumping with multiple diode arrays and permits efficient area-scalable devices pumped by uncollimated or partially collimated laser diode beams, which would result perhaps in the simplest pump design. Nevertheless, due to its low single pass absorption, face pumping requires multipass pump optics to be used, such as a reflective, slotted mirror pump chamber [78] to increase the absorption efficiency, which adds to the complexity of the laser system.

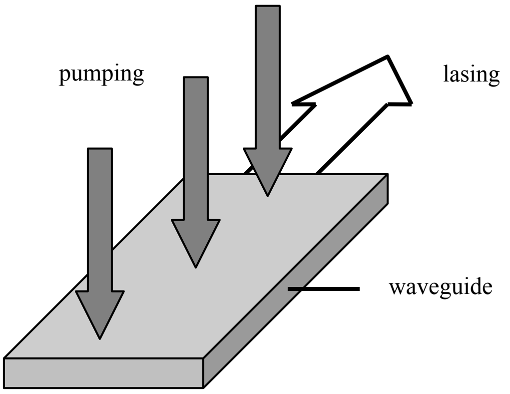

a. face pumping

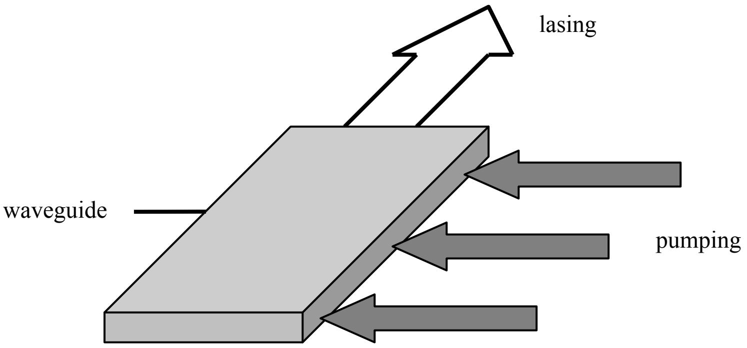

b. side pumping

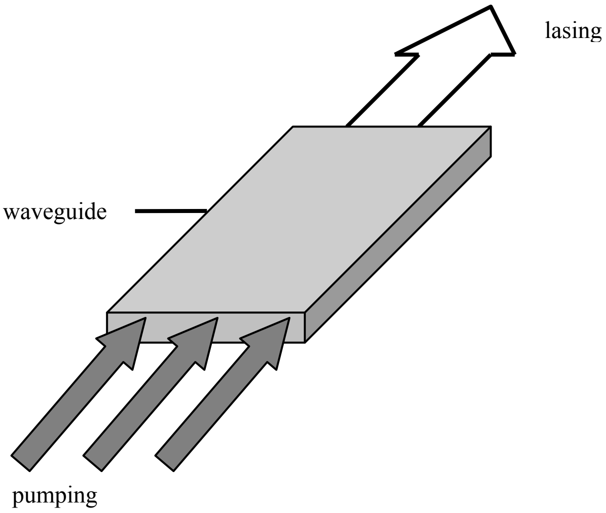

c. end pumping

Figure 1.5 Possible diode-pumping configurations for planar waveguide lasers.

In a side-pumped laser system (Fig. 1.5.b), the pump beam is incident on the edge of the waveguide perpendicular to the laser beam. Side pumping is favoured in some cases, especially in high-average-power systems, where it is rather difficult to deliver an adequate amount of pump power through the small end faces of the laser crystal. A significant advantage of the side-pumped geometry is that power scaling can be simply achieved by increasing the length over which the waveguide is pumped to allow in more pump power, or by pumping from both sides. Furthermore, side pumping uses separate crystal surfaces for pumping, cooling, and laser extraction for individual optimisation, which significantly simplifies the laser system design. The design modelling in ref. [59] shows that edge pumping of quasi-three-level systems is in theory superior to face pumping due to more flexibility in choosing doping level.

End pumping (Fig. 1.5.c) causes the pump radiation to be absorbed along the longitudinal axis of the laser medium, which results in near total absorption of the pump and, therefore, in high laser efficiency. It also has the advantage that good overlap is obtained between the pump volume and the laser mode, leading to improved mode control and beam quality [79], but is limited in terms of power scalability [80] compared to the face and side pumping configurations.

1.2.4 Historical review

The first lasing waveguide structures date back to the 1960’s, when fibres were employed to reduce the threshold in laser systems [81], and in 1971 the first operation of a planar waveguide laser was reported [82]. Since then, a large range of techniques has been applied to the fabrication of waveguides and a host of materials have been studied as the potential active media [71, 83-85].

The contributions to the development of high-average-power diode-pumped waveguide laser systems can be largely divided into two groups by the different schemes of pumping arrangements, in-plane pumping (end and side pumping) and face pumping.

In the case of in-plane pumping, the first diode-side-pumped waveguide laser was reported in 1992 by the researchers at the University of Southampton [86], followed by the first diode-pumped Yb:YAG planar waveguide laser in 1995 [87]. In 1997, with the thermal-bonding technique [72], planar waveguides were fabricated with high numerical aperture, low propagation loss, and good thermal properties that are necessary for high-power diode-bar pumping. A lot of improvements were presented in the following two years in obtaining more average output power and (nearly) diffraction-limited beam quality. In 1998, Bonner *et al.* [88] reported a 6.2W CW PWL from an 80µm-thick multimode Nd:YAG waveguide that was grown via liquid phase epitaxy. The following year [73] a much smaller 8µm-thick Nd:YAG waveguide produced 3.7W output power, fabricated with direct bonding. With the same technique, laser performance of a 100µm-thick 10at.% multimode Yb:YAG waveguide was reported by Griebner *et al.* [76]: a maximum CW output power of 1.2W was obtained and near-diffraction-limited output (M^2 values 1.5x4) was achieved by using an astigmatic resonator. Based on the technique of direct bonding, proximity coupling and double-clad structures were developed and reported by Bonner *et al.* [64]. It should be mentioned here that in this paper the authors described the technique of proximity coupling the diode-bar radiation to the planar waveguide without coupling optics, which probably led to the simplest pump scheme so far and provided efficient diode pumping, practically demonstrated in [89] by Beach *et al.* with >12W obtained from a side-pumped proximity-coupled double-clad Yb:YAG waveguide laser. In the same year, 15W output power [13] was achieved by side pumping again, from a double-clad Tm:YAG waveguide lasing at 2.02µm.

The main advantage of face pumping is that un-collimated or partially collimated laser light from a diode stack can be used to pump the thin slab [78], which simplifies the pumping design. The direct injection of “raw” light from a diode stack into the active waveguide can be achieved by pumping in a rectangular high reflecting chamber with narrow slots. With the face pumping scheme investigated in [78], the researchers at Heriot-Watt University presented a quasi-CW Nd:YAG PWL with a 9W average power in 1997 [90]. The waveguide consisted of a 200µm-thick Nd^{3+}-doped core and a 400µm-thick updoped cladding, fabricated by thermal bonding. The continuation of this work has kept on with the efforts to increase the average output power and to gain more compact system designs [12, 61]. The greatest output power reported for this arrangement so far is 150W in multi-mode operation and >100W in a high-brightness configuration using an external unstable resonator [91].

1.3 Structure of this thesis

Following this introduction the rest of this thesis is set out as follows. Chapter 2 details the theory used in describing the performance of the planar waveguide lasers and models the expected laser performance. Four parts are included: general laser performance theory, laser beam quality, thermal modelling, and waveguide theory. The main experimental results will be discussed in Chapters 3-6. Chapter 3 will compare the laser performance of parabolic tapered-waveguides with linear tapered-waveguides using Ti:sapphire pumping, to work out an optimum design for high-average-power diode-stripe-pumped tapered waveguide lasers towards 1-Watt level sources compatible with integrated circuits. Broad-stripe-diode end-pumping is also investigated and the laser performance is characterised, with linear tapered-waveguides. In Chapter 4, a diode-bar side-pumped waveguide laser will be demonstrated at high-brightness operation, utilising a double-clad structure and an extended stable cavity. Chapter 5 describes the experimental work done to develop a diode-stack side-pumped planar waveguide laser to achieve very high power laser output, associated with discussions on thermal managements and future directions. As this work is based on bonded waveguides which are not easy to mass produce, Nd:GGG PLD waveguides are assessed as a potential alternative in Chapter 6 using both Ti:sapphire and diode array pumps, along with the results obtained from self-imaging effects in a thin film. Conclusions and future work are presented in Chapter 7.

1.4 References

[1] T. Y. Fan and R. L. Byer, "Diode laser-pumped solid-state lasers," *IEEE Journal of Quantum Electronics,* vol. 24, pp. 895-912, Jun 1988.

[2] D. C. Brown, "Ultrahigh-average-power diode-pumped Nd:YAG and Yb:YAG lasers," *IEEE Journal of Quantum Electronics,* vol. 33, pp. 861-873, May 1997.

[3] N. V. Kravtsov, "Basic trends in the development of diode-pumped solid-state lasers," *Quantum Electronics,* vol. 31, pp. 661-677, Aug 2001.

[4] G. Cerullo, S. Desilvestri, and V. Magni, "High-efficiency, 40-W CW Nd:YLF laser with large TEM_{00} mode," *Optics Communications,* vol. 93, pp. 77-81, Sep 1992.

[5] S. C. Tidwell, J. F. Seamans, and M. S. Bowers, "Highly efficient 60-W TEM_{00} CW diode-end-pumped Nd:YAG laser," *Optics Letters,* vol. 18, pp. 116-118, Jan 15 1993.

[6] D. Golla, S. Knoke, W. Schone, G. Ernst, M. Rode, A. Tunnermann, and H. Welling, "300-W CW diode-laser side-pumped Nd:YAG rod laser," *Optics Letters,* vol. 20, pp. 1148-1150, May 15 1995.

[7] D. Golla, M. Rode, S. Knoke, W. Schone, and A. Tunnermann, "62-W CW TEM_{00} Nd:YAG laser side-pumped by fibre-coupled diode lasers," *Optics Letters,* vol. 21, pp. 210-212, Feb 1996.

[8] S. Konno, S. Fujikawa, and K. Yasui, "80 W CW TEM_{00} 1064 nm beam generation by use of a laser-diode-side-pumped Nd:YAG rod laser," *Applied Physics Letters,* vol. 70, pp. 2650-2651, May 1997.

[9] V. Dominic, S. MacCormack, R. Waarts, S. Sanders, S. Bicknese, R. Dohle, E. Wolak, P. S. Yeh, and E. Zucker, "110W fibre laser," *Electronics Letters,* vol. 35, pp. 1158-1160, Jul 1999.

[10] Y. Hirano, Y. Koyata, S. Yamamoto, K. Kasahara, and T. Tajime, "208-W TEM_{00} operation of a diode-pumped Nd : YAG rod laser," *Optics Letters,* vol. 24, pp. 679-681, May 15 1999.

[11] C. Stewen, K. Contag, M. Larionov, A. Giesen, and H. Hugel, "A 1-kW CW thin disc laser," *IEEE Journal of Selected Topics in Quantum Electronics,* vol. 6, pp. 650-657, Jul-Aug 2000.

[12] J. R. Lee, G. J. Friel, H. J. Baker, G. J. Hilton, and D. R. Hall, "A Nd:YAG planar waveguide laser operating at 121W output with face-pumping by diode bars, and its use as a power amplifier," in *Advanced Solid-State Lasers, Proceedings*. vol. 50, 2001, pp. 36-40.

[13] J. I. Mackenzie, S. C. Mitchell, R. J. Beach, H. E. Meissner, and D. P. Shepherd, "15W diode-side-pumped Tm:YAG waveguide laser at 2 µm," *Electronics Letters,* vol. 37, pp. 898-899, Jul 5 2001.

[14] Y. Jeong, J. K. Sahu, D. N. Payne, and J. Nilsson, "Ytterbium-doped large-core fiber laser with 1.36 kW continuous-wave output power," *Optics Express,* vol. 12, pp. 6088-6092, Dec 13 2004.

[15] D. Gapontsev, "Quasi-single-mode fiber laser nears 2-kW output with high-quality beam," *Laser Focus World,* vol. 41, p. 9, Jun 2005.

[16] D. Y. Shen, J. K. Sahu, and W. A. Clarkson, "Highly efficient in-band pumped Er : YAG laser with 60 W of output at 1645 nm," *Optics Letters,* vol. 31, pp. 754-756, Mar 15 2006.

[17] D. W. Hughes and J. R. M. Barr, "Laser diode pumped solid state lasers," *Journal Of Physics D-Applied Physics,* vol. 25, pp. 563-586, Apr 14 1992.

[18] A. Tunnermann, H. Zellmer, W. Schone, A. Giesen, and K. Contag, "New concepts for diode-pumped solid-state lasers," in *High-Power Diode Lasers: Fundamentals, Technology, Applications*. vol. 78, R. Diehl, Ed.: Springer-Verlag Berlin Heidelberg, 2000, pp. 369-408.

[19] L. Marshall, "Laser Diode-Pumped Solid-State Lasers," in *CLEO/QELS* Baltimore, USA, 2005, p. SC165.

[20] U. Brauch, P. Loosen, and H. Opower, "High-power diode lasers for direct applications," in *High-Power Diode Lasers: Fundamentals, Technology, Applications*. vol. 78, R. Diehl, Ed.: Springer-Verlag Berlin Heidelberg, 2000, pp. 303-368.

[21] W. Koechner, *Solid-state laser engineering - Chapter 6*, 5th ed. vol. 1: Springer-Verlag Berlin Heidelberg New York, 1999.

[22] W. F. Krupke, "Ytterbium solid-state lasers - The first decade," *IEEE Journal of Selected Topics in Quantum Electronics,* vol. 6, pp. 1287-1296, Nov-Dec 2000.

[23] N. P. Barnes, D. J. Gettemy, L. Esterowitz, and R. E. Allen, "Comparison of Nd 1.06 and 1.33 µm operation in various hosts," *IEEE Journal of Quantum Electronics,* vol. 23, pp. 1434-1451, Sep 1987.

[24] T. Y. Fan and R. L. Byer, "Continuous-wave operation of a room-temperature, diode-laser-pumped, 946-nm Nd:YAG laser," *Optics Letters,* vol. 12, pp. 809-811, Oct 1987.

[25] B. J. Dinerman, "3-µm CW laser operations in erbium-doped YSGG, GGG, and YAG," *Optics Letters,* vol. 19, pp. 1143-1145, Aug 1 1994.

[26] D. W. Chen, C. L. Fincher, T. S. Rose, F. L. Vernon, and R. A. Fields, "Diode-pumped 1-W continuous-wave Er:YAG 3 μm laser," *Optics Letters,* vol. 24, pp. 385-387, Mar 15 1999.

[27] L. Esterowitz, "Diode-pumped holmium, thulium, and erbium lasers between 2 and 3 μm operating CW at room temperature," *Optical Engineering,* vol. 29, pp. 676-680, Jun 1990.

[28] C. Li, J. Song, D. Y. Shen, N. S. Kim, K. Ueda, Y. J. Huo, S. F. He, and Y. H. Cao, "Diode-pumped high-efficiency Tm : YAG lasers," *Optics Express,* vol. 4, pp. 12-18, Jan 4 1999.

[29] P. M. W. French, R. Mellish, J. R. Taylor, P. J. Delfyett, and L. T. Florez, "All-solid-state diode-pumped modelocked Cr-LiSAF laser," *Electronics Letters,* vol. 29, pp. 1262-1263, Jul 8 1993.

[30] D. Kopf, K. J. Weingarten, G. Zhang, M. Moser, M. A. Emanuel, R. J. Beach, J. A. Skidmore, and U. Keller, "High-average-power diode-pumped femtosecond Cr:LiSAF lasers," *Applied Physics B-Lasers And Optics,* vol. 65, pp. 235-243, Aug 1997.

[31] H. W. Bruesselbach, D. S. Sumida, R. A. Reeder, and R. W. Byren, "Low-heat high-power scaling using InGaAs-diode-pumped Yb:YAG lasers," *IEEE Journal of Selected Topics in Quantum Electronics,* vol. 3, pp. 105-116, Feb 1997.

[32] T. Dascalu, N. Pavel, and T. Taira, "90 W continuous-wave diode edge-pumped microchip composite Yb : $Y_3Al_5O_{12}$ laser," *Applied Physics Letters,* vol. 83, pp. 4086-4088, Nov 17 2003.

[33] E. C. Honea, R. J. Beach, S. C. Mitchell, and P. V. Avizonis, "183-W, M^2 = 2.4 Yb : YAG Q-switched laser," *Optics Letters,* vol. 24, pp. 154-156, Feb 1 1999.

[34] W. Koechner, *Solid-state laser engineering - Chapter 2*, 5th ed. vol. 1: Springer-Verlag Berlin Heidelberg New York, 1999.

[35] P. Lacovara, H. K. Choi, C. A. Wang, R. L. Aggarwal, and T. Y. Fan, "Room temperature diode-pumped Yb:YAG laser," *Optics Letters,* vol. 16, pp. 1089-1091, Jul 15 1991.

[36] T. Y. Fan, "Optimizing the efficiency and stored energy in quasi-three-level lasers," *IEEE Journal of Quantum Electronics,* vol. 28, pp. 2692-2697, Dec 1992.

[37] H. W. Bruesselbach and D. S. Sumida, "69-W-average-power Yb:YAG laser," *Optics Letters,* vol. 21, pp. 480-482, 1994.

[38] L. D. Deloach, S. A. Payne, L. L. Chase, L. K. Smith, W. L. Kway, and W. F. Krupke, "Evaluation of absorption and emission properties of Yb^{3+} doped

crystals for laser applications," *IEEE Journal of Quantum Electronics,* vol. 29, pp. 1179-1191, Apr 1993.

[39] W. F. Krupke and L. L. Chase, "Ground-state depleted solid-state lasers - principles, characteristics and scaling," *Optical And Quantum Electronics,* vol. 22, Supplement 1, pp. S1-S22, Jul 1990.

[40] D. S. Sumida and T. Y. Fan, "Room-temperature 50-mJ/pulse side-diode-pumped Yb:YAG laser," *Optics Letters,* vol. 20, pp. 2384-2386, Dec 1 1995.

[41] W. Koechner, *Solid-state laser engineering - Chapter 7*, 5th ed. vol. 1: Springer-Verlag Berlin Heidelberg New York, 1999.

[42] U. Brauch and M. Schubert, "Comparison of lamp and diode pumped CW Nd:YAG slab lasers," *Optics Communications,* vol. 117, pp. 116-122, May 15 1995.

[43] T. Y. Fan, "Heat-generation in Nd-YAG and Yb-YAG," *IEEE Journal Of Quantum Electronics,* vol. 29, pp. 1457-1459, Jun 1993.

[44] B. Comaskey, B. D. Moran, G. F. Albrecht, and R. J. Beach, "Characterization of the heat loading of Nd-doped YAG, YOS, YLF, and GGG excited at diode pumping wavelengths," *IEEE Journal Of Quantum Electronics,* vol. 31, pp. 1261-1264, Jul 1995.

[45] W. A. Clarkson, "Thermal effects and their mitigation in end-pumped solid-state lasers," *Journal of Physics D-Applied Physics,* vol. 34, pp. 2381-2395, Aug 21 2001.

[46] S. Chenais, F. Balembois, F. Druon, G. Lucas-Leclin, and P. Georges, "Thermal lensing in diode-pumped ytterbium lasers - Part I: Theoretical analysis and wavefront measurements," *IEEE Journal Of Quantum Electronics,* vol. 40, pp. 1217-1234, Sep 2004.

[47] S. Chenais, F. Balembois, F. Druon, G. Lucas-Leclin, and P. Georges, "Thermal lensing in diode-pumped ytterbium lasers - Part II: Evaluation of quantum efficiencies and thermo-optic coefficients," *IEEE Journal Of Quantum Electronics,* vol. 40, pp. 1235-1243, Sep 2004.

[48] J. D. Foster and L. M. Osterink, "Thermal effects in a Nd:YAG Laser," *Journal Of Applied Physics,* vol. 41, pp. 3656-3663, 1970.

[49] J. M. Eggleston, T. J. Kane, K. Kuhn, J. Unternahrer, and R. L. Byer, "The slab geometry laser---part 1: Theory," *IEEE Journal of Quantum Electronics,* vol. 20, pp. 289-301, 1984.

[50] J. E. Marion, "Fracture of solid-state laser slabs," *Journal of Applied Physics,* vol. 60, pp. 69-77, Jul 1 1986.

[51] Y. F. Chen, C. F. Kao, T. M. Huang, C. L. Wang, and S. C. Wang, "Influence of thermal effect on output power optimization in fiber-coupled laser-diode end-pumped lasers," *IEEE Journal of Selected Topics in Quantum Electronics,* vol. 3, pp. 29-34, Feb 1997.

[52] R. Paschotta, J. Aus der Au, and U. Keller, "Thermal effects in high-power end-pumped lasers with elliptical-mode geometry," *IEEE Journal Of Selected Topics In Quantum Electronics,* vol. 6, pp. 636-642, Jul-Aug 2000.

[53] M. Tsunekane, N. Taguchi, T. Kasamatsu, and H. Inaba, "Analytical and experimental studies on the characteristics of composite solid-state laser rods in diode-end-pumped geometry," *IEEE Journal Of Selected Topics In Quantum Electronics,* vol. 3, pp. 9-18, Feb 1997.

[54] R. Weber, B. Neuenschwander, M. Mac Donald, M. B. Roos, and H. P. Weber, "Cooling schemes for longitudinally diode laser-pumped Nd : YAG rods," *IEEE Journal Of Quantum Electronics,* vol. 34, pp. 1046-1053, Jun 1998.

[55] W. C. Scott and M. D. Wit, "Birefringence compensation and TEM_{00} mode enhancement in a Nd:YAG Laser," *Applied Physics Letters,* vol. 18, pp. 3-4, Jan 1 1971.

[56] M. K. Davis, M. J. F. Digonnet, and R. H. Pantell, "Thermal effects in doped fibres," *Journal of Lightwave Technology,* vol. 16, pp. 1013-1023, Jun 1998.

[57] A. Giesen, H. Hugel, A. Voss, K. Wittig, U. Brauch, and H. Opower, "Scalable concept for diode-pumped high-power solid-state lasers," *Applied Physics B-Lasers And Optics,* vol. 58, pp. 365-372, May 1994.

[58] L. Zenteno, "High-power double-clad fiber lasers," *Journal Of Lightwave Technology,* vol. 11, pp. 1435-1446, Sep 1993.

[59] T. S. Rutherford, W. M. Tulloch, E. K. Gustafson, and R. L. Byer, "Edge-pumped quasi-three-level slab lasers: Design and power scaling," *IEEE Journal of Quantum Electronics,* vol. 36, pp. 205-219, Feb 2000.

[60] H. J. Baker, A. A. Chesworth, D. P. Millas, and D. R. Hall, "A planar waveguide Nd:YAG laser with a hybrid waveguide - unstable resonator," *Optics Communications,* vol. 191, pp. 125-131, May 1 2001.

[61] J. R. Lee, H. J. Baker, G. J. Friel, G. J. Hilton, and D. R. Hall, "High-average-power Nd:YAG planar waveguide laser that is face pumped by 10 laser diode bars," *Optics Letters,* vol. 27, pp. 524-526, Apr 1 2002.

[62] P. Madasamy, S. Honkanen, D. F. Geraghty, and N. Peyghambarian, "Single-mode tapered waveguide laser in Er-doped glass with multimode-diode pumping," *Applied Physics Letters,* vol. 82, pp. 1332-1334, Mar 3 2003.

[63] J. Q. Xu, "Quasi-self-imaging planar waveguide lasers with high-power single-mode output," *Optics Communications,* vol. 259, pp. 251-255, Mar 1 2006.

[64] C. L. Bonner, T. Bhutta, D. P. Shepherd, and A. C. Tropper, "Double-clad structures and proximity coupling for diode-bar-pumped planar waveguide lasers," *IEEE Journal of Quantum Electronics,* vol. 36, pp. 236-242, Feb 2000.

[65] D. P. Shepherd, S. J. Hettrick, C. Li, J. I. Mackenzie, R. J. Beach, S. C. Mitchell, and H. E. Meissner, "High-power planar dielectric waveguide lasers," *Journal of Physics D-Applied Physics,* vol. 34, pp. 2420-2432, Aug 21 2001.

[66] T. Findakly, "Glass waveguides by ion-exchange: A review," *Optical Engineering,* vol. 24, pp. 244-250, 1985.

[67] R. V. Schmidt and I. P. Kaminow, "Metal-diffused optical waveguides in $LiNbO_3$," *Applied Physics Letters,* vol. 25, pp. 458-460, 1974.

[68] P. J. Chandler, L. Zhang, and P. D. Townsend, "Ion-implanted wave-guides in laser host materials," *Nuclear Instruments & Methods - Physics Research Section B - Beam Interactions with Materials and Atoms,* vol. 59, pp. 1223-1227, Jul 1991.

[69] M. Svalgaard, C. V. Poulsen, A. Bjarklev, and O. Poulsen, "Direct UV writing of buried singlemode channel waveguides in Ge-doped silica films," *Electronics Letters,* vol. 30, pp. 1401-1403, 1994.

[70] M. Kawachi, "Silica waveguides on silicon and their application to integrated-optic components," *Optical and Quantum Electronics,* vol. 22, pp. 391-416, 1990.

[71] I. Chartier, B. Ferrand, D. Pelenc, S. J. Field, D. C. Hanna, A. C. Large, D. P. Shepherd, and A. C. Tropper, "Growth and low-threshold laser oscillation of an epitaxially grown Nd:YAG waveguide," *Optics Letters,* vol. 17, pp. 810-812, Jun 1 1992.

[72] C. T. A. Brown, C. L. Bonner, T. J. Warburton, D. P. Shepherd, A. C. Tropper, D. C. Hanna, and H. E. Meissner, "Thermally bonded planar waveguide lasers," *Applied Physics Letters,* vol. 71, pp. 1139-1141, Sep 1 1997.

[73] D. P. Shepherd, C. L. Bonner, C. T. A. Brown, W. A. Clarkson, A. C. Tropper, D. C. Hanna, and H. E. Meissner, "High-numerical-aperture, contact-bonded, planar waveguides for diode-bar-pumped lasers," *Optics Communications,* vol. 160, pp. 47-50, Feb 1 1999.

[74] R. V. Ramaswamy and R. Srivastava, "Ion-exchanged glass waveguides: a review," *Journal of Lightwave Technology,* vol. 6, pp. 984-1002, Jun 1988.

[75] J. Haisma, B. Spierings, U. K. P. Biermann, and A. A. Vangorkum, "Diversity and feasibility of direct bonding - a survey of a dedicated optical-technology," *Applied Optics,* vol. 33, pp. 1154-1169, March 1 1994.

[76] U. Griebner, R. Grunwald, and H. Schonnagel, "Thermally bonded Yb : YAG planar waveguide laser," *Optics Communications,* vol. 164, pp. 185-190, Jun 15 1999.

[77] C. Grivas, T. C. May-Smith, D. P. Shepherd, and R. W. Eason, "Laser operation of a low loss (0.1 dB/cm) Nd : $Gd_3Ga_5O_{12}$ thick (40 μm) planar waveguide grown by pulsed laser deposition," *Optics Communications,* vol. 229, pp. 355-361, Jan 2 2004.

[78] A. Faulstich, H. J. Baker, and D. R. Hall, "Face pumping of thin, solid-state slab lasers with laser diodes," *Optics Letters,* vol. 21, pp. 594-596, Apr 15 1996.

[79] L. R. Marshall, A. Kaz, and R. L. Burnham, "Highly efficient TEM_{00} operation of transversely diode-pumped Nd-YAG lasers," *Optics Letters,* vol. 17, pp. 186-188, Feb 1 1992.

[80] L. Cabaret and G. Girard, "Study of some pumping schemes for laser diode pumped solid-state lasers," *Journal De Physique Iii,* vol. 2, pp. 1703-1712, Sep 1992.

[81] N. S. Kapany, *Fiber optics: Principles and applications*. New York: Academic Press, 1967.

[82] G. Zeidler, "Optical waveguide technique with organic dye lasers," *Journal of Applied Physics,* vol. 42, pp. 884-885, 1971.

[83] A. A. Anderson, R. W. Eason, L. M. B. Hickey, M. Jelinek, C. Grivas, D. S. Gill, and N. A. Vainos, "Ti:sapphire planar waveguide laser grown by pulsed laser deposition," *Optics Letters,* vol. 22, pp. 1556-1558, Oct 15 1997.

[84] C. Becker, T. Oesselke, J. Pandavenes, R. Ricken, K. Rochhausen, G. Schreiber, W. Sohler, H. Suche, R. Wessel, S. Balsamo, I. Montrosset, and D. Sciancalepore, "Advanced Ti:Er:$LiNbO_3$ Waveguide Lasers," *IEEE Journal of Quantum Electronics,* vol. 36, pp. 101-113, 2000.

[85] T. Bhutta, A. M. Chardon, D. P. Shepherd, E. Daran, C. Serrano, and A. Munoz-Yague, "Low phonon energy Nd:LaF_3 channel waveguide lasers fabricated by molecular beam epitaxy," *IEEE Journal Of Quantum Electronics,* vol. 37, pp. 1469-1477, Nov 2001.

[86] D. C. Hanna, A. C. Large, D. P. Shepherd, A. C. Tropper, I. Chartier, B. Ferrand, and D. Pelenc, "A side-pumped Nd:YAG epitaxial waveguide laser," *Optics Communications,* vol. 91, pp. 229-235, July 15 1992.

[87] D. Pelenc, B. Chambaz, I. Chartier, B. Ferrand, C. Wyon, D. P. Shepherd, D. C. Hanna, A. C. Large, and A. C. Tropper, "High slope efficiency and low-threshold in a diode-pumped epitaxially grown Yb:YAG waveguide laser," *Optics Communications,* vol. 115, pp. 491-497, Apr 1 1995.

[88] C. L. Bonner, C. T. A. Brown, D. P. Shepherd, W. A. Clarkson, A. C. Tropper, D. C. Hanna, and B. Ferrand, "Diode-bar end-pumped high-power Nd:$Y_3Al_5O_{12}$ planar waveguide laser," *Optics Letters,* vol. 23, pp. 942-944, Jun 15 1998.

[89] R. J. Beach, S. C. Mitchell, H. E. Meissner, O. R. Meissner, W. F. Krupke, J. M. McMahan, W. J. Bennett, and D. P. Shepherd, "Continuous-wave and passively Q-switched cladding-pumped planar waveguide lasers," *Optics Letters,* vol. 26, pp. 881-883, Jun 15 2001.

[90] D. P. Millas, A. Faulstich, H. J. Baker, and D. R. Hall, "A planar waveguide Nd:YAG laser, face pumped by laser diode bars," in *Proceedings of the XI International Symposium on Gas Flow and Chemical Lasers and High Power Lasers*. vol. 3092, 1997, pp. 25-28.

[91] H. J. Baker, J. R. Lee, and D. R. Hall, "Planar waveguide solid-state lasers," in *CLEO/QELS* Long Beach, USA, 2002, p. CTuP1.

Chapter 2

Theory

2.1 Introduction

This chapter discusses the theoretical aspects that are essential to the experimental work and future directions detailed in this thesis. The laser performance theory presented here, along with the equations needed for the analysis of results, can be applied to the diode-pumped waveguide lasers studied in this work. A basic discussion on the laser beam quality is given in order to introduce the important concepts concerning the propagation of multimode laser beams. A model developed to predict the effects of heat flow in a side-pumped planar waveguide laser is also investigated and this is of particular importance for high-power operation. Finally, an introductory overview of waveguide theory will be presented followed by more detailed discussions on the waveguide structures that are relevant to the experimental chapters.

2.2 Laser performance

Here two modelling approaches will be introduced to characterise the performance of a solid-state laser. The first, based on the analysis of Risk [1], starts with the rate equations, describing the population-inversion density and the cavity photon number, which are modified to account for reabsorption losses, spatial distribution of the laser and pump fields and gain saturation. This model provides a comprehensive understanding as to how various factors (especially spatial overlaps) affect the performance characteristics of longitudinally pumped lasers such as laser threshold and slope efficiency. The other approach is based on a simplified plane-wave analysis developed by Beach in 1995 [2], for a quasi-three level, end-pumped laser oscillator, which can be easily applied to our side-pumping configurations. This model also allows the simple tracking of all the output channels for the input pump power, which is useful for determining the full thermal loading in high-power waveguide lasers.

2.2.1 Spatial rate equation analysis

In the past [1, 3-7], many authors have modelled the behaviour of laser systems, including the effects of the overlap of the pump and laser fields. Here we follow Risk's model [1], which gives a general understanding of the effects of mode overlap with arbitrary sizes of the pump and laser modes, to predict laser performance, and can be applied to both four and quasi-three level lasers.

A steady-state spatial rate equation analysis is applied to a non-uniformly doped active material, of which the planar waveguide is one example, to determine the effect of the relative sizes of the pump beam and the laser beam on the threshold and the slope efficiency. With careful design of the doping profile, it is shown that the fundamental-mode operation can be robustly maintained even under highly saturated, high-power conditions [8].

The modelling described here adopts a quasi-three-level laser energy-level scheme shown in Fig. 2.1, in which the population density of the lower laser level N_1 is not presumed to be zero, as in the case of a four-level laser, but is assumed to have a small thermal population. It should be noted, however, that the approach is also easily applicable to four-level lasers. As shown in figure 2.1, the lower laser level "*1*" and the upper laser level "*2*" are two particular crystal-field components lying in the lower and upper manifold respectively, denoted as *L* and *U*. The relative populations of all levels of *L* and *U* can be assumed to obey a Boltzmann distribution under steady-state pumping [1].

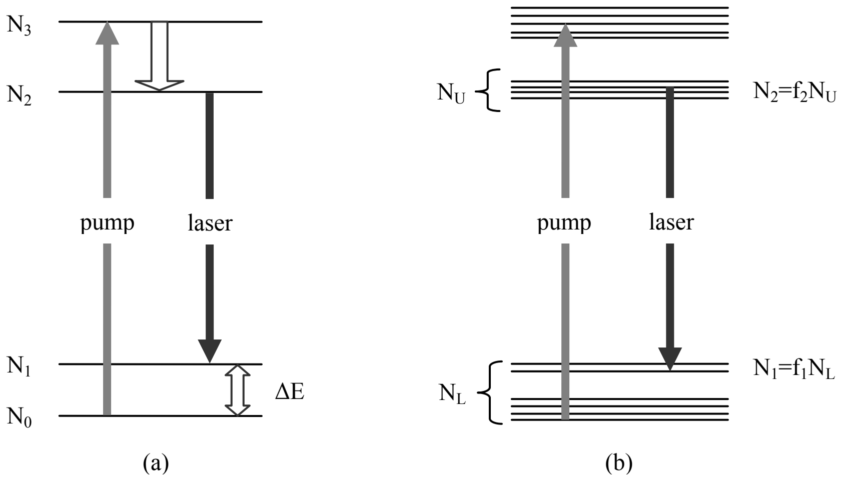

Figure 2.1 (a) Idealized energy-level scheme and (b) a practical quasi-three-level energy diagram.

Therefore, in contrast with the case of four-level lasers, the population density of the lower laser level N_1 is assumed to have a small thermal population, regarded as a fraction of the total population density of the lower manifold N_L: $N_1 = f_1 N_L$. In the same way, the actual population density of the upper laser level can be expressed as $N_2 = f_2 N_U$. The laser performance is modelled starting from the rate equations describing the population inversion and the photon density in the laser cavity in the steady-state case. Following the assumptions given by Risk [1], the laser rate equation for the population-inversion density, $\Delta N(x,y,z) = N_2(x,y,z) - N_1(x,y,z)$, at steady state is written as,

$$\frac{d\Delta N(x,y,z)}{dt} = fRr_p(x,y,z) - \frac{\Delta N(x,y,z) - \Delta N^0}{\tau} - \frac{fc\sigma\Delta N(x,y,z)}{n}\Phi\phi_0(x,y,z) = 0 \quad (2.1),$$

where

f = sum of the occupation factors for the lower (f_1) and upper (f_2) laser Stark levels as stated above;

ΔN^0 = population-inversion density at thermal equilibrium (un-pumped situation);

τ = lifetime of the upper laser-level manifold;

c = speed of light in vacuum;

σ = gain cross section;

n = refractive index of the laser medium at the laser wavelength.

$Rr_p(x,y,z)$ and $\Phi\phi_0(x,y,z)$ describe the pump and laser modes, respectively. The total pump rate is given by $R = P_p\eta_a / h\nu_p$, determined by the incident pump power P_p, the absorption efficiency $\eta_a = 1-\exp(-\alpha_p l)$ in the active material of length l with absorption coefficient α_p at the pump wavelength, and the pump photon energy $h\nu_p$; while Φ is the total cavity photon number given by $\Phi = 2nlP_l / ch\nu_l$, with P_l the laser power travelling inside the laser cavity and $h\nu_l$ the laser photon energy. Finally, $r_p(x,y,z)$ and $\phi_0(x,y,z)$ are the normalised spatial pump energy and laser photon distribution, respectively.

It should be noted that, in the condition of thermal equilibrium, $N_1^0 >> N_2^0$ so that the equilibrium population inversion density ΔN^0 can be written as $\Delta N^0 \approx -N_1^0$. Therefore, below threshold, by substituting $\Phi = 0$ into equation (2.1) it is found that the population-inversion density is given by,

$$\Delta N(x,y,z) = \tau f R r_p(x,y,z) - N_1^0 \qquad (2.2).$$

Above threshold, also from equation (2.1), the spatial distribution of the inversion density is written as

$$\Delta N(x,y,z) = \frac{\tau f R r_p(x,y,z) - N_1^0}{1 + \frac{c\sigma\tau f}{n}\Phi\phi_0(x,y,z)} \qquad (2.3).$$

Hence it follows that although the total inversion above threshold is clamped such that gain equals loss, the spatial distribution of the inversion is not necessarily constant above threshold but changes as a function of the pump and laser intensity, as described by equation (2.3).

In the condition of the normal steady-state laser, equating the total round-trip cavity losses to the gain, then

$$L+T_{oc}=2\sigma l\iiint \Delta N(x,y,z)\phi_0(x,y,z)dV \qquad (2.4),$$

where

L = the round-trip loss exponent $=2\alpha_L l$ (α_L is the propagation loss coefficient);

T_{oc} = the transmission of the output coupler $\approx -\ln R_{oc}$ (R_{oc} is the output coupler reflectivity at the laser wavelength).

Based on (2.4), the gain for each waveguide mode for a given doping distribution in a certain laser cavity is found, in the next section.

2.2.1.1 Mode dependent gain

For an approximately uniformly pumped laser, such as a diode side-pumped waveguide laser, which is discussed in later chapters, the first term of equation (2.1) $fRr_p(x,y,z)$ can then be replaced by $fRd(x,y,z)$ [8], where $d(x,y,z)$ is the normalized doping profile in the active medium,

$$\iiint d(x,y,z)\,dV=1 \qquad (2.5).$$

The un-pumped population density profile in the lower laser Stark level can be written as $n_1^0 d(x,y,z)$, where n_1^0 is the total population in the terminal laser level. Thus equation (2.3) will be rewritten as follows,

$$\Delta N(x,y,z)=\frac{\tau fRd(x,y,z)-n_1^0 d(x,y,z)}{1+\dfrac{c\sigma\tau f}{n}\Phi\phi_0(x,y,z)} \qquad (2.6).$$

Equations (2.4) and (2.6) can be evaluated numerically in order to find the output laser power versus the input pump power for a given laser system. Combining equations (2.4) and (2.6) can give:

$$\iiint\frac{(\tau fR-n_1^0)d(x,y,z)}{1+S\phi_0(x,y,z)}\phi_0(x,y,z)dV=\frac{L+T_{oc}}{2\sigma l} \qquad (2.7),$$

where

$S = \frac{c\sigma\tau f}{n}\Phi$, which gives a measure of the degree of saturation caused by the intra-cavity laser power.

After substituting equation (2.7) back into (2.6), the population inversion density distribution can be expressed only in terms of the losses and the laser power:

$$\Delta N(x,y,z) = \frac{d(x,y,z)(L+T_{oc})}{2\sigma l\left[1+S\phi_0(x,y,z)\right]\iiint \frac{d(x,y,z)\phi_0(x,y,z)}{1+S\phi_0(x,y,z)}dV} \qquad (2.8).$$

Now the gain G_p for a particular p^{th} mode with spatial distribution ϕ_p, with a population inversion saturated by a lasing mode with spatial distribution ϕ_0, is then given by [8]

$$\begin{aligned} G_p &= 2\sigma l\iiint \Delta N(x,y,z)\phi_p(x,y,z)dV \\ &= (L+T_{oc})\iiint \frac{d(x,y,z)\phi_p(x,y,z)}{\left[1+S\phi_0(x,y,z)\right]\left[\iiint \frac{d(x,y,z)\phi_0(x,y,z)}{1+S\phi_0(x,y,z)}dV\right]}dV \end{aligned} \qquad (2.9).$$

Therefore, for a multimode waveguide, including fibre and planar formats, the gain for each guided mode is a function of the crystal doping profile, the mode spatial profile, the saturating spatial distribution and the laser power. This can be used to theoretically explain the selectivity of fundamental-mode operation from multimode waveguides with doping profiles that vary in one direction [8, 9]. We will further discuss a planar geometry with a doped central portion to give a selective overlap with the fundamental mode in Chapter 4.

2.2.1.2 Threshold and slope efficiency

Here we only consider a (possibly asymmetric) Gaussian intensity distribution for both the pump beam and the laser beam with no diffraction, and assume that the pump beam only passes once through the gain medium, i.e., unabsorbed pump light is assumed not to be reflected back into the laser medium. Hence, in the laser medium the normalized spatial distribution of pump and cavity modes, $r_P(x,y,z)$ and $\phi_0(x,y,z)$ respectively, are written as

$$r_p(x,y,z) = \frac{2\alpha_p}{\eta_a \pi \omega_{px}\omega_{py}} \exp\left[-2\left(\frac{x^2}{\omega_{px}^2} + \frac{y^2}{\omega_{py}^2}\right)\right]\exp(-\alpha_p z) \tag{2.10}$$

$$\phi_0(x,y,z) = \frac{2}{\pi \omega_{lx}\omega_{ly} l} \exp\left[-2\left(\frac{x^2}{\omega_{lx}^2} + \frac{y^2}{\omega_{ly}^2}\right)\right] \tag{2.11}$$

where

$$\iiint r_p(x,y,z)dV = \iiint \phi_0(x,y,z)dV = 1 \qquad (2.12).$$

ω_p and ω_l are the Gaussian beam radii for the pump and laser cavity modes on both axes of the transverse plane.

Although, as already stated, the expected laser performance is normally calculated numerically, an analytical expression for the laser threshold can be calculated by setting $\Phi = 0$ in equation (2.6) and substituting (2.6), (2.10) and (2.11) into equation (2.4) to give

$$P_{th} = \frac{\pi h \nu_p \left[(\omega_{px}^2 + \omega_{lx}^2)(\omega_{py}^2 + \omega_{ly}^2)\right]^{\frac{1}{2}} (L + T_{oc} + 2N_1^0 \sigma l)}{4\sigma\tau\eta_a f} \qquad (2.13).$$

Here it is observed that as far as the laser threshold is concerned the reabsorption loss term $N_1^0\sigma l$, which is zero in four-level lasers, appears as a loss no different from the usual cavity loss. It is clear from equation (2.13) that small pump-beam size, small laser-beam size, low loss, and low transmission of the output coupler will produce a low laser threshold. Hence, for waveguide lasers, the sum of the beam radii for the pump and laser modes $(\omega_p^2 + \omega_l^2)$ is generally smaller compared with equivalent bulk lasers, which leads to the relatively low laser threshold of waveguide lasers.

The slope efficiency is given by [1],

$$\eta_{slope} = \eta_a \frac{v_l}{v_p} \frac{T_{oc}}{L + T_{oc}} \eta_{pl} \tag{2.14}$$,

where η_{pl} is a term that accounts for spatial overlap of the output and pump lasers inside the laser medium. It is clear that to increase the slope efficiency for a given laser system, the propagation loss L must be as small as possible, and that optimising the efficiency η_{pl} is desirable. Increasing the output coupler transmission T_{oc} can improve the slope efficiency, but it will also increase the laser threshold. Therefore, the transmission of the cavity output coupler needs to be carefully optimised to achieve both high slope efficiency and reasonable laser threshold.

For a longitudinally-pumped four-level laser, η_{pl} can be written as [10],

$$\eta_{pl} = \frac{\omega_{lx}\omega_{ly}(2\omega_{px}^2 + \omega_{lx}^2)^{1/2}(2\omega_{py}^2 + \omega_{ly}^2)^{1/2}}{(\omega_{px}^2 + \omega_{lx}^2)(\omega_{py}^2 + \omega_{ly}^2)} \tag{2.15}$$.

It can be seen from equation (2.15) that, to gain high η_{pl}, the pump beam size needs to be reduced below the laser beam size. For a waveguide laser, since the pump has a shorter wavelength than the laser, the pump mode is usually smaller or nearly equivalent in size to the laser mode, which results in a good spatial overlap (η_{pl}=0.75 for $\omega_p = \omega_l$).

2.2.2 Plane-wave analysis

In section 2.2.1 the approach using rate equations to model the behaviour of solid-state lasers was described, in which case it is necessary to have knowledge of the spatial details of the laser and pump schemes. Here another way to characterize the laser system is presented, based on the work of Beach [2], starting with a straightforward plane wave analysis accounting for the pump and laser power. This approach is applicable to the high-power uniformly side-pumped waveguide lasers, discussed later in Chapter 4 and 5, and allows the simple tracking of the various output channels for the input pump power.

As an example, a side-pumped quasi-three level continuous-wave laser will be modelled, along with a set of derived equations which are useful for the optimization of the laser performance. The derived equations correctly account for ground state depletion due to intense pumping as well as gain saturation due to the extracting laser beam. It should be noted that this method is also suitable for the end-pumping configuration, which is in fact modelled in [2], and the theory covers the cases of both single and double passes through the laser medium for the pump beam, depending on the value of the pump reflectivity at the laser output end.

Fig. 2.2 (a) shows a quasi-three-level energy scheme, from which we can tell clearly that the terminal laser Stark level lies in the ground state manifold; Fig. 2.2 (b) gives the Stark level spectroscopy of an Yb:YAG laser, as an example for the following modelling in a side-pumped configuration with a slab geometry. Some relevant parameters are explained here: f_L^p is the initial pump Stark level Boltzmann occupation factor, f_U^p is the terminal pump Stark level Boltzmann occupation factor, f_U^l is the initial laser Stark level Boltzmann occupation factor, and f_L^l is the final laser Stark level Boltzmann occupation factor. σ_p is the spectroscopic pump absorption cross section, while σ_l is the spectroscopic laser emission cross section.

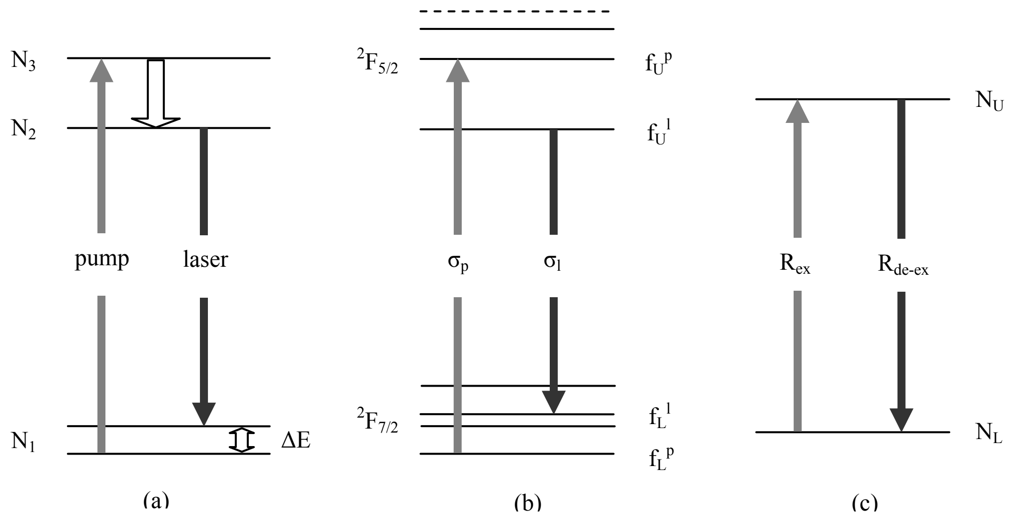

Figure 2.2 (a) A quasi-three-level energy scheme for a laser system , (b) Stark level spectroscopy of Yb^{3+} : YAG, and (c) a sketch for the processes of excitation and de-excitation of the lasing ions in the laser medium for an Yb^{3+} : YAG laser.

It is assumed that all of the active ions (n_A) are contained either in the lower (n_L) or upper (n_U) manifold, which is expressed by

$$n_A = n_L + n_U \tag{2.16}$$

in terms of population density. Changes in the population levels are defined by "excitation" and "de-excitation" [2] from the lower and upper levels respectively, as shown in Fig. 2.2 (c).

Another characteristic feature of this plane wave model is the linear relationship assumed between the input power and the output power, as shown in Fig. 2.3, when the pump excitation and laser extraction beams are both plane waves. That is, this model does not predict a reduced slope efficiency near the laser threshold as often seen in the analysis of Risk [1]. The output power P_{out} is expressed by,

$$P_{out} = \eta_{slope}(P_p - P_{th}) \qquad (2.17).$$

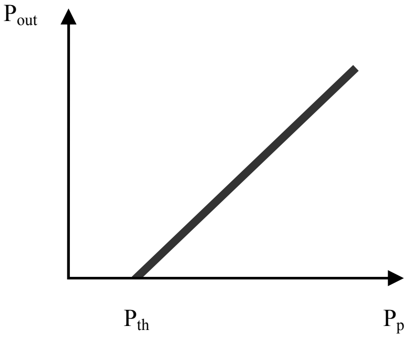

Figure 2.3 A linear slope efficiency diagram, where the slope efficiency is the gradient with P_{out} plotted against P_p.

Next, we need to derive the expressions for the rate of excitation of the lasing ions in the active crystal and their de-excitation. These must be equal in a steady state, and hence will immediately lead to the expressions of the laser threshold and slope efficiency.

2.2.2.1 Rate of excitation

When the laser is operating in the steady state, the fraction of incident pump power delivered to the laser medium, that is absorbed in a single pass through the width of the crystal w_c, is

$$F_A = 1 - \exp\left[-\sigma_p \eta_{po} \int_0^{w_c} (f_L^p n_L - f_U^p n_U) dx \right] \tag{2.18}$$

where η_{po} is the pump overlap with the doped region [11]. With the assumption stated in equation (2.16), the integrating factor in (2.18) can be rewritten as,

$$f_U^p n_U - f_L^p n_L = (f_L^p + f_U^p) n_U - f_L^p n_A \quad (2.19).$$

Here we define an integrated inversion density with respect to the crystal width w_c and referenced to the Stark levels coupled by the pump radiation,

$$N_U^p = (f_L^p + f_U^p) n_U w_c - f_L^p n_A w_c \quad (2.20),$$

so that we obtain

$$F_A = 1 - e^{\sigma_p \eta_{po} N_U^p} \quad (2.21).$$

The rate at which ions are excited into the upper laser manifold by the pumping process is therefore given by,

$$R_{ex} = \eta_{del} \frac{P_p}{h\nu_p} (1 - e^{\sigma_p \eta_{po} N_U^p}) \tag{2.22}$$

where the pump delivery efficiency, η_{del}, is included to account for the coupling factor of the pump radiation into the waveguide.

2.2.2.2 Rate of de-excitation

The same type of argument can be made for the de-excitation rate of the lasing ions in the gain medium. Correspondingly, the fraction of laser power “absorbed” in a single pass along the length of the crystal l is

$$F_B = e^{\sigma_l \eta_{lo} N_U^l} - 1 \qquad (2.23)$$

where η_{lo} is the laser overlap with the doped region, and we define an integrated inversion density with respect to the crystal length l,

$$N_U^l = (f_L^l + f_U^l) n_U l - f_L^l n_A l \qquad (2.24).$$

The laser power in the cavity, P_{cav}, can be related to the laser output power, P_{out}, by

$$P_{cav} = \frac{R_{oc}}{1 - R_{oc}} P_{out} \qquad (2.25),$$

where R_{oc} is the reflectivity of the laser output coupler, as defined in section 2.2.1. To trace this power through the cavity, the assumption is made that all the passive cavity losses (excluding the output coupler and ground state absorption) which contribute to the one-way cavity transmission, T_{ow}, are located at the high reflector end of the laser cavity. Consequently, the de-excitation rate of the lasing ions for a double pass in the gain medium is

$$R_{de-ex} = \frac{P_{out}}{\eta_{mode} h \nu_l} \left(\frac{R_{oc}}{1 - R_{oc}}\right)\left(e^{\sigma_l \eta_{lo} N_U^l} - 1\right)\left(1 + T_{ow}^2 e^{\sigma_l \eta_{lo} N_U^l}\right) + \frac{n_U w_c l d_{core}}{\tau_{eff}} \qquad (2.26),$$

where η_{mode} stands for the fill factor of the laser beam with respect to the laser gain cross-sectional area [2], d_{core} is the depth of the doped region, and τ_{eff} is the effective emission lifetime of the upper laser level dependent upon radiative and non-radiative decay in addition to other excited state energy transfer mechanisms, such as upconversion and cross relaxation.

2.2.2.3 Slope efficiency and laser threshold

The slope efficiency η_{slope} and laser threshold P_{th} are derived when (2.22) is equated with (2.26), as follows,

$$\eta_{slope} = \eta_{mode} \eta_{del} \frac{\nu_l}{\nu_p} \left(\frac{1 - R_{oc}}{R_{oc}}\right) \left[\frac{1 - e^{\sigma_p \eta_{po} N_U^p}}{\left(e^{\sigma_l \eta_{lo} N_U^l} - 1\right)\left(1 + T_{ow}^2 e^{\sigma_l \eta_{lo} N_U^l}\right)}\right] \qquad (2.27)$$

$$P_{th} = \frac{h\nu_p}{\eta_{del}\tau_{eff}}\left(\frac{n_U w_c l d_{core}}{1-e^{\sigma_p \eta_{po} N_U^p}}\right) \qquad (2.28).$$

2.3 Laser beam quality

Characterising beam quality is very important in this work, for both pump and laser beams, since beam quality of the pump source significantly affects the efficiency with which its radiation may be coupled into the laser medium, and high quality is also essential for the laser beam which, in many applications, must have a high intensity output beam that can be easily focussed. It is well known that the "highest beam quality" is given by the fundamental, Gaussian, or "TEM_{00}" mode, which has the lowest possible divergence and delivers the highest concentration of power over the longest propagation distance. However, many lasers do not produce this ideal output and so the beam quality needs to be characterised, in order to trace the optical propagation properly. One measure of beam quality is given by the M^2 factor, equivalent to the degree to which the divergence exceeds natural diffraction. In this section, the definition of the M^2 factor is discussed, with related issues.

2.3.1 Gaussian beam propagation

For a propagating Gaussian beam, although the intensity distribution is Gaussian in every beam cross section, the width of the intensity profile changes along the propagation axis, as shown in Fig. 2.4. The spot size of the fundamental mode beam is then defined in terms of a beam waist w_0, which is the minimum beam radius along the propagation axis, and the beam divergence angle related to the beam waist is given by $\theta = \lambda / \pi w_0$ [12].

Two important parameters of a Gaussian fundamental mode beam will change as the beam at the wavelength λ propagates along the *z*-axis: they are the spot radius (w) and the wavefront curvature (R),

$$w(z)=w_0\left[1+\left(\frac{\lambda z}{\pi w_0^2}\right)^2\right]^{\frac{1}{2}} \qquad R(z)=z\left[1+\left(\frac{\pi w_0^2}{\lambda z}\right)^2\right] \qquad (2.29,\ 30).$$

Here w_0 is the spot radius at the waist ($z=0$).

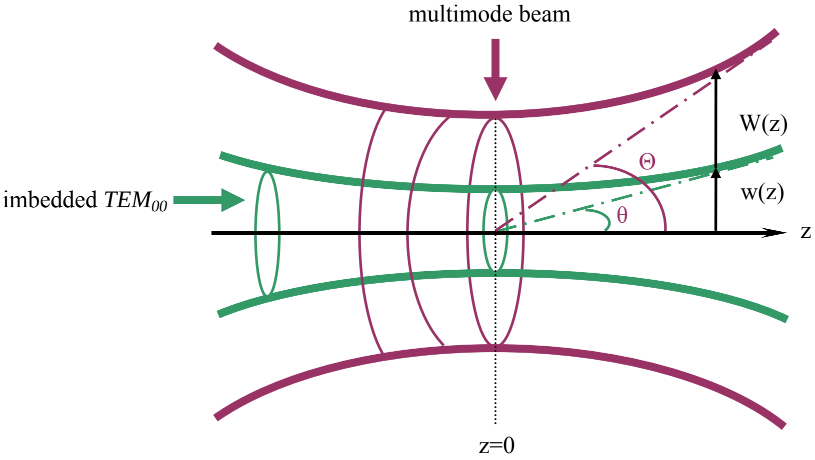

Figure 2.4 The geometries of imbedded Gaussian beam and multimode beam.

2.3.2 Definition of the M^2 factor

As shown in figure 2.4, beams are often not pure modes but mixtures of transverse modes, with higher-order mode components producing larger beam radii and divergence angles. It has been pointed out, in [13], that a constant M can act as a factor to characterize real mixed-mode beams by

$$W(z)=M\cdot w(z) \qquad (2.31),$$

where $W(z)$ is the transverse extent of any high-order mode, which is everywhere larger than the underlying Gaussian beam by the same factor. As stated above, in the paraxial approximation the half-divergence-angle of the Gaussian beam is given by $\theta=\lambda/\pi w_0$, while it is easy to find that this value of the higher-order mode with the spot size $W_0=Mw_0$ is given by,

$$\Theta = M \cdot \frac{\lambda}{\pi w_0} = M \cdot \frac{\lambda}{\pi \frac{W_0}{M}} = M^2 \cdot \frac{\lambda}{\pi W_0} \qquad (2.32).$$

Therefore, this divergence-half-angle of the relative high-order mode, Θ, is M^2 times that of a Gaussian beam with spot size W_0.

Equation (2.32) has the same form as its fundamental Gaussian beam counterpart except for the factor M^2. When $M^2 = 1$, it changes back to the fundamental Gaussian beam equation and the M^2 factor increases for modes of greater divergence, indicating "poorer" beam quality. Therefore, the beam propagation factor M^2 serves as a measure of beam quality and limits the ability to focus a beam, which is very important in many applications. In later chapters, high M^2 diode pump beams are converted to low M^2 laser outputs, so relevant calculations and analyses based on the M^2 concept are required in the experimental work discussed in this thesis.

2.3.3 Defining beam width

One of the core questions in developing a meaningful measure of "beam quality" for laser beams is simply: what is a practical and readily measurable definition for the "width" of a beam (or beam size)? Possible definitions of beam width that have been suggested or used for optical beams in the past include [14]: (1) width (or half-width) at first nulls; (2) variance of the intensity profile in one or the other transverse direction; (3) width at $1/e$ or $1/e^2$ intensity points; (4) the "D86" diameter, containing 86% of the total beam energy; (5) transverse knife edge widths between 10%-90% or 5%-95% integrated intensities; (6) width of a rectangular profile having the same peak intensity and same total power; (7) width of some kind of best fit Gaussian fitted to the measured profile; etc.

Among the various beam width definitions mentioned above the variance definition perhaps comes the closest to a mathematically useful formulation [14]. The beam radius, W, is defined as follows based on the second moment [13] of the intensity distribution $I(x)$ and $I(y)$ across the transverse co-ordinates x and y, respectively:

$$W_x = \sqrt{2\overline{x^2}} = \sqrt{2\frac{\int_{-\infty}^{\infty} x^2 I(x)dx}{\int_{-\infty}^{\infty} I(x)dx}} \tag{2.33}$$

$$W_y = \sqrt{2\overline{y^2}} = \sqrt{2\frac{\int_{-\infty}^{\infty} y^2 I(y)dy}{\int_{-\infty}^{\infty} I(y)dy}} \tag{2.34}$$

This definition provides a result for the case of a pure TEM_{00} mode, which is consistent with the standard definition of this radius as the radial distance at which the intensity falls to $1/e^2$ of the peak intensity.

Furthermore, by writing the complex beam parameter q in terms of the high-order mode radius [13],

$$\frac{1}{q(z)} = \frac{1}{R(z)} - \frac{iM^2\lambda}{\pi W^2(z)} \tag{2.35}$$

We can then easily obtain the expressions for beam radius and wavefront radius of curvature for the high-order mode:

$$W(z) = W_0\left[1+\left(\frac{M^2\lambda z}{\pi W_0^2}\right)^2\right]^{\frac{1}{2}} \tag{2.36}$$

$$R(z) = z\left[1+\left(\frac{\pi W_0^2}{M^2\lambda z}\right)^2\right] \tag{2.37}$$

It should be noted that the complex radius of curvature q can be applied here in the matrix methods to calculate the propagation of beams with any mix of modes, which characterize optical systems by ray transfer (ABCD) matrices. This will be discussed in more detail in Chapter 4.

2.4 Thermal modelling

As mentioned in the last chapter, thermal issues are often a serious problem that restrict laser performance in terms of output power and beam quality, which makes thermal management an essential part of solid-state laser systems, especially high-power diode-pumped lasers. Therefore, a model is investigated here to predict the effects of heat flow in a planar waveguide laser, based on a theoretical study of the slab geometry introduced by Eggleston et al. [15]. The waveguide studied here is of a five-layer structure, with sapphire as outer cladding, YAG as inner cladding, and a rare-earth doped-YAG core as heat source when optically pumped, as shown in Fig. 2.5. Taking the case of double-sided pumping, which is often applied in the experiments designed for high-power operation, the thermal load in a plane can be relatively uniform, and the composite structure can be approximated to a slab of infinite extent [15], with the thermal gradients assumed to be one-dimensional and perpendicular to the waveguide plane.

2.4.1 Temperature distribution

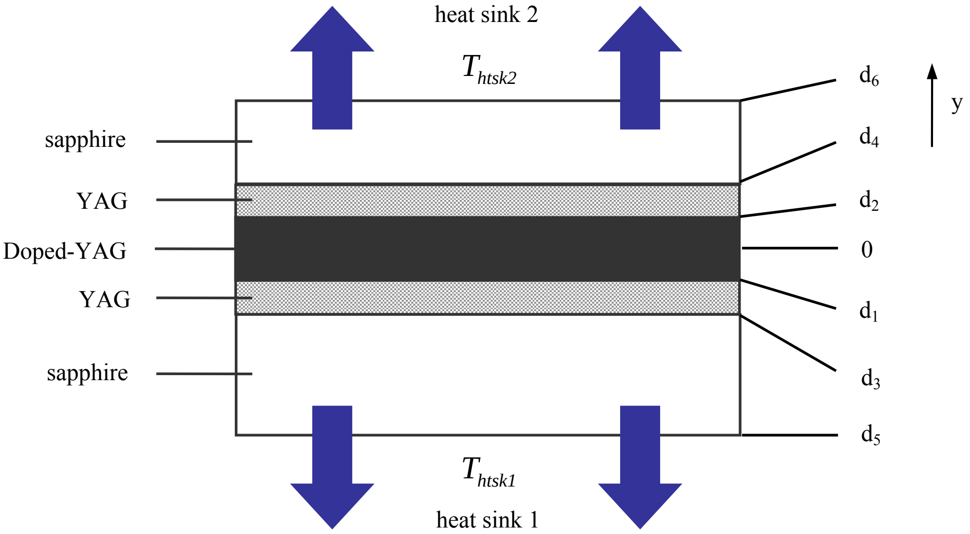

Figure 2.5 Schematic structure of a diode-side-pumped double-clad waveguide laser which has a one-dimensional temperature profile.

As shown in Fig. 2.5, the waveguide is in direct contact with the upper and lower heat sinks, which have fixed temperatures driven by cooling systems: T_{htsk2} and T_{htsk1}, respectively. To obtain the temperature profile in the waveguide, we need to solve the corresponding thermal conduction equations, combined with thermal boundary conditions, at different surfaces. In the steady state, the time-independent thermal conduction equation is written as [15],

$$\nabla^2 T(x,y,z) = \frac{-Q_T(x,y,z)}{k(x,y,z)} \tag{2.38}$$

where $Q_T(x,y,z)$ is the thermal power loading per unit volume, which is assumed to be zero except in the doped-core, $k(x,y,z)$ is the thermal conductivity, and $T(x,y,z)$ is the temperature (K).

Due to the side-pumping configuration, the temperature distribution is 1D perpendicular to the waveguide plane, so that equation (2.38) can be rewritten as,

$$\frac{\partial^2 T(y)}{\partial y^2} = -\frac{Q_T}{k(y)} \tag{2.39}$$

which can be solved as follows, with reference to the 1D structure along the y-axis in the waveguide,

$$T = \begin{pmatrix} ay+b \\ cy+d \\ ey^2 + fy + g \\ hy+i \\ jy+m \end{pmatrix} \quad \text{for} \quad \begin{pmatrix} d_4 < y < d_6 \\ d_2 < y < d_4 \\ |y| < d_2 = -d_1 \\ d_3 < y < d_1 \\ d_5 < y < d_3 \end{pmatrix} \tag{2.40}.$$

Before we write the boundary conditions, we make two assumptions about the thermal conductivity introduced in equation (2.38): (1) it is independent of temperature in the situation we discuss here, and (2) each layer of different materials is isotropic as far as the thermal conductivity is concerned, denoted by k_s, k_y, and k_{dy} for the layer of sapphire, YAG, and doped-YAG, respectively. Therefore, the thermal boundary conditions between the adjacent layers are given by,

$$\begin{cases} k_{dy}\dfrac{\partial T}{\partial y}\Big|_{d_1} = k_y \dfrac{\partial T}{\partial y}\Big|_{d_1} \\ k_{dy}\dfrac{\partial T}{\partial y}\Big|_{d_2} = k_y \dfrac{\partial T}{\partial y}\Big|_{d_2} \\ k_y\dfrac{\partial T}{\partial y}\Big|_{d_3} = k_s \dfrac{\partial T}{\partial y}\Big|_{d_3} \\ k_y\dfrac{\partial T}{\partial y}\Big|_{d_4} = k_s \dfrac{\partial T}{\partial y}\Big|_{d_4} \end{cases} \qquad T\big|_s = T_{next-layer}\big|_s \qquad (2.41).$$

The right-hand equation above represents the continuity of the temperature on either side of an infinitely thin boundary, while the left-hand equation states that the temperature gradient in adjacent layers is proportional through each layer's thermal conductivity.

By Newton's law of heat transfer, the boundary conditions on the two outer layers joined with the heat sinks are,

$$\begin{cases} k_s\dfrac{\partial T}{\partial y}\Big|_{d_5} = -\lambda_{htsk1}\,(T_{htsk1} - T\big|_{d_5}) \\ k_s\dfrac{\partial T}{\partial y}\Big|_{d_6} = -\lambda_{htsk2}\,(T_{htsk2} - T\big|_{d_6}) \end{cases} \qquad (2.42),$$

where λ_{htsk} are the surface heat transfer coefficients.

By using (2.39), one parameter in equation (2.40), e, is immediately worked out as $e = -\dfrac{Q_T}{2k_{dy}}$. When we set $Q_T = P_h / w_c l d_{core}$, where P_h is the uniformly deposited heat and $w_c l d_{core}$ is the volume of the active core of the waveguide, there is only an algebraic problem left to solve equations (2.40) to (2.42).

2.4.2 Stress distribution

The temperature distribution leads to effects such as thermal lensing, birefringence, and stress. In the absence of thermal loading, the slab is assumed to be stress-free and not constrained by external forces. Here the over-riding limitation of thermal stress fracture is calculated. When the expression for $T(y)$, detailed in equation (2.40), is obtained, another temperature distribution that characterizes a change in temperature can be derived,

$$T'(y) = T(y) - T_a \tag{2.43},$$

where T_a is the average temperature either in the whole slab along the y-axis, or averaged in each of the layers specifically, according to different requirements.

The maximum surface stress, or stress fracture limit that can be tolerated by the laser host material prior to fracture, is given by [15]

$$\sigma_{\max} = \frac{R_s \alpha_T E_Y}{(1-\nu)k} \tag{2.44},$$

where R_s is a thermal shock parameter [16], α_T is the thermal expansion coefficient, E_Y is Young's modulus, and ν is Poisson's ratio. For a uniformly pumped slab of infinite extent, the stress is found to be [15]

$$\sigma_s = \frac{\alpha_T E_Y}{(1-\nu)} T'(y) \tag{2.45}.$$

Therefore, a "safety factor" can be introduced here to express the possibility of the slab fracture by taking the ratio of equation (2.44) and (2.45)

$$F_s = \frac{\sigma_{\max}}{\sigma_s} = \frac{R_s}{kT'(y)} \tag{2.46},$$

that is, the stress fracture limit for a slab of infinite extent occurs when F_s is equal to 1. In Chapter 5, this theoretical model will be applied to calculate the temperature and stress distribution in a diode-stack side-pumped planar waveguide, analysing the experimental case of fracture, and allowing prediction for power scaling.

2.5 Waveguide theory

Guidance of light can occur due to total internal reflection (TIR) in a waveguide core when the refractive index of the core is higher than that of the substrate or cladding.

Therefore the light beam that is coupled to the end face of the waveguide is confined in the core, as shown in Fig. 2.6.

Figure 2.6 **Basic structure of an optical waveguide.**

The condition for total internal reflection inside the waveguide geometry is provided by Snell's law. With the assumption that $n_3 \geq n_1$, we obtain the critical angle for wave guiding,

$$\theta_c = \sin^{-1}(n_3/n_2) \qquad (2.47),$$

where n_1, n_2, and n_3 are refractive indices of the cladding, core and substrate, respectively. The angle θ_g ($\theta_g \geq \theta_c$ for the light to be guided in the core) is related to the incident angle θ_i by

$$n_0 \sin\theta_i = n_2 \sin(\pi/2 - \theta_g) \leq n_2 \sin(\pi/2 - \theta_c) = n_2 \cos\theta_c \qquad (2.48).$$

When we rewrite the right hand part of the above equation as,

$$n_2 \cos\theta_c = n_2(1 - \sin^2\theta_c)^{1/2} = n_2(1 - n_3^2/n_2^2)^{1/2} = (n_2^2 - n_3^2)^{1/2} \qquad (2.49),$$

the maximum acceptance angle $\theta_{\max}$, for launching the light into the waveguide, can be obtained,

$$\theta_{\max} = \sin^{-1}(\sqrt{n_2^2 - n_3^2}/n_0) \qquad (2.50).$$

The refractive index difference between the core and the cladding is normally small and $n_0 = 1$ when the outer region is air, in which case $\theta_{\max}$ can be approximated by

$$\theta_{\max} \cong \sqrt{n_2^2 - n_3^2} \equiv NA \tag{2.51}$$,

where NA is known as the numerical aperture. It can be calculated then that a YAG/sapphire guide structure gives an $NA = 0.46$.

2.5.1 Maxwell's equations

To analyze the wave propagation inside a waveguide in more detail, it is necessary to use electromagnetic theory. We will start with Maxwell's equations. For an isotropic and lossless dielectric medium, Maxwell's equations are written in terms of the electric field E and magnetic field H as [17],

$$\nabla \times E = -\mu \frac{\partial H}{\partial t} \qquad \nabla \times H = \varepsilon \frac{\partial E}{\partial t} \tag{2.52, 53}$$

$$\nabla \cdot E = 0 \qquad \nabla \cdot H = 0 \tag{2.54, 55}$$,

where ε and μ denote the permittivity and permeability of the medium, respectively.

When we consider an electromagnetic wave having angular frequency ω and propagating in the z direction with propagation constant k_z, the electric and magnetic fields can be expressed as [18],

$$E(x, y, z, t) = E(x, y)e^{i(\omega t - k_z z)} \tag{2.56}$$

$$H(x, y, z, t) = H(x, y)e^{i(\omega t - k_z z)} \tag{2.57}$$

where (x, y) denotes the position in the plane transverse to the z-axis, and $E(x, y)$ and $H(x, y)$ are the x and y dependence of the electric, and magnetic field function of a guided mode, respectively.

In the planar waveguide, as shown in Fig. 2.7, electromagnetic fields E and H do not have x-axis dependency. Therefore, we set $\partial E/\partial x = 0$ and $\partial H/\partial x = 0$. Putting these relations into (2.52, 53) and (2.56, 57), two independent electromagnetic modes are obtained, which are denoted as TE mode and TM mode, respectively.

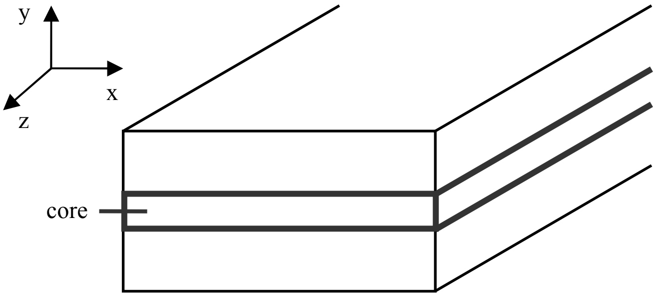

Figure 2.7 Planar optical waveguide structure.

The TE mode satisfies the following wave equation:

$$\frac{\partial^2 E_x}{\partial y^2} + (\mu\varepsilon\omega^2 - k_z^2)E_x = 0 \tag{2.58}$$

where $$E_x = -\frac{\mu\omega}{k_z}H_y \qquad \frac{\partial E_x}{\partial y} = -i\mu\omega H_z \tag{2.59, 60}$$

$$E_y = E_z = H_x = 0 \tag{2.61}$$,

where E_x, E_y, E_z are x, y, and z-components of E respectively, while the same definition applies to H. As shown in (2.61), since the electric field component along the z-axis is zero, which means the electric field lies in the plane that is perpendicular to the z-axis, this electromagnetic field distribution is called the transverse electric (TE) mode.

Similarly, the transverse magnetic (TM) mode satisfies the following wave equation:

$$\frac{\partial^2 H_x}{\partial y^2} + (\mu\varepsilon\omega^2 - k_z^2)H_x = 0 \tag{2.62}$$

where $$H_x = \frac{\varepsilon\omega}{k_z}E_y \qquad \frac{\partial H_x}{\partial y} = i\varepsilon\omega E_z \tag{2.63, 64}$$

$$E_x = H_y = H_z = 0 \tag{2.65}$$.

2.5.2 A general asymmetric slab waveguide model

The solution for the asymmetric waveguide geometry, illustrated in Fig. 2.8, is explored first and will immediately be applied in the work reported in later chapters. Due to duality conditions [17], only the derivation for the *TE* modes will be presented, followed by the direct result of the *TM* solutions.

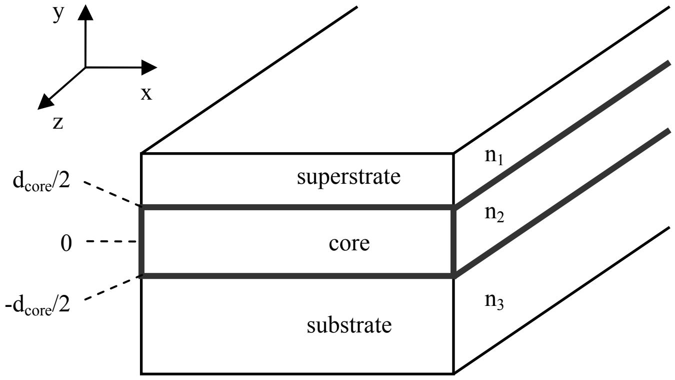

Figure 2.8 An asymmetric waveguide structure.

As shown in Fig. 2.8, this asymmetric slab waveguide is assumed to have infinite extension in the x and z axes. The superstrate region, referred to as region 1, is often air, which is characterised by ε_1 and μ_1; the higher refractive index guiding core (region 2) has a small depth d_{core} (ε_2 and μ_2); and region 3 is the substrate which may be considered essentially infinite in thickness, characterised by ε_3 and μ_3.

2.5.2.1 TE modes

The solutions for E_x in the separate waveguide regions can be proposed, assuming that the solutions decay exponentially outside of the core region and form standing waves inside the core [19],

$$E_x(y,z) = \begin{Bmatrix} A_1 e^{-\alpha_{1y} y} \\ A_2 \cos(k_{2y} y + \psi) \\ A_3 e^{\alpha_{3y} y} \end{Bmatrix} e^{-ik_z z} \quad \begin{matrix} y \geq d_{core}/2 \\ |y| \leq d_{core}/2 \\ y \leq -d_{core}/2 \end{matrix} \qquad (2.66).$$

A_1 - A_3 are constants; α_{1y} and α_{3y} are the decay coefficients in regions 1 and 3; k_{2y} is the y-axis wave vector within the core; and ψ denotes the offset of the peak intensity from the centre of the core for region 2. The definitions of the dispersion relations for α_{1y}, k_{2y} and α_{3y} can be revealed by simply substituting (2.66) into (2.58),

$$\alpha_{1y} = \sqrt{k_z^2 - \mu_1\varepsilon_1\omega^2} \tag{2.67}$$

$$k_{2y} = \sqrt{\mu_2\varepsilon_2\omega^2 - k_z^2} \tag{2.68}$$

$$\alpha_{3y} = \sqrt{k_z^2 - \mu_3\varepsilon_3\omega^2} \qquad (2.69).$$

The tangential component of the H-field H_z can be obtained directly from (2.60),

$$H_z(y,z) = \begin{Bmatrix} -\dfrac{i\alpha_{1y}}{\omega\mu_1} A_1 e^{-\alpha_{1y}y} \\ -\dfrac{ik_{2y}}{\omega\mu_2} A_2 \sin(k_{2y}y + \psi) \\ \dfrac{i\alpha_{3y}}{\omega\mu_3} A_3 e^{\alpha_{3y}y} \end{Bmatrix} e^{-ik_z z} \quad \begin{matrix} y \geq d_{core}/2 \\ |y| \leq d_{core}/2 \\ y \leq -d_{core}/2 \end{matrix} \qquad (2.70).$$

The tangential components of E and H must be continuous at the region interfaces [19], which can be applied at the boundary $y = d_{core}/2$:

$$E_{\tan} = E_x: \qquad A_1 e^{-\alpha_{1y} d_{core}/2} = A_2 \cos(k_{2y} d_{core}/2 + \psi) \tag{2.71}$$

$$H_{\tan} = H_z: \qquad A_1 e^{-\alpha_{1y} d_{core}/2} = \frac{\mu_1 k_{2y}}{\mu_2 \alpha_{1y}} A_2 \sin(k_{2y} d_{core}/2 + \psi) \qquad (2.72).$$

Taking the ratio of (2.71) and (2.72) to eliminate A_1 and A_2, gives

$$\frac{\mu_2\alpha_{1y}}{\mu_1 k_{2y}} = \tan(k_{2y} d_{core}/2 + \psi) \qquad (2.73),$$

while similarly at $y = -d_{core}/2$

$$\frac{\mu_2 \alpha_{3y}}{\mu_3 k_{2y}} = \tan(k_{2y}\, d_{core}/2 - \psi) \qquad (2.74).$$

Using the fact that $\tan(x) = \tan(x \pm m\pi)$, where m is an integer, after some rearrangements the TE mode guidance condition for an asymmetric waveguide can be expressed as:

$$k_{2y} d_{core} - \tan^{-1}\left(\frac{\mu_2 \alpha_{1y}}{\mu_1 k_{2y}}\right) - \tan^{-1}\left(\frac{\mu_2 \alpha_{3y}}{\mu_3 k_{2y}}\right) = p\pi \qquad p = 0,1,... \qquad (2.75).$$

This guidance condition can then be solved numerically.

Once the guidance condition has been solved for a particular mode, the corresponding fields in all the three regions can be obtained:

$$E_x(y,z) = A_2 \begin{Bmatrix} \cos(k_{2y}\, d_{core}/2 + \psi) e^{-\alpha_{1y}(y - d_{core}/2)} \\ \cos(k_{2y} y + \psi) \\ \cos(k_{2y}\, d_{core}/2 - \psi) e^{\alpha_{3y}(y + d_{core}/2)} \end{Bmatrix} e^{-ik_z z} \qquad \begin{matrix} y \geq d_{core}/2 \\ |y| \leq d_{core}/2 \\ y \leq -\, d_{core}/2 \end{matrix} \qquad (2.76)$$

by relating A_1 - A_3 by the boundary conditions at $y = \pm\, d_{core}/2$.

2.5.2.2 TM modes

The solutions for TM modes are obtained directly by making use of duality: $E \to -H$, $H \to E$, $\mu \to \varepsilon$, $\varepsilon \to \mu$. The TM mode guidance condition for an asymmetric waveguide can then be written as

$$k_{2y} d_{core} - \tan^{-1}\left(\frac{\varepsilon_2 \alpha_{1y}}{\varepsilon_1 k_{2y}}\right) - \tan^{-1}\left(\frac{\varepsilon_2 \alpha_{3y}}{\varepsilon_3 k_{2y}}\right) = p\pi \qquad p = 0,1,... \qquad (2.77),$$

and the resulting fields are given by

$$H_x(y,z) = A_2 \begin{Bmatrix} \cos(k_{2y}\, d_{core}/2 + \psi') e^{-\alpha_{1y}(y - d_{core}/2)} \\ \cos(k_{2y} y + \psi') \\ \cos(k_{2y}\, d_{core}/2 - \psi') e^{\alpha_{3y}(y + d_{core}/2)} \end{Bmatrix} e^{-ik_z z} \qquad \begin{matrix} y \geq d_{core}/2 \\ |y| \leq d_{core}/2 \\ y \leq -\, d_{core}/2 \end{matrix} \qquad (2.78),$$

where ψ' is the offset given by the dual of either equation (2.73) or (2.74).

2.5.2.3 The symmetric slab waveguides

When $\varepsilon_1 = \varepsilon_3$ and $\mu_1 = \mu_3$, which also gives $\alpha_{1y} = \alpha_{3y}$ by equations (2.67) and (2.69), the planar waveguide shown in Fig. 2.8 becomes a symmetric slab structure. The following relations are obtained using equations (2.73) and (2.74),

$$k_{2y}\, d_{core}/2 + \psi = \tan^{-1}\left(\frac{\mu_2 \alpha_{1y}}{\mu_1 k_{2y}}\right) \pm m\pi \tag{2.79}$$

$$k_{2y}\, d_{core}/2 - \psi = \tan^{-1}\left(\frac{\mu_2 \alpha_{1y}}{\mu_1 k_{2y}}\right) \pm n\pi \qquad (2.80),$$

where m and n are both integers. The guidance condition for TE modes can then be produced:

$$\frac{k_{2y} d_{core}}{2} - \tan^{-1}\left(\frac{\mu_2 \alpha_{1y}}{\mu_1 k_{2y}}\right) = p\pi \quad p = 0,1,... \quad \text{(even modes)} \tag{2.81}$$

$$\frac{k_{2y} d_{core}}{2} + \cot^{-1}\left(\frac{\mu_2 \alpha_{1y}}{\mu_1 k_{2y}}\right) = p\pi \quad p = 0,1,... \quad \text{(odd modes)} \qquad (2.82).$$

After substituting (2.81) and (2.82) into (2.80), the offset ψ is either $p\pi \mp n\pi$ (for even modes) or $\pi/2 + p\pi \mp n\pi$ (for odd modes), with which the electric fields in (2.76) can be given for even and odd modes, respectively:

$$\text{Even modes: } E_x(y,z) = A_2 \left\{ \begin{matrix} \cos(k_{2y}\, d_{core}/2) e^{-\alpha_{1y}(y - d_{core}/2)} \\ \cos(k_{2y} y) \\ \cos(k_{2y}\, d_{core}/2) e^{\alpha_{1y}(y + d_{core}/2)} \end{matrix} \right\} e^{-ik_z z} \quad \begin{matrix} y \geq d_{core}/2 \\ |y| \leq d_{core}/2 \\ y \leq -d_{core}/2 \end{matrix} \tag{2.83}$$

$$\text{Odd modes: } E_x(y,z) = A_2 \left\{ \begin{matrix} \sin(k_{2y}\, d_{core}/2) e^{-\alpha_{1y}(y - d_{core}/2)} \\ \sin(k_{2y} y) \\ \sin(k_{2y}\, d_{core}/2) e^{\alpha_{1y}(y + d_{core}/2)} \end{matrix} \right\} e^{-ik_z z} \quad \begin{matrix} y \geq d_{core}/2 \\ |y| \leq d_{core}/2 \\ y \leq -d_{core}/2 \end{matrix} \qquad (2.84).$$

Again, the symmetry in Maxwell's equations will immediately lead to the TM mode guidance condition and field results, which are omitted here for simplicity.

It should be noted that the slab waveguide modelling discussed in this section forms the basis of the modelling to be applied in Chapter 4, in which a five-layer slab waveguide is analysed and its mode-selection properties are investigated.

2.5.3 A graded-index asymmetric waveguide model

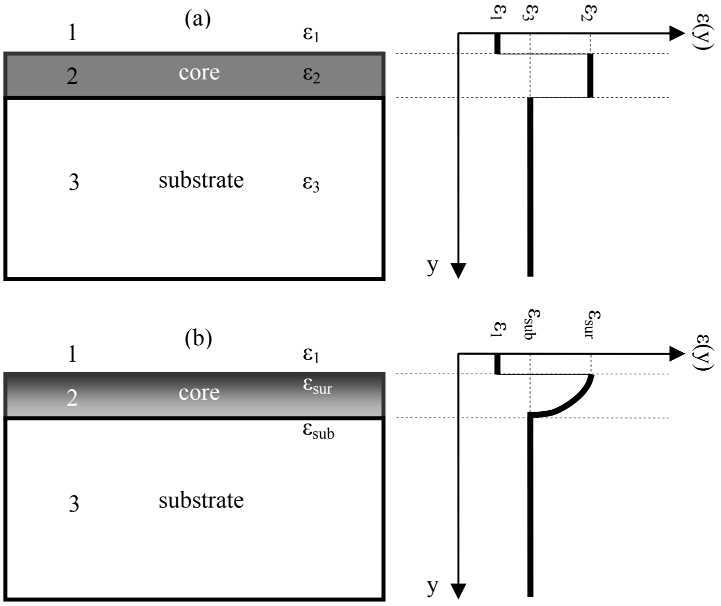

Figure 2.9 Permittivity (refractive index) profile of (a) a step-index waveguide structure and (b) a graded-index asymmetric waveguide structure.

In the last section, the asymmetric slab waveguide model has a step-index guiding structure that is usually a representation of the type of waveguides fabricated by the conjunction of two types of materials (such as techniques of bonding and deposition, for example, which will be stated in Chapter 4-6). For this structure, the permittivity is constant except for sudden discontinuities at interfaces, as illustrated in Fig. 2.9 (a).

For waveguides fabricated by material modification such as the ion-exchange technique, the fabrication process will produce a smooth and continuous variation in ε with increasing depth into the substrate, as shown in Fig. 2.9 (b), which is referred to as a graded-index guiding structure. The WKB method [20] can be used to calculate the propagation constant and transverse field variation approximately for each guided mode within a graded-index planar waveguide, and is therefore described here for its practical importance to the ion-exchanged waveguides investigated in Chapter 3.

In the waveguide core, the variation in permittivity $\varepsilon(y)$ along the y-axis results in the variation in refractive index, which is related to the permittivity through

$$n(y) = \sqrt{\varepsilon(y)/\varepsilon_0} \tag{2.85}$$

when we assume $\mu(y) = \mu_0$, and to represent this y-dependence of the permittivity the dispersion relation is given by:

$$k_y(y) = \sqrt{\omega^2 \mu\varepsilon(y) - k_z^2} \tag{2.86}.$$

If we intend to make an analogy with the guidance condition developed in section 2.5.2, certain boundaries need to be first identified for the “core region” of this graded-index waveguide, so that it can be expected that the fields should be oscillatory within the core and decay exponentially to either side, like the slab waveguides.

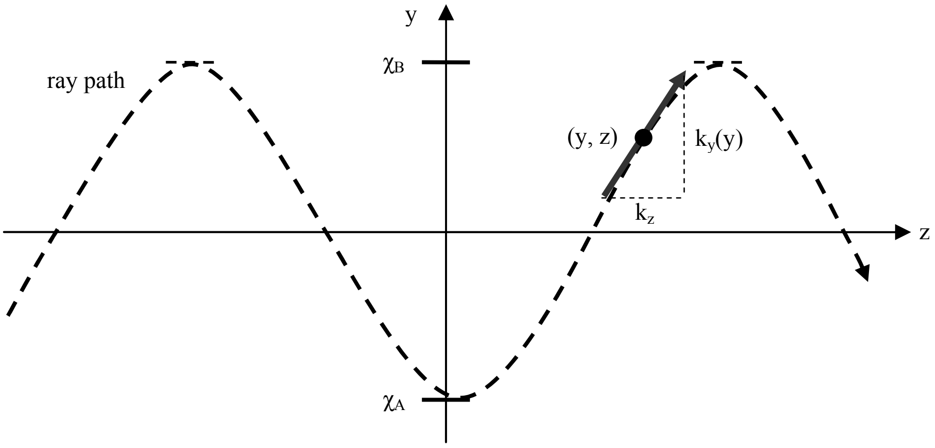

Figure 2.10 Ray path through a graded-index asymmetric waveguide. χ_A and χ_B are the boundary positions along the y-axis where the ray is parallel to the z-axis [20].

A guided mode within the core is related to a wave vector $k(y)$, which is defined as

$$k^2(y) \equiv k_y^2(y) + k_z^2 = \omega^2 \mu\varepsilon(y) \tag{2.87}.$$

The relations among $k(y)$, $k_y(y)$ and k_z are shown in Fig. 2.10 [20] schematically.

Hence, equation (2.86) can be rearranged as

$$k_y(y) = k_0\sqrt{n^2(y) - n_{eff}^2} \quad (2.88),$$

where $k_0 = \omega\sqrt{\mu_0\varepsilon_0}$ is the wave vector in free space and $n_{eff} = k_z/k_0$ is the effective refractive index experienced by the guided mode, which is defined below.

As shown in Fig. 2.10, the effective boundaries χ_A and χ_B are observed to be the positions along the y-axis where the ray is parallel to the z-axis,

$$k_y(\chi_A) = k_y(\chi_B) = 0 \quad (2.89).$$

Correspondingly, the effective refractive index satisfies the following:

$$\begin{array}{lccl} n(y) > n_{eff} & & \chi_A < y < \chi_B & \textit{region R} \\ n(\chi_A) = n(\chi_B) = n_{eff} & \text{for} & y = \chi_A, y = \chi_B & \textit{boundaries} \\ n(y) < n_{eff} & & y < \chi_A, y > \chi_B & \textit{region I} \end{array} \quad (2.90).$$

When equation (2.90) is substituted into equation (2.88), it can be seen that $k_y(y)$ turns from purely real in region "R" to purely imaginary in region "I" at the turning points χ_A and χ_B, which satisfies the expectation that the fields should decay exponentially beyond certain boundaries, as happens outside the core region of the slab waveguide.

Therefore, when the analogy is made with the slab waveguide, the guidance condition of the graded-index waveguide is supposed to adopt the form of

$$2k_{2y}d_{core} - \varphi_1 - \varphi_3 = 2p\pi \quad (2.91),$$

where $2k_{2y}d_{core}$ represents the phase change along the y-axis due to propagation within the waveguide, and φ_1 and φ_3 are the additional phase shifts resulting from total internal reflection at the two dielectric interfaces.

With this model, the guidance condition should be expressed as

$$2\int_{\chi_A}^{\chi_B} k_{2y}(y)dy - \varphi_1 - \varphi_3 = 2p\pi \qquad (2.92),$$

in order to take into account the y-axis variation in k_{2y} (the subscript "2" denotes region 2) and the equivalent core region of the graded-index waveguide set by χ_A and χ_B. For φ_1 and φ_3, analogy can also be made from equation (2.75), see ref. [20].

For graded-index waveguides with a maximum refractive index at the core-air surface, as shown in Fig. 2.9 (b), the first effective boundary χ_A can be set to be zero [21], and then only χ_B is left to be found. It should be underlined here that the boundary χ_B is different for each mode of the waveguide, with higher-order modes producing successively greater values of χ_B. Thus, in graded-index waveguides higher-order modes effectively experience larger core sizes and therefore their spatial extent can be significantly different from that of the fundamental mode, whereas in step-index slab waveguides all the modes have equal-sized core boundaries and are of similar spatial extent.

This graded-index waveguide modelling is useful for the waveguides in Chapter 3, in which a graded refractive index structure is fabricated via the ion-exchange process. However, in general the modal analysis of such waveguides is more complicated as the core boundaries are not so clearly defined and the modes are normally calculated by numerical methods.

2.6 References

[1] W. P. Risk, "Modeling of longitudinally pumped solid-state lasers exhibiting reabsorption losses," Journal of the Optical Society of America B-Optical Physics, vol. 5, pp. 1412-1423, Jul 1988.

[2] R. J. Beach, "CW Theory of quasi-three level end-pumped laser oscillators," Optics Communications, vol. 123, pp. 385-393, Jan 15 1995.

[3] K. Kubodera and K. Otsuka, "Single-transverse-mode $LiNdP_4O_{12}$ slab waveguide laser," Journal of Applied Physics, vol. 50, pp. 653-659, Feb 1979.

[4] L. W. Casperson, "Laser power calculations: sources of error," Applied Optics, vol. 19, pp. 422-434, 1980.

[5] D. G. Hall, R. J. Smith, and R. R. Rice, "Pump-size effects in Nd:YAG lasers," Applied Optics, vol. 19, pp. 3041-3043, Sep 15 1980.

[6] M. J. F. Digonnet and C. J. Gaeta, "Theoretical-analysis of optical fiber laser-amplifiers and oscillators," Applied Optics, vol. 24, pp. 333-342, 1985.

[7] T. Y. Fan and R. L. Byer, "Modeling and CW operation of a quasi-three-level 946 nm Nd:YAG laser," IEEE Journal of Quantum Electronics, vol. 23, pp. 605-612, May 1987.

[8] T. Bhutta, J. I. Mackenzie, and D. P. Shepherd, "Spatial dopant profiles for transverse-mode selection in multimode waveguides," Journal of the Optical Society of America B-Optical Physics, vol. 19, pp. 1539-1543, Jul 2002.

[9] C. L. Bonner, T. Bhutta, D. P. Shepherd, and A. C. Tropper, "Double-clad structures and proximity coupling for diode-bar-pumped planar waveguide lasers," IEEE Journal of Quantum Electronics, vol. 36, pp. 236-242, Feb 2000.

[10] W. A. Clarkson and D. C. Hanna, "Effects of transverse-mode profile on slope efficiency and relaxation oscillations in a longitudinally-pumped laser," Journal of Modern Optics, vol. 36, pp. 483-498, Apr 1989.

[11] J. I. Mackenzie, C. Li, D. P. Shepherd, R. J. Beach, and S. C. Mitchell, "Modeling of high-power continuous-wave Tm:YAG side-pumped double-cad waveguide lasers," IEEE Journal of Quantum Electronics, vol. 38, pp. 222-230, Feb 2002.

[12] W. Koechner, Solid-state laser engineering - Chapter 5, 5th ed. vol. 1: Springer-Verlag Berlin Heidelberg New York, 1999.

[13] D. R. Hall and P. E. Jackson, The physics and technology of laser resonators - Chapter 9: IOP Publishing, 1989.

[14] A. E. Siegman, "How to (maybe) measure laser beam quality," in Optical Society of America Annual Meeting Long Beach, California, 1997.

[15] J. M. Eggleston, T. J. Kane, K. Kuhn, J. Unternahrer, and R. L. Byer, "The slab geometry laser---part 1: Theory," IEEE Journal of Quantum Electronics, vol. 20, pp. 289-301, 1984.

[16] W. Koechner, Solid-state laser engineering - Chapter 7, 5th ed. vol. 1: Springer-Verlag Berlin Heidelberg New York, 1999.

[17] D. L. Lee, Electromagnetic principles of integrated optics - Chapter 2: John Wiley & Sons, 1986.

[18] K. Okamoto, Fundamentals of optical waveguides - Chapter 1: Academic Press, 2000.

[19] D. L. Lee, Electromagnetic principles of integrated optics - Chapter 4: John Wiley & Sons, 1986.

[20] D. L. Lee, Electromagnetic principles of integrated optics - Chapter 5: John Wiley & Sons, 1986.

[21] G. B. Hocker and W. K. Burns, "Modes in diffused optical waveguides of arbitrary index profile," IEEE Journal of Quantum Electronics, vol. 11, pp. 270-276, Jun 1975.

Chapter 3

Tapered waveguide lasers

3.1 Introduction

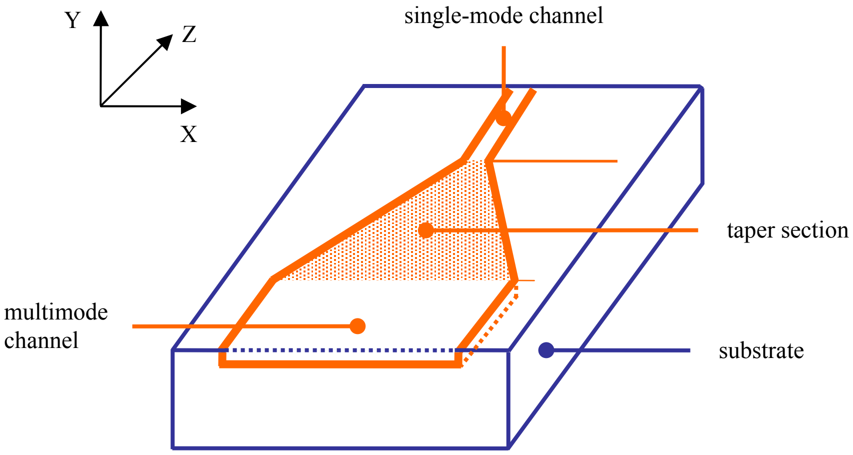

Figure 3.1 Schematic diagram of a tapered waveguide.

High-power diode pumping requires a large multi-spatial-mode planar waveguide to achieve efficient coupling, which in turn leads to non-diffraction-limited laser output. Conversely, the single-mode channel waveguide geometry is a common solution to obtain diffraction-limited operation through its two-dimensional optical confinement, but would have an inevitably poor high-power-diode-to-waveguide coupling. A logical step would therefore be to take advantage of both the multimode planar and single-mode channel waveguide geometries in a single optical device. However, the direct combining of multimode planar (or broad channel) and single-mode channel waveguides will result in large coupling losses due to the dramatic difference in mode sizes between the two sections. An immediate solution is the use of a tapered waveguide structure [1], which adiabatically expands a single-mode channel up to a broad multimode channel, as shown in Fig. 3.1. Diode pumping is allowed at the multimode wide end with a shape matched to the pump radiation, whereas fundamental-mode laser output is ensured at the narrow end by carefully designing the channel to select only a single mode at the laser wavelength.

The “adiabatic operation” stated above is the fundamental requirement of the interconnecting taper. It demands that the fundamental lasing mode supported by the narrow channel be converted into a mode of greater lateral size in the broad channel, without losing power coupled to higher-order modes, which can be possibly accomplished through proper design of the taper structure [2, 3] (see more details in section 3.2). A reasonable overlap is possible between the fundamental laser mode of the broad channel at the laser wavelength and the launched multimode pump radiation, thereby achieving efficient laser operation [4, 5].

Tapers are important elements that are necessary for many optical applications. They have been used to improve coupling between diodes and fibre optics [6] or channel waveguides [7], and have been found useful within fibre lasers [8] to produce single-transverse-mode laser operation. In integrated optical devices tapers offer an excellent means of converting optical mode sizes [9, 10] to connect optical devices of different cross-sectional dimensions. Furthermore, in planar devices they could take the place of integrated lenses in order to transform a confined field into a collimated beam. Due to the taper design considerations in the following sections, these taper structures are compatible with multi-watt broad-stripe diode end-pumping. The capability to fabricate these structures on planar chips makes them compatible with integrated optical circuits, power-scalable to 1-Watt level with broad-stripe diode pumping, at very interesting wavelengths such as Yb^{3+} doped lasers operating at around 980nm to act as pump sources for erbium doped amplifiers, or Er^{3+} doped lasers at around 1550nm of high interest in telecommunications. The higher power regime for planar waveguides pumped by diode bars/stacks will be discussed in Chapter 4-6.

3.2 Theoretical study

3.2.1 Tapered waveguide theory

The concept of using tapered waveguides to couple from planar to channel waveguides is well established in integrated optics and various designs have been investigated so far, including linear, parabolic, and exponential expansions. The design of the coupling taper structure should be based on considerations of both expected adiabatic operation through the taper structure and the desire to obtain minimum taper length that is necessary for compact optical devices. Here a two-dimensional channel waveguide of width W with a 1D expansion is shown in Fig. 3.2, with a ray model to describe the mode propagation.

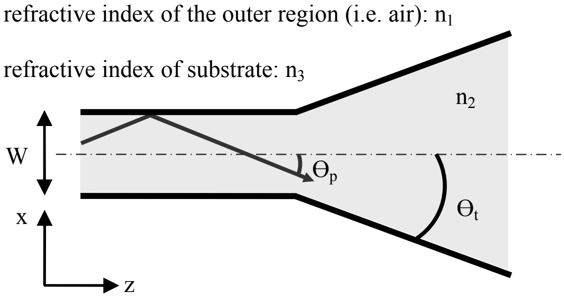

Figure 3.2 Ray path within a two-dimensional tapered waveguide.

As shown in Fig. 3.2, n_1, n_2 and n_3 are the refractive indices of the outer region, waveguide core and substrate respectively, and a parameter Δn is defined as the index difference between n_2 and n_3. θ_p is defined as the projection angle of the ray of the fundamental mode in the waveguide plane. θ_t is the angle of the taper barrier with the axis of the channel z. We follow the ray model of Burns *et al.* [11], based on the effective index method [12].

From [11], the projection of the ray angle can be derived as:

$$\cos\theta_p = \frac{n_3 + \Delta n b b'}{n_3 + \Delta n b} \tag{3.1}$$,

where the variables b and b' are the normalised mode effective indices, defined by

$$b = \frac{n_{eff}^2 - n_3^2}{n_2^2 - n_3^2} \qquad b' = \frac{n_{eff}'^2 - n_3^2}{n_{eff}^2 - n_3^2} \tag{3.2, 3}$$.

Here $n_{eff}'^2$ is the effective index of the fundamental mode in the channel waveguide with finite width W, while n_{eff}^2 is the effective index of the fundamental mode within a planar waveguide of equal depth ($W \to \infty$).

A new parameter V' [12] is defined as the normalised guide width,

$$V' = k_0 W (n_{eff}^2 - n_3^2)^{1/2} \tag{3.4}$$,

where $k_0 = 2\pi/\lambda_0$ is the free-space wave vector, and V' is analogous to the normalised guide depth V in the $y-z$ plane for a waveguide with a core depth d_{core},

$$V = k_0 d_{core} (n_2^2 - n_3^2)^{1/2} \tag{3.5}$$.

It should be pointed out here that, with the effective index method [12], analogous derivation can be made to alter from the $y-z$ plane fields investigated in Chapter 2 to the $x-z$ plane explored here by $n_{eff} \to n'_{eff}$, $n_2 \to n_{eff}$, $b \to b'$ and $V \to V'$.

By substituting b' and V' into equation (2.81), as the waveguide structure is symmetric in the $x-z$ plane, the guidance condition for the fundamental mode ($p = 0$) of the channel waveguide can be derived, aided by the analogy above, to relate b' and W,

$$V'(1-b')^{1/2} = 2\tan^{-1}\left(\frac{b'}{1-b'}\right)^{1/2} \tag{3.6}$$,

through the steps

$$k_{2x} W = k_0 W \sqrt{n_{eff}^2 - n_{eff}'^2} = V'(1-b')^{1/2} \tag{3.7}$$

$$2\tan^{-1}\left(\frac{\mu_2\alpha_{3x}}{\mu_3 k_{2x}}\right) = 2\tan^{-1}\sqrt{\frac{n'^2_{eff} - n_3^2}{n_{eff}^2 - n'^2_{eff}}} = 2\tan^{-1}\left(\frac{b'}{1-b'}\right)^{1/2} \qquad (3.8).$$

Since the index difference Δn is small (the order of 10^{-3} for the ion exchange process that is applied in this chapter), the ray angle in equation (3.1) is then approximated as,

$$\theta_p \approx \left[\frac{2\Delta nb}{n_3}(1-b')\right]^{1/2} \qquad (3.9).$$

Substitute (3.4) and (3.6) into equation (3.9), and after some rearrangements the ray angle can be written as

$$2\theta_p = \frac{\lambda_0}{n_3 W}\left(\frac{2n_3}{n_2+n_3}\right)^{1/2}\left(\frac{\tan^{-1}[b'/(1-b')]^{1/2}}{\frac{\pi}{2}}\right) \qquad (3.10).$$

With the consideration of the small index difference between the core and substrate again, the equation above can be rewritten as

$$2\theta_p = \frac{\lambda_0}{n_3 W}\left(\frac{\tan^{-1}[b'/(1-b')]^{1/2}}{\frac{\pi}{2}}\right) \qquad (3.11).$$

With the ray approaching along the waveguide, the expanding width W starts to increase and $n'_{eff} \rightarrow n_{eff}$, so that $b' \rightarrow 1$. Therefore, the term in the brackets in the equation above approaches unity. Thus, for well-confined modes far from cut-off, the projection of the ray angle can then be approximated as

$$\theta_p = \frac{\lambda_0}{2n_3 W} \qquad (3.12).$$

To ensure the adiabatic operation within the waveguide, the taper angle θ_t should not exceed the ray angle θ_p, otherwise the ray would not "see" the taper barrier, resulting in no guidance in the waveguide and therefore mode conversion from the fundamental mode. Hence, a design criterion is given here to relate the projection angle and the taper angle:

$$\theta_t(z) = \alpha\theta_p(z) \tag{3.13}$$

where α is a constant defined as the expansion coefficient of the structure and both the angles are dependent on the local position. It is recommended [2] that for adiabatic operation the expansion coefficient should be equal to or less than unity as values greater than this will cause coupling to higher-order modes.

Combining equations (3.12) and (3.13) gives

$$\theta_t = \frac{\alpha\lambda_0}{2n_3W} \tag{3.14}$$

which describes the relationship between the taper angle and the waveguide width and suggests that the taper diverges more slowly than diffraction from an aperture of width W.

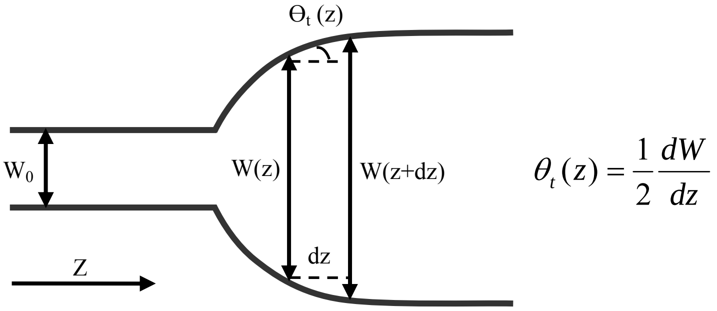

Figure 3.3 Rate of change of waveguide width with the taper angle.

As shown in Fig. 3.3, since $\theta_t = (1/2)(dW/dz)$, the rate of waveguide width W can be given by

$$\frac{dW}{dz} = \frac{\alpha\lambda_0}{n_3W} \tag{3.15}$$

After integration the width W performs a parabolic formation

$$W^2 = \frac{2\alpha\lambda_0}{n_3} z + W_0^2 \qquad (3.16),$$

where W_0 is the initial channel width of the waveguide for $z = 0$.

If the maximum taper width $W_{\max}$ is large enough so that the initial channel width W_0 can be neglected ($W_{\max} >> W_0$), the length of the optimum parabolic taper can be described as (where $z = L$),

$$L \approx \frac{n_3 W_{\max}^2}{2\alpha\lambda_0} \qquad (3.17),$$

which relates the length of the taper to its maximum width. Parabolic tapers can now be designed using equations (3.16) and (3.17) for a chosen value of α. For reasonable device lengths of a few centimetres, this implies that maximum widths of a few hundred microns are feasible, which should be compatible with high-brightness broad-stripe diode pumping.

Milton and Burns showed via mode-coupling theory [2] that the parabolic taper shape, suggested by this simple ray tracing model, offers a reasonably adiabatic solution for $\alpha \leq 1$. Nevertheless, the first experimental presentation of an ion-exchanged tapered-waveguide laser opened up from 2.5μm to 175μm over just 12.5mm (equivalent to $\alpha = 1.75$ for a parabolic design) and was linear in design. Nevertheless, it gave an adiabatic expansion with low-loss operation [1].

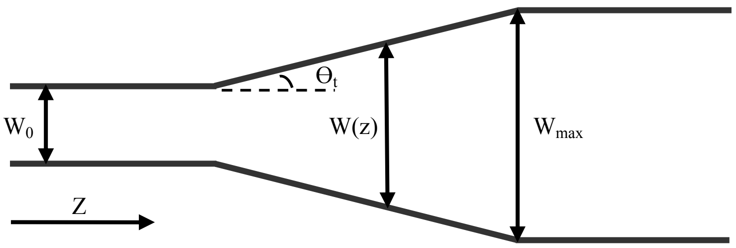

Figure 3.4 A schematic diagram for the linear tapered waveguide structure.

Linear tapers have been investigated by Duport er. al. [3] and give another option for the waveguide design. The width of the taper increases linearly with the propagation distance, as shown in Fig. 3.4, and can be therefore expressed as

$$W(z) = W_0 + 2z\tan\theta_t = W_0 + 2z(W_{\max} - W_0)/L \qquad (3.18),$$

where L is the taper length.

This taper structure was analysed in [3] using the standard Beam Propagation Method (BPM), which showed that linear tapers with θ_t less than 0.77° ($W_0 = 10.8\mu m$, $W_{\max} = 40\mu m$, $\Delta n = 0.0064$) allow adiabatic operation at a wavelength of 0.78µm with a coupling of 94% between the fundamental mode of the input and output ends.

3.2.2 Design of the tapered waveguides

In this thesis, both the linear and parabolic tapered waveguides were characterised experimentally in order to find the more efficient design for high-power 1W-level integrated laser sources. The linear and parabolic tapers expand to various widths over the same lengths along with standard channel waveguides on the same substrate, designed according to equations (3.19) and (3.20), respectively. These two equations satisfy the condition given by equation (3.17) if the maximum taper width is large enough such that $W_{\max} >> W_0$.

$$W_p(z) = \sqrt{\frac{2\alpha\lambda_0}{n_3}z + W_0^2} \qquad (3.19)$$

$$W_l(z) = \frac{2\alpha\lambda_0\left(W_{\max} - W_0\right)}{n_3 W_{\max}^2}z + W_0 \qquad (3.20).$$

Except for the geometrical restrictions outlined here for adiabatic operation, it is also necessary to include pump considerations in the waveguide design, in order to make the planar section of the waveguide compatible with multi-watt broad-stripe diode end-pumping. Assuming that the waveguide is a step-index structure, the maximum size of the waveguide taper section required to confine the non-diffraction-limited slow axis (denoted as x-axis in this thesis, and the fast axis denoted as y-axis likewise) of a broad-stripe diode can be calculated by [13]:

$$W_{\max} \geq \frac{M_x^2 \lambda_p}{NA} \tag{3.21}$$,

where M_x^2 represents the slow-axis beam quality of the pump beam, λ_p is the pump wavelength, and NA is the numerical aperture of the waveguide.

For the K^+-Na^+ ion-exchanged waveguides fabricated within Schott BK7 glass in this chapter, the maximum index change is 8×10^{-3}, which gives an NA of ~0.16. Thus, a broad-stripe laser diode with a typical M_x^2 up to 40 would require a maximum taper width of ~200µm. An expansion coefficient of $\alpha = 2$ was explored in this work, producing a taper length of 11mm expanding from 2.5um to 175 um. The expansion was faster compared with the linear taper design in [1] to decrease the device length. The total lengths of all the tapered waveguides were kept constant at 46mm by changing the lengths of the single-mode channel sections. Following this design, a photolithographic mask was required first to create the formation of the waveguides. Here the mask structure parameters are listed in Table 3.1, and the waveguides fabricated from this mask are characterised in section 3.4.1.

Table 3.1 Design features of the photolithographic mask: linear and parabolic tapers.

Feature number	Feature type	Max. feature width (µm)	Taper length (mm)	Taper angle (^{o})	α value	Broad channel length (mm)
1	Linear	175	11.0	0.45	—	20
2	Parabolic	175	11.0	—	2	20
3	Channel	2.5	—	—	—	—
4	Linear	200	14.3	0.40	—	20
5	Parabolic	200	14.3	—	2	20
6	Channel	2.5	—	—	—	—
7	Linear	250	22.3	0.32	—	20
8	Parabolic	250	22.3	—	2	20
9	Channel	2.5	—	—	—	—
10	Linear	300	32.2	0.26	—	20
11	Parabolic	300	32.2	—	2	20

12	Channel	2.5	—	—	—	—
13	Linear	350	43.8	0.23	—	20
14	Parabolic	350	43.8	—	2	20

Using this mask, thermal ion exchange (TIE) can then applied to fabricate the waveguides, which will be discussed in section 3.3.

3.2.3 Modelling by the Beam Propagation Method

Complex waveguide structures such as tapers can be modelled with commercially available software (Prometheus software published by Kymata, Netherlands in this work) using 2D-BPM, to gain a qualitative insight into the operation of the tapered waveguide structure. Time consuming, full 3D-BPM would be required, together with an accurate knowledge of the true index profile, if we were to attempt to get quantitative modelling.

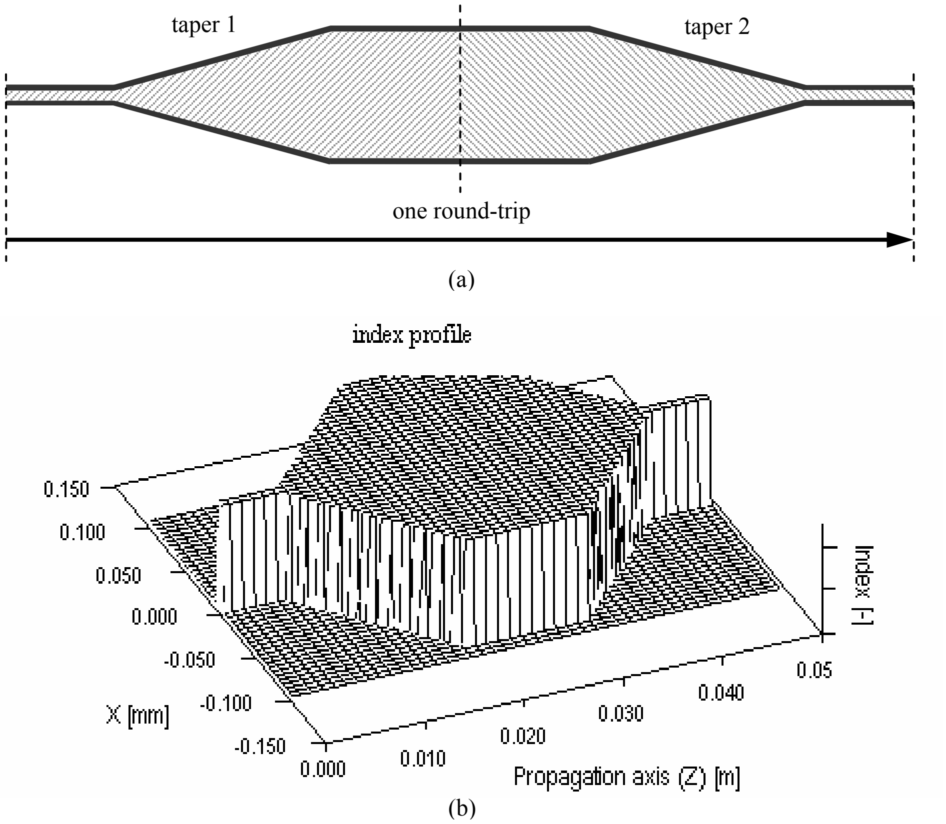

(a)

(b)

Figure 3.5 One round-trip of (a) the linear tapered waveguide structure and (b) the refractive-index profile applied in the BPM modelling.

The finite difference method (FD-BPM) was used in the modelling, owing to its accuracy for longitudinally varying waveguides with small index differences and its efficiency on the computation time compared to the fast Fourier transformation method (FFT-BPM) [14]. A linear taper of 11mm length expanding up to a width of 175μm ($\alpha = 2$) was tested, with parameters listed in Taper 1, Table 3.1, and a single round-trip was modelled within a laser cavity, as shown in Fig. 3.5 (a). The tapered waveguide represented here was fabricated by K^+-Na^+ TIE in BK7 glass, which produces the refractive-index profile shown in Fig. 3.5 (b), with the assumption of a constant core depth. It should be mentioned here that this model only analyses the effect on the waveguide mode due to propagation through the taper, and does not take into account any gain or loss through scattering or absorption.

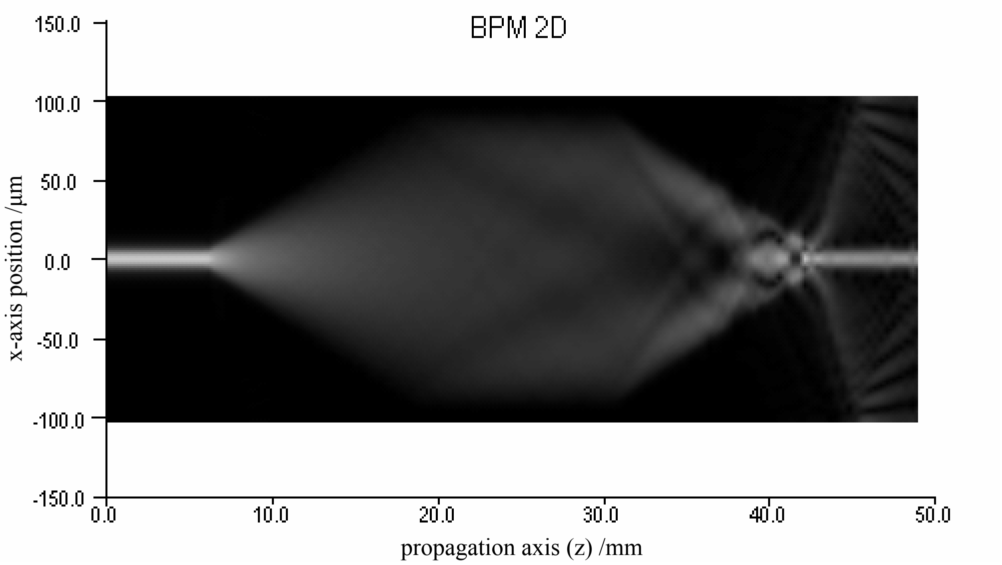

Figure 3.6 Evolution of the intensity in the one round-trip through the tapered waveguide, with higher intensities denoted by whiter colours.

Fig. 3.6 shows a diagrammatic field result of the intensity distribution for the fundamental mode making a round-trip through the tapered waveguide, with higher intensities denoted by whiter colours. As can be seen here, all power is confined within the single-mode channel section at first, with mode coupling occurring in the two taper sections during the propagation, and the higher-order modes are radiated from the waveguide as the second taper shrinks to the single-mode channel, which results in some reduction in the total guided power. However, although the 2D-BPM modelling allows effective assistance with the taper design, it provides only qualitative analysis concerning the taper performances, because the index profile used in this 2D-BPM modelling cannot actually represent the graded-index profile, which is the real case of the ion-exchanged waveguides. There is also known to be an increase in core depth for wider exchange apertures [15].

3.3 Fabrication

3.3.1 Thermal ion exchange

The waveguide fabrication adopts a standard TIE process, which is based on the exchange of ions from a glass with ions from molten salts. Ion exchange techniques had been used for more than a century to strengthen glass before it was used to produce a gradient refractive index in glass and consequently wave-guiding in 1972 [16]. Izawa and Nakagome reported the first ion-exchanged waveguides by exchange of Tl^+ ions in a silicate glass containing oxides of sodium and potassium. Since then, the technique has been applied in waveguide fabrication with various glasses, using different exchanging ions [17-19], and has been widely used due to its simplicity and flexibility in choosing the numerical aperture and dimensions.

Ion exchange is normally accomplished by the diffusion of monovalent ions of higher polarizability, such as Cs^+, K^+, Ag^+, Rb^+ and Tl^+ (diffusant ions), into the glass matrix where they usually exchange with Na^+ and K^+ ions (glass ions). Practically there are two main approaches to waveguide formation by ion exchange. One is assisted by the use of a molten salt bath, where the glass substrate is immersed in at an elevated temperature. An interphase concentration gradient is formed, as the concentration of the diffusant ions in the salt is much higher than within the glass, and thus the diffusant ions are driven into the glass from the salt. In order to maintain charge neutrality, the glass ions are released into the salt. Another approach requires a metallic film that is evaporated onto the surface of the glass substrate, and an external field is applied to incorporate the diffusant ions from the film into the glass structure, where they exchange with the glass ions. However, this approach has been limited to mainly the exchange of the Ag^+-Na^+ process [20] because of the stability problem of the metallic film.

The change in the refractive index of the substrate glass is due to both the different electrical polarizabilities and the different ionic radii of the exchanging ions, which can lead to mechanical strains [21]. Weiss and Srivastava [15] experimentally determined the two dimensional refractive index profile $n(x, y)$ of an ion-exchanged channel waveguide,

$$n(x, y) = n_3 + (\Delta n)\exp(-x^2/d_x^2)\,erfc(y/d_y) \qquad y \geq 0 \qquad (3.22),$$

where n_3 is the substrate index, Δn is the maximum index change measured at the surface and centre of the waveguide, and d_x and d_y describes the decay of the index profile in the lateral and depth directions, respectively. For this fabrication method, Δn is independent of the diffusion conditions and the photolithographic mask width, so d_x and d_y are the only two variables that can be adjusted through the fabrication procedure.

In order to maintain the shape and polish quality of the substrate glass, TIE is usually carried out below the substrate's glass transition temperature. Hence, nitrate salts are the practical choice for TIE due to their relatively low melting temperatures (200 - $400°C$) compared to sulphate salts (500 - $600°C$). In this thesis, the cheap and commercially available potassium nitrate ($K^+NO_3^-$ - melting temperature $333°C$) salt was chosen for the waveguide fabrication process as the diffusant ion K^+ can be easily incorporated into glass. Moreover, it is suitable to the fabrication of single-mode waveguides, due to a relatively low increase in refractive index ($\Delta n \leq 0.01$) [22]. It should be noted that K^+ has a low diffusion rate [23], which means that relatively long ion-exchange times are required for suitable wave-guiding to occur.

3.3.2 Fabrication process

The sample was fabricated in-house from commercially available BK7 glass chosen for its cheapness and good optical characteristics. The BK7 glass was doped with

1.5wt.% neodymium oxide (Nd_2O_3). The waveguide fabrication procedure is shown in Fig. 3.7.

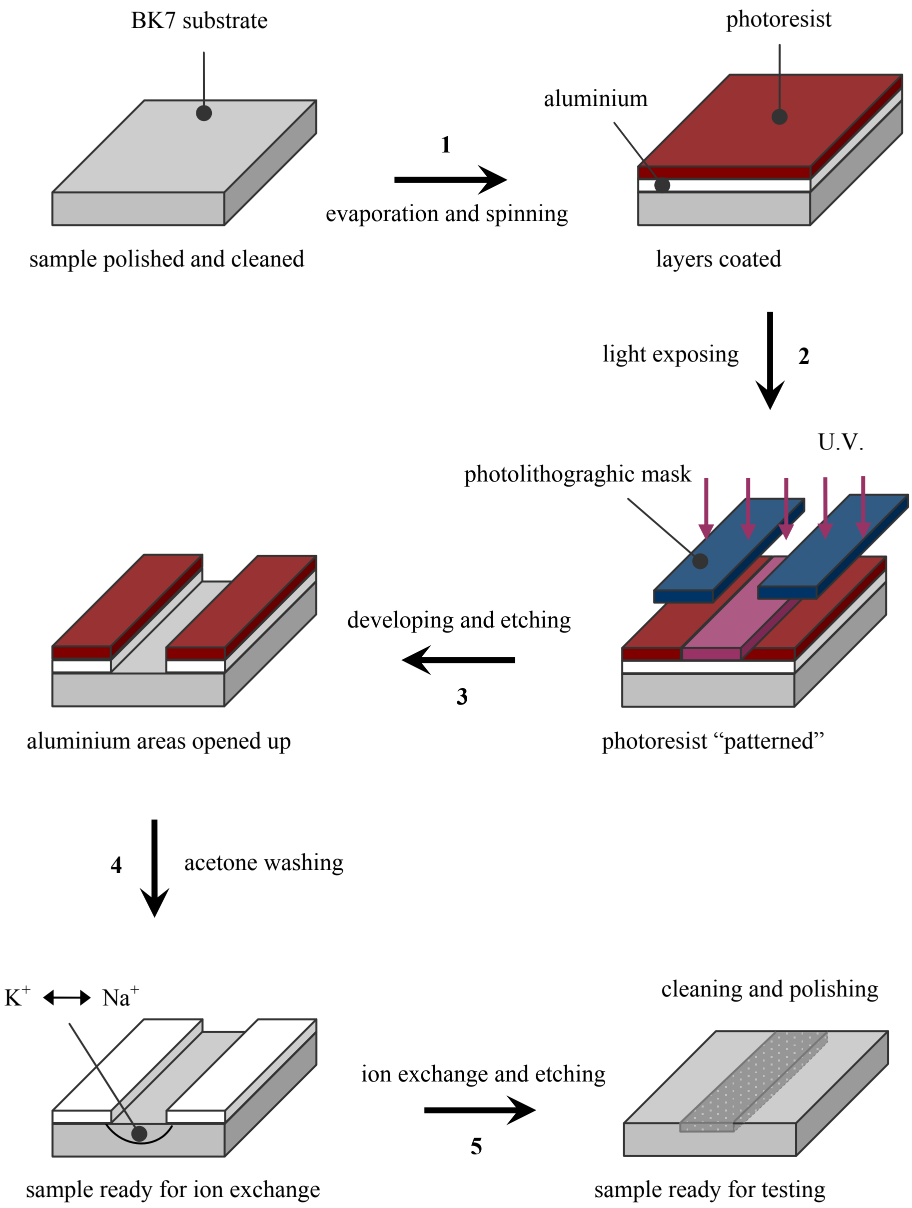

Figure 3.7 Fabrication procedure.

To prepare the sample for the fabrication, the glass block was cut to be 2mm thick, ~20mm wide and ~50mm long. The top surface was then polished to optical quality in preparation for the ion exchange process. One of the edges was also polished for the photolithography process carried out later on, to give an alignment reference to obtain parallelism of the waveguide structure with the substrate edge. This “reference” edge would also be used in the last step of the fabrication to help polish the two end faces to ensure their perpendicularity to the waveguide.

After polishing, the sample needed the necessary cleaning for the next step. Residual polishing wax was first removed by a 10-minute clean in trichloroethane at room temperature. Organic contaminants were then removed from the substrate by immersing it for 20 minutes in acetone heated to $50°C$ in an ultrasonic bath. Isopropanol was then immediately used to rinse the sample to remove the residual acetone, followed by a final rinse in deionised (DI) water. After a quick blowing dry, all traces of water needed to be removed off the substrate by storing the sample in an oven for 30 minutes at $120°C$. As far as inorganic contaminants are concerned, they were washed off with a 45-second fuming nitric acid bath, at room temperature. Again the sample was rinsed in water, blown dry and stored in a $120°C$ oven for 30 minutes. The cleaning procedure is shown schematically in Fig. 3.8. At this point the sample was clean of both organic and inorganic impurities.

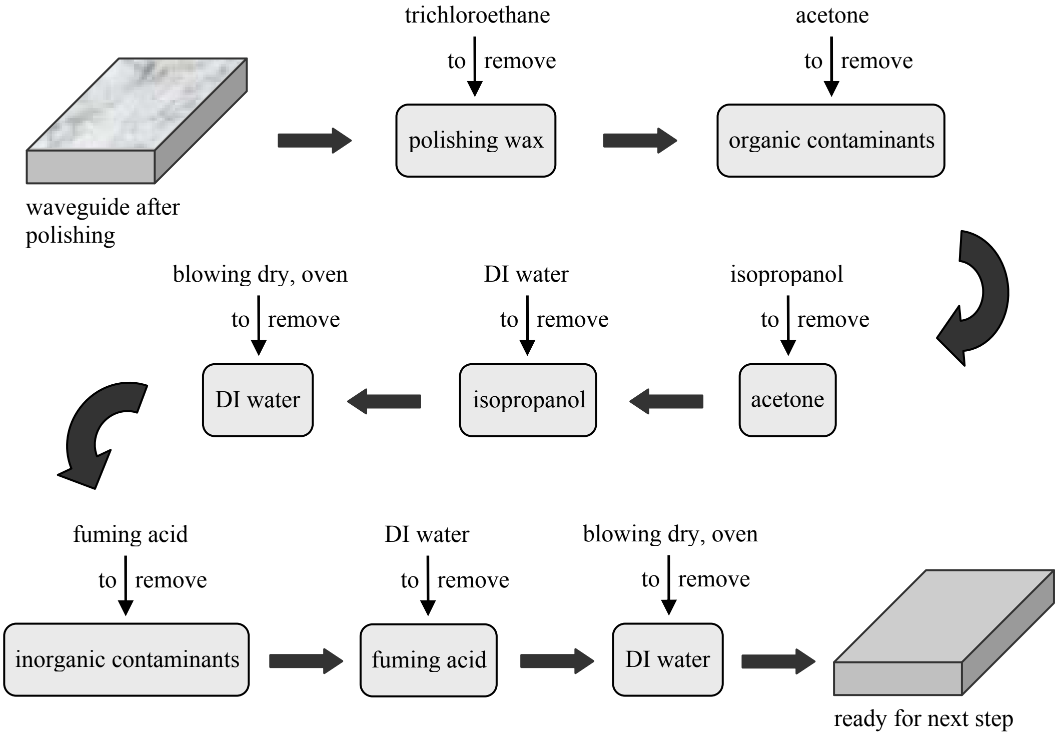

Figure 3.8 Cleaning procedure.

To produce any waveguide pattern (channels, tapers etc) by the ion exchange procedure, an “ion exchange mask” is required on the top of the substrate glass to effectively block the diffusant ions from reaching the surface of the glass, which should therefore carry the information of the photolithography mask itself. The material of the “mask” should not react with any of the chemicals during the fabrication process, especially at high temperatures, and should be able to be deposited on or removed off the top surface without difficulties. Aluminium is widely known to have lent itself well for this purpose. It can be evaporated rather easily, and was chosen in this work also for its relative cheapness. A 250nm-thick aluminium layer, expected to fully block the diffusant K^+ ions, was evaporated onto the polished sample surface, using an Edwards 309 thermal evaporator.

A standard photolithographic technique transfers the designed pattern onto the sample surface. First the aluminium layer was spin-coated with a 1μm layer of photoresist (S1813, 4000rpm for 60 seconds), which is a light sensitive polymer. After the spinning, the sample was then “soft baked” at $90°C$ for 30 minutes, to harden the photoresist.

The sample was exposed to ultraviolet (UV) light (with an exposure time of 11 seconds) through the openings of the photolithographic mask, thus passing the mask information onto the photoresist layer. The UV-exposed parts dissolved when developed in Shipley MF-319 developer for 50 seconds, which uncovered the aluminium layer underneath. After necessary DI water cleaning, the sample was then “hard baked” at $120°C$ for 30 minutes, which dried the sample and removed all solvents from the photoresist.

To copy the patterns present in the photoresist layer onto the aluminium layer, the sample was immersed in a 90-second aluminium etch at $60°C$, which opened the areas on the aluminium film that were exposed by the previous developing process. The residual photoresist was then removed by a 20-minute, $50°C$ acetone bath. The sample was rinsed by isopropanol and DI water afterwards, and was dried again in a $120°C$ oven, ready for ion exchange.

A salt crucible containing solid potassium nitrate was first heated to $395°C$ in an oven, with the salt fully molten, and then the sample, held in a stainless steel holder, was lowered into the salt and fixed there for an ion exchange time of 12 hours. The parameters for the ion-exchange procedure were chosen to give single mode channels at the laser wavelength [15]. The temperature of the salt was monitored with a thermocouple during the whole process.

After removal from the salt, the sample was cooled naturally in air and was washed in DI water to remove the remaining salt on it. The aluminium mask was stripped from the substrate using a 3-minute aluminium etch. The two end faces of the sample were polished parallel, perpendicular to the waveguides on the surface, and then the sample was ready for characterisation.

3.4 Laser characterisation

3.4.1 Comparison of linear and parabolic tapers

The laser performance of the waveguides (sample LP) fabricated with the parameters listed in Table 3.1 was assessed by pumping the single-mode channel ends of the waveguides with an argon-ion-pumped Ti:sapphire laser tuned to the Nd^{3+} peak absorption at 807nm. The pump beam was launched into the waveguides with a 10x microscope objective, which produced a spot size of $\approx 3\mu m$. The laser cavity set-up is shown schematically in Fig. 3.9. A monolithic laser cavity was formed by temporarily butting dielectric mirrors onto the end faces of the waveguide substrate, with the aid of the surface tension of a drop of fluorinated liquid for adhesion.

The input coupling mirror was highly reflecting at the lasing wavelength of 1.06μm and transmitted 95% of the pump power, while the output coupler had 23% transmission ($R_{oc} = 0.77$) at the lasing wavelength and was highly reflecting at the pump wavelength. Another 10x microscope objective was used to collimate the laser output beam to be characterised, followed immediately by a RG1000 filter (transmission of $< 10^{-5}$ at 807nm, and 68% at 1.06μm) to block residual pump light.

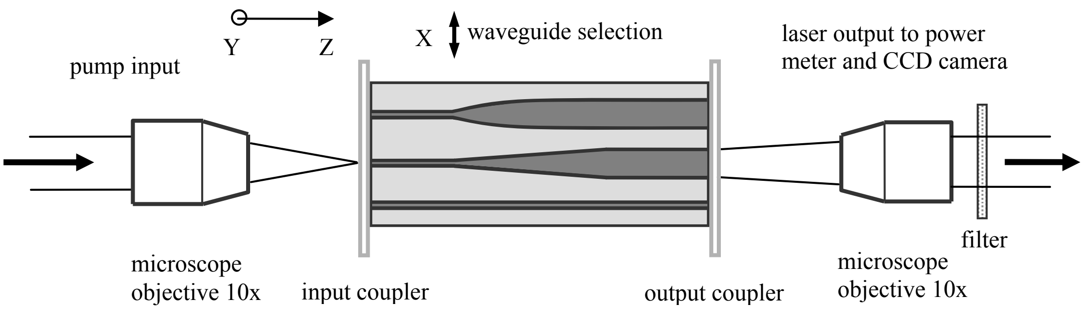

Figure 3.9 Top view of the experimental cavity set-up for the Ti:sapphire pumped channel and tapered waveguide lasers.

The collimated laser output was detected by a silicon photodiode connected to a digital oscilloscope that was triggered by a chopper placed in the way of the pump beam, so that the thresholds could then be judged by the appearance of sharp peaks in the fluorescence decay profile. According to the discussion in Chapter 2, the expression of laser threshold can be modified for a four-level laser as,

$$P_{th} = \frac{\pi h \nu_p \left[(\omega_{px}^2 + \omega_{lx}^2)(\omega_{py}^2 + \omega_{ly}^2) \right]^{\frac{1}{2}} (L - \ln R_{oc})}{4\sigma\tau\eta_a} \tag{3.23}$$

The optimum launch was found by both adjusting the position of the waveguide and tuning the Ti:sapphire laser (for the optimum pump wavelength/absorption) to find the lowest threshold power. However, the launch efficiency (the ratio of the power incident on the waveguide and the power immediately after) was measured when the Ti:sapphire laser was tuned off the Nd^{3+} absorption, without the coupling mirrors. The launch efficiency into a channel was calculated to be 64%, which was assumed to be the same for all the tapered waveguides, as they have the same size input ends.

The relationship between the incident power P_{in} and the absorbed power P_{abs} can be written as

$$P_{abs} = \eta_a \cdot \eta_L \cdot P_{in} \tag{3.24}$$

where η_a is the pump absorption efficiency as defined in Chapter 2 and η_L is the launch efficiency. With the launch efficiency available and absorption assumed to be

100% in such long waveguides, the results of the absorbed threshold power of the waveguides with different taper widths were obtained, as illustrated in Fig. 3.10. The best results of a 2.5μm-wide channel are also listed for comparison.

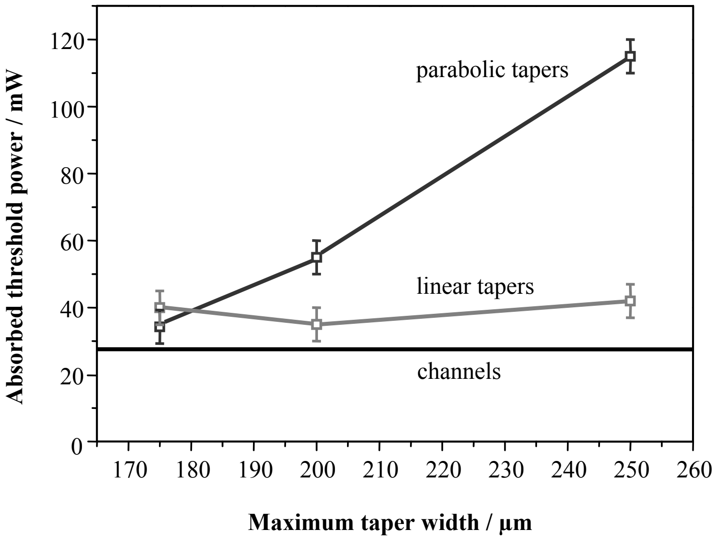

Figure 3.10 Absorbed pump power threshold against maximum taper width for the linear and parabolic tapered-waveguide lasers, alongside the standard channel waveguide lasers.

The slope efficiency was measured experimentally by recording laser output power at given pump powers for all these three types of waveguides. The calculation of the slope efficiency η_{slope} is based on the formula,

$$P_{out} = \eta_{slope}(P_{abs} - P_{th}) \quad (3.25).$$

Fig. 3.11 draws a comparison between the slope efficiencies of the linear and parabolic tapered waveguide lasers, alongside the standard channel waveguide lasers. It can be seen that, within experimental error, the 175μm-wide tapers for both taper structures have good laser performance, which is comparable to that of the channel guide. The small increase in threshold over that of the channel is reasonable if we consider the slight increase in propagation loss that is probably introduced by the taper expansion rate that was chosen here ($\alpha = 2$). However, while the linear tapers maintain the comparable laser performance, which shows independence of the taper width, the slope efficiency of the parabolic tapers encounters a sharp drop for larger widths, accompanied by a considerable increase in the laser threshold.

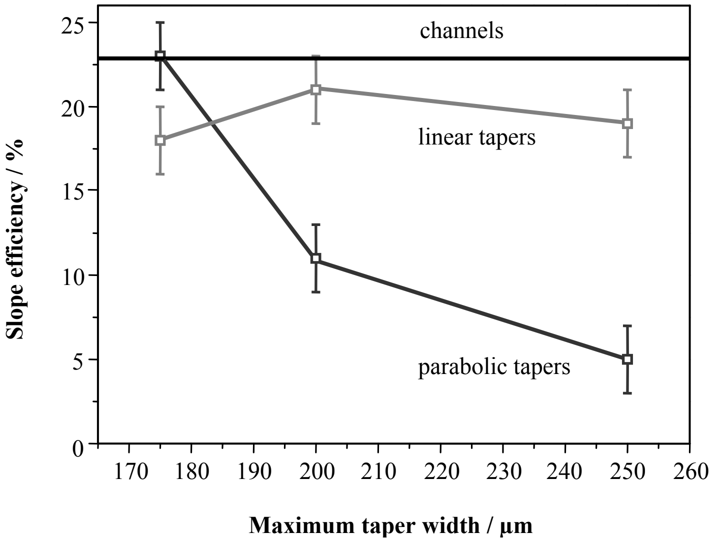

Figure 3.11 Slope efficiency against maximum taper width for the linear and parabolic tapered-waveguide lasers, alongside the standard channel waveguide lasers.

3.4.1.1 Discussion

Table 3.2 is given below as a summary of our experimental results, to compare the laser performance of the tapers and channels of different patterns.

Table 3.2 Summary of laser performance for the three types of waveguides.

Feature type	Max. feature width (µm)	Threshold power (mW)	Slope efficiency (%)
Linear taper	175	40	18
Linear taper	200	35	21
Linear taper	250	42	19
Parabolic taper	175	34	23
Parabolic taper	200	55	11
Parabolic taper	250	115	5
Channel	2.5	27	22

A rough estimate of the propagation loss can be calculated from the slope efficiency according to equation (2.14) in Chapter 2,

$$\eta_{slope} \leq \frac{\lambda_p}{\lambda_l}\left(\frac{-\ln R_{oc}}{-\ln R_{oc} + L}\right)\eta_{pl} \qquad (3.26).$$

λ_p and λ_l are the pump and the laser wavelengths, respectively. R_{oc} is the reflectivity of the output coupler, L is the round-trip loss in the cavity excluding the output coupling, and η_{pl} is a term that accounts for spatial overlap of the output and pump lasers, as defined in Chapter 2. The round-trip loss can be rewritten in dB as,

$$L_{dB} = -10\log_{10}(e^{-L}) = 2\delta \cdot l + \gamma \qquad (3.27),$$

where δ is the background propagation loss coefficient, l is the device length, and γ is here defined to characterise the additional round-trip loss as a result of the taper. Combining equations (3.26) and (3.27) and assuming $\eta_{pl} = 1$, a maximum possible background propagation loss coefficient of $\delta = 0.25\,\mathrm{dBcm}^{-1}$ is obtained when $\gamma = 0$ in the case of the standard channels, which is reasonable for TIE waveguides of this type. Thereby, the additional loss, γ, can be calculated, which is consistently ≤ 1.4dB for the linear tapers, whereas the additional loss rises up to over 10dB for the wider parabolic tapers. The low-loss nature of the linear tapers suggests an adiabatic quality that allows very little coupling from the fundamental mode to higher-order modes in the taper, which can be verified by a clean Gaussian output profile captured by a CCD camera shown in Fig. 3.12, compared with a distinct multimode output profile for the parabolic taper of the same width of 200μm.

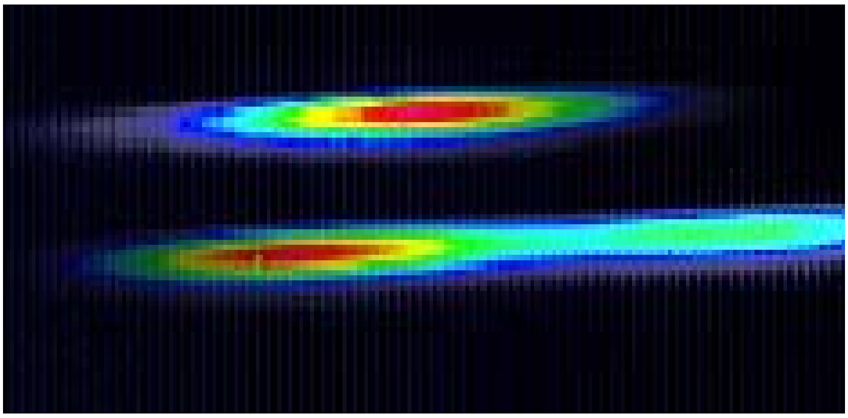

Figure 3.12 Imaged mode profiles for the 200μm-wide linear (upper) and parabolic (lower) tapers.

3.4.2 Broad-stripe diode pumping

As stated in the introduction, the objective of the work with the tapered waveguides is to produce 1-Watt level waveguide lasers with broad-stripe diode pumping. Some initial diode-pumping work was carried out, predominantly by two colleagues Dr S Hettrick and Dr C Li, and is included here for the completeness of this chapter. The laser diode used in this experiment was purchased from Polaroid Corporation (Model No. 462D-1375E-3-1), with the maximum output power of 2W and an emitter size of $1 \times 100\,\mu\text{m}$ (fast axis/slow axis), and after a collimation of the fast axis by a fibre lens the M^2 values were measured to be 1.9 and 22, respectively. One tapered-waveguide sample (sample LT), fabricated in the same type of substrate used for sample LP, was characterised using this laser diode, along with another broad-channel-waveguide sample (sample BC) fabricated in a separate substrate for comparison, both under identical fabrication conditions as used for sample LT. The structure details of these two samples are listed in Table 3.3.

Table 3.3 Design features of sample LT and sample BC.

Sample	Feature type	Max. feature width (μm)	Taper length (mm)	Taper angle (^{0})	Narrow channel length (mm)	Broad channel length (mm)
LT	Linear	175	12.5	0.40	6	25
BC	channel	175	—	—	—	18

The absorption coefficient measured in bulk 1.5wt.% Nd:BK7 was found to have a maximum value of 0.9 cm^{-1}, measured using a similar broad-stripe diode source. Double pass absorption is not applicable to the tapered waveguides since all power in modes higher than the fundamental will be radiated out of the waveguide along the taper. Taking these factors into consideration, the broad channel section of the taper was set to be 25mm, which gives a pump absorption efficiency of 89%, while it can be assumed that the 18mm-long broad channel from sample BC absorbs 100% pump radiation due to double-pass absorption.

The experimental set-up is similar to the one shown in Fig. 3.9. However, to launch the more non-diffraction-limited pump beam, the 10x microscope objective was replaced by a combination of two cylindrical focussing lenses with focal lengths $f = 19$ mm (slow axis) and $f = 12.7$ mm (fast axis) in order, which produces a spot size of 216×20 μm. Since the laser wavelength of the pump diode cannot be turned off the Nd^{3+} absorption in the same way as the Ti:sapphire laser, two 25mm-long undoped BK7 substrates were used to fabricate a planar waveguide and a 175μm-wide channel waveguide, with which launch efficiency can be measured, - 67% for the planar waveguide and 54% for the channel.

With a 23% transmission output coupler, the maximum output power obtained from this experiment was ~85mW, which appeared to be input-power-limited. The slope efficiencies were also obtained: 27.5% for the broad-channel waveguide and 12.9% for the tapered waveguide, with respect to absorbed power. The output from the broad channel was naturally multimode due to its own waveguide structure, while diffraction-limited output was extracted from the single-mode channel end of the tapered waveguide laser. Since the two waveguides were designed to obtain the same launch efficiency and their pump absorption are similar (100% and 89%), the superior slope efficiency of the broad channel waveguide laser possibly benefits from a better spatial overlap η_{pl} between the pump and the laser, according to equation (3.26). Unlike the case with Ti:sapphire pumping, where single-mode pump overlaps with single-mode laser, the overlap of the multimode diode pump and the fundamental-mode laser cannot be assumed to be 100% any more. As stated in section 3.4.11, the background propagation loss is assumed to be $0.25\,\text{dBcm}^{-1}$, which is a typical value for a TIE waveguide of this type, and the taper loss was obtained between $0 - 1.4$ dB for linear tapers, so that the spatial overlap factor η_{pl} can be calculated using equations (3.26) and (3.27). The results of this analysis are listed in Table 3.4.

Table 3.4 Slope efficiency results and spatial overlap calculation of sample LT and sample BC.

Sample	Feature type	Slope efficiency (%)	Background propagation loss (dBcm^{-1})	Additional taper loss (dB)	Spatial overlap η_{pl} (%)
LT	Linear	12.9	0.25	0 – 1.4	49 – 70
BC	channel	27.5	0.25	—	65

As can be seen, the overlap factor calculated for the channel is ~65%, which is reasonable for multimode pump and laser operation. However, the overlap for the diode-pumped linear taper could be as poor as 49% (as we expect that the additional taper loss is certainly less than the maximum possible figure of 1.4dB). This could be explained by the inherent property of graded-index waveguides described in section 2.5.3, that higher-order modes see a much larger effective core size and so can be considerably different in size to the fundamental mode. It is thus proposed that the linear taper is suffering from the poor overlap of the multimode diode pump and the single mode laser output. One possible future solution to this problem would be to use field-assisted ion-exchange as this allows some control over the index profile and is capable of producing more step-like index changes.

3.5 Summary

We have performed an experimental comparison of linear and parabolic tapers with fast expansion rates ($\alpha = 2$) to apertures of up to 250µm. The linear tapers investigated here show only a small additional loss over the background propagation loss of the ion-exchanged waveguides up to the maximum taper widths tried of 250µm, while parabolic tapers of the same length show a remarkable degradation in laser performance for the larger guiding sizes. The ability for the linear tapers to achieve adiabatic expansion to widths of 250µm suggests that linear tapers are compatible with high-average-power broad-stripe diode pumping, and should be of great interest as integrated-optics laser sources around 1 Watt level.

An initial demonstration of a broad-stripe diode-pumped tapered-waveguide laser with single-mode output has been reported at output power levels near 100mW, which showed no inclination of power drop even at the maximum pump power. Greater width of the linear tapers can improve the launch efficiency and the spatial overlap of the laser and pump can be increased by using step-index waveguides fabricated by FAIE. Moreover, higher power (~4W) diode stripes with similar output divergence can be purchased to deliver more pump power and allow the use of output couplers with higher transmission. It is estimated that output powers >0.5W can be achieved with these improvements accomplished.

3.6 References

[1] S. J. Hettrick, J. I. Mackenzie, R. D. Harris, J. S. Wilkinson, D. P. Shepherd, and A. C. Tropper, "Ion-exchanged tapered-waveguide laser in neodymium-doped BK7 glass," Optics Letters, vol. 25, pp. 1433-1435, Oct 1 2000.

[2] A. F. Milton and W. K. Burns, "Mode coupling in optical waveguide horns," IEEE Journal of Quantum Electronics, vol. QE-13, pp. 828-835, Oct 1977.

[3] I. Duport, P. Benech, D. Khalil, and R. Rimet, "Study of linear tapered waveguides made by ion exchange in glass," Journal of Physics D-Applied Physics, vol. 25, pp. 913-918, Jun 14 1992.

[4] D. P. Shepherd, S. J. Hettrick, C. Li, J. I. Mackenzie, R. J. Beach, S. C. Mitchell, and H. E. Meissner, "High-power planar dielectric waveguide lasers," Journal of Physics D-Applied Physics, vol. 34, pp. 2420-2432, Aug 21 2001.

[5] P. Madasamy, S. Honkanen, D. F. Geraghty, and N. Peyghambarian, "Single-mode tapered waveguide laser in Er-doped glass with multimode-diode pumping," Applied Physics Letters, vol. 82, pp. 1332-1334, Mar 3 2003.

[6] M. Mashayekhi, T. Touam, W. J. Wang, E. Berolo, and S. I. Najafi, "Semiconductor device to optical fiber coupling using low-loss glass taper waveguide," Optical Engineering, vol. 36, pp. 3476-3477, Dec 1997.

[7] K. Mizuuchi, K. Yamamoto, and T. Taniuchi, "High-efficiency coupling of laser-diodes in tapered proton-exchanged waveguides," Electronics Letters, vol. 26, pp. 1992-1994, Nov 22 1990.

[8] L. A. Zenteno, J. D. Minelly, A. Liu, A. J. G. Ellison, S. G. Crigler, D. T. Walton, D. V. Kuksenkov, and M. J. Dejneka, "1W single-transverse-mode Yb-doped double-clad fibre laser at 978 nm," Electronics Letters, vol. 37, pp. 819-820, Jun 21 2001.

[9] R. N. Thurston, E. Kapon, and A. Shahar, "2-dimensional control of mode size in optical channel waveguides by lateral channel tapering," Optics Letters, vol. 16, pp. 306-308, Mar 1 1991.

[10] D. J. Vezzetti and M. Munowitz, "Design of strip-loaded optical waveguides for low-loss coupling to optical fibers," Journal Of Lightwave Technology, vol. 10, pp. 581-586, May 1992.

[11] W. K. Burns, A. F. Milton, and A. B. Lee, "Optical waveguide parabolic coupling horns," Applied Physics Letters, vol. 30, pp. 28-30, Jan 1 1977.

[12] D. L. Lee, Electromagnetic principles of integrated optics - Chapter 5: John Wiley & Sons, 1986.

[13] D. P. Shepherd, C. L. Bonner, C. T. A. Brown, W. A. Clarkson, A. C. Tropper, D. C. Hanna, and H. E. Meissner, "High-numerical-aperture, contact-bonded, planar waveguides for diode-bar-pumped lasers," Optics Communications, vol. 160, pp. 47-50, Feb 1 1999.

[14] Y. Chung and N. Dagli, "An assessment of finite difference beam propagation method," IEEE Journal of Quantum Electronics, vol. 26, pp. 1335-1339, 1990.

[15] M. N. Weiss and R. Srivastava, "Determination of ion-exchanged channel waveguide profile parameters by mode-index measurements," Applied Optics, vol. 34, pp. 455-458, Jan 20 1995.

[16] T. Izawa and H. Nakagome, "Optical waveguide formed by electrically induced migration of ions in glass plates," Applied Physics Letters, vol. 21, pp. 584-586, Dec 15 1972.

[17] T. G. Giallorenzi, E. J. West, R. Kirk, R. Ginther, and R. A. Andrews, "Optical waveguides formed by the thermal migration of ions in glass," Applied Optics, vol. 12, pp. 1240-1245, 1973.

[18] G. Stewart, C. A. Millar, P. J. R. Laybourn, C. D. W. Wilkinson, and R. M. Delarue, "Planar optical waveguides formed by silver migration in glass," IEEE Journal of Quantum Electronics, vol. QE-13, pp. 192-200, Apr 1977.

[19] J. E. Gortych and D. G. Hall, "Fabrication of planar optical waveguides by K^+-ion exchange in BK7 and pyrex glass," IEEE Journal of Quantum Electronics, vol. 22, pp. 892-895, Jun 1986.

[20] G. H. Chartier, P. Jaussaud, A. D. Deoliveira, and O. Parriaux, "Optical waveguides fabricated by electric-field controlled ion-exchange in glass," Electronics Letters, vol. 14, pp. 132-134, 1978.

[21] A. Opilski, R. Rogozinski, M. Blahut, P. Karasinski, K. Gut, and Z. Opilski, "Technology of ion exchange in glass and its application in waveguide planar sensors," Optical Engineering, vol. 36, pp. 1625-1638, 1997.

[22] R. V. Ramaswamy and R. Srivastava, "Ion-exchanged glass waveguides: a review," Journal of Lightwave Technology, vol. 6, pp. 984-1002, Jun 1988.

[23] T. Findakly, "Glass waveguides by ion-exchange: A review," Optical Engineering, vol. 24, pp. 244-250, 1985.

Chapter 4

A diode-bar side-pumped waveguide laser with an extended cavity

4.1 Introduction

4.1.1 Diode pumping of planar waveguides

From this chapter on, diode lasers at higher power level are applied to the study of planar waveguide lasers. The asymmetric pump aperture of the waveguides can be matched to that of a diode bar with relative ease, which simplifies the coupling optics set-up. Moreover, producing thin regions of very high gain, the optical confinement offered by the planar waveguides leads to a high pumping intensity and low laser threshold, which can still be an issue in high-power laser systems, especially for quasi-three-level systems such as Yb.

High-power diode pumping generates heat load in the gain medium, which can cause various thermal problems which affect the laser beam quality and output power. As an extreme case of the slab geometry, the planar waveguide shows excellent thermal power handling capabilities. As discussed in Chapter 1, planar waveguides produce an approximately one-dimensional heat flow that passes through a relatively large cooling face, leading to a simple, efficient, and compact cooling scheme compared to bulk rod and fibre lasers. Furthermore, in the guided axis the optical guidance offered by the waveguide dominates the thermal lensing effect [1], and thermal depolarisation is also not a problem here due to the well-defined axes set by the slab structure. Therefore, the output laser beam quality in the guided axis can be well controlled by the waveguide structure itself.

Standard diode bars (30W per bar) were used in the experiments of this chapter for their relatively high power emission and reasonable spectral brightness, and the pumping configurations are investigated in the next section.

4.1.2 Diode coupling

The efficiency in the transfer of radiation from the pump source to the laser active medium determines, to a large extent, the overall efficiency of the waveguide laser system. A pump configuration is expected to provide good coupling between the source and the absorbing active material, and is also responsible for the pump density distribution in the laser region, which influences the spatial mode and optical distortions of the output beam.

The three possible pumping configurations (face-pumping, side-pumping and end-pumping, see Chapter 1) have all been investigated in planar waveguide lasers [2-4]. In-plane pumping, either longitudinal or transverse, allows much smaller waveguide cores (typically ~10μm) to be used [1], and can thus fully exploit the waveguide advantages of low lasing thresholds and excellent heat removal. End pumping has the advantage that good overlap is easily obtained between the pump distribution and the laser mode, leading to improved efficiency and mode control, but is limited in terms of power scalability. Alternatively, although less intense than end pumping, the side pumping configuration is more easily scaled, allows separate optimisation of the pumping, lasing and thermal management, and can still produce high inversion densities suitable for quasi-three-level transitions.

To design an appropriate waveguide structure and a proper pump cavity for diode pumping, it is necessary to first consider the diode-bar output, which is typically several thousand times diffraction-limited in the slow divergence axis (x-axis) and near diffraction-limited in the fast divergence axis (y-axis). Assuming that the waveguide is a symmetric step-index structure, the required beam quality of the pump radiation for good launch efficiency, perpendicular to the incident plane, will be related to the numerical aperture (NA) of the waveguide by:

$$M_y^2 \le \frac{NA \cdot t_w}{\lambda_p} \qquad (4.1),$$

where λ_p is the pump wavelength, t_w is the waveguide thickness, and NA is defined by,

$$NA = \sqrt{n_{core}^2 - n_{cladding}^2} \qquad (4.2),$$

where n_{core} and $n_{cladding}$ are the refractive index of waveguide core and the cladding layers, respectively. From (4.1) and (4.2), it can be seen that greater index contrast between n_{core} and $n_{cladding}$ will give the waveguide higher numerical aperture, which can tolerate "poorer" beam quality (with higher M^2 value) from the pump beam. However, it should also be noted that there is no point in going to extreme NA values if one is still limited by the numerical aperture of the coupling optics.

Therefore, it is logical that, for high power diode pumping with diode bars and stacks, co-joining materials with dissimilar refractive index is preferred compared to modification of refractive index in one material, as it is easier to fabricate high NA waveguides in this way. According to equation (4.2), a YAG/sapphire guide structure has an $NA = 0.46$. By substituting a typical waveguide thickness $t_w = 30\mu m$ into equation (4.1), at a pump wavelength $\lambda_p \approx 0.8\mu m$, the beam quality of the laser diode is limited by $M_y^2 < 17.5$, while the measured M_y^2 value of a standard diode bar is often ~ 5 or more after collimation in the fast axis. As stated in Chapter 1, the technique of direct bonding [5, 6] produces such waveguides with good thermal management characteristics that cope well with high power operation, and is used in the fabrication of the waveguide tested in this chapter.

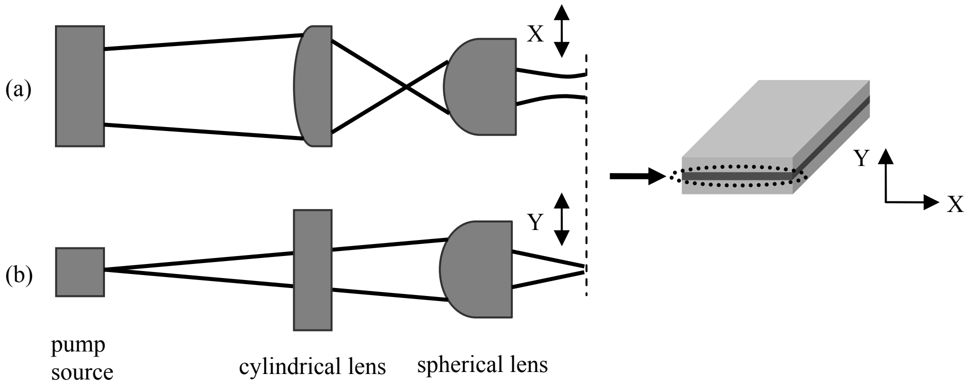

Figure 4.1 Typical pump configuration of a diode end-pumped waveguide laser: (a) coupling scheme for the diode "slow" axis, and (b) for the "fast" axis.

The end-pumped configurations often use a shaped high-brightness diode pump source that has a beam quality, at least in one axis, qualified for the condition set by the equation (4.1). The pump beam is usually launched into the waveguide with a simple cylindrical-and-spherical lens combination. A cylindrical lens can be used to focus the x-axis (diode slow axis) beam followed by a spherical short focal length lens to focus inside the waveguide in this axis [7]. This spherical lens is positioned at the right place so that the focussed pump beam in the other axis (diode fast axis) reaches the beam waist at the entrance aperture of the waveguide, as shown in Fig. 4.1.

In the case of side pumping, high-power pump sources such as diode bars are well suited to the pumping configuration, closely matching the geometry of the planar waveguide. If we wish to couple the pump radiation from a diode bar into a planar waveguide using simple cylindrical lenses, rather than trying to circularise the beam (and equalize the $M_{x,y}^2$ values), then it is easier to try to guide the lower M_y^2 value of the fast axis. Furthermore, this cylindrical lens coupling technique is also compatible with diode-stack pumping, which gives another option for power scaling side-pumped waveguide lasers. The experiment in this chapter was set up by side pumping and the coupling scheme will be shown in section 4.3.

Based on the technique of direct bonding, proximity coupling has been developed in the scientific literature [8-10]. The availability of high *NA* guides allows the possibility of simply proximity coupling the beam from diode bars to planar waveguides, which avoids the need for any coupling optics and leads to a very simple and compact design. For instance, the 0.46 *NA* of a YAG/sapphire guide allows incident light travelling at angles of up to 28° to be coupled, as shown in Fig. 4.2. This is compatible with the non-collimated outputs of many diode bars, which typically have a half-width half-maximun beam divergence of $< 20^\circ$ in the fast axis. Experimentally [8], a proximity-coupling launch efficiency of nearly 90% has been demonstrated with a waveguide that consists of an 8-μm-thick Nd:YAG core contact-bonded to a sapphire substrate.

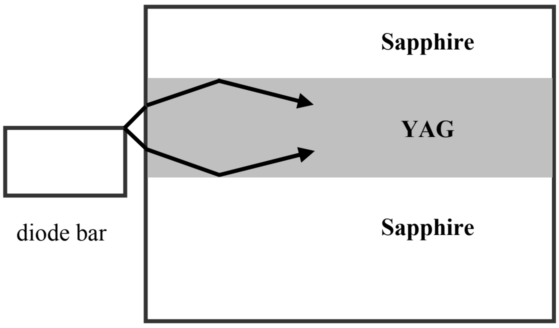

Figure 4.2 Schematic representation of diode to waveguide proximity coupling.

4.1.3 Spatial mode control

High *NA* waveguides with depths of several tens of microns would normally suffer from a lasing output that is non-diffraction-limited due to the multimode nature of the structure. In order to gain spatial mode control in the guided axis, a double-clad, multilayer, planar waveguide structure was presented by the same authors in [8], as shown in Fig. 4.3. Similar to a double clad fibre, this structure has a low numerical aperture (*NA*) inner structure, and a high *NA* outer structure.

Nevertheless, there is a significant difference between the double-clad planar waveguides considered here and classical double-clad fibres (see Fig. 4.4).

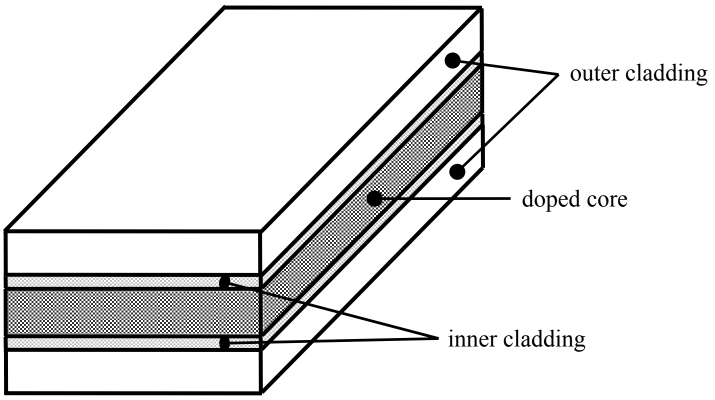

Figure 4.3 Schematic of double-clad planar waveguide structure.

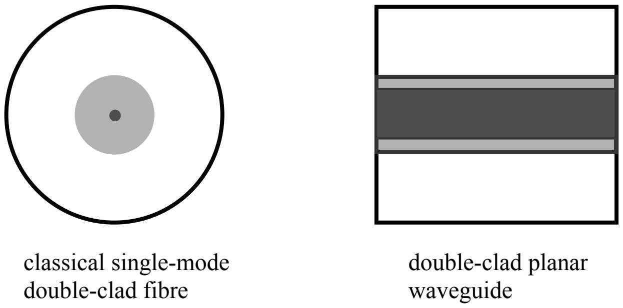

Figure 4.4 Cross-section comparison of a "classical" single-mode double-clad fiber and a large-mode-area double-clad planar waveguide.

For a double-clad fibre laser [11], the doped core is itself a single-mode waveguide surrounded by a considerably larger multimode inner cladding, which is in turn surrounded by an outer cladding of a much lower refractive index. The diode pump beam is captured by the inner cladding first and gradually absorbed when it passes through the doped core, and thus single-spatial-mode laser output is naturally obtained by index guiding. Note that a long fibre is required to achieve enough pump absorption due to the fact that the pump mode volume is significantly larger than the doped region. Producing long lengths of fibre is relatively easy and low overall propagation losses are still obtained.

On the other hand, practically the absorption length of the planar waveguide cannot exceed feasible fabrication limitations of typically less than a few centimetres. This requires a much larger doped core compared with the inner cladding to ensure efficient absorption and under these conditions the core is no longer an isolated single-mode waveguide. Thus in the planar waveguide structure, single-mode operation is maintained by gain mode selection rather than index guiding, as discussed in the following section.

The use of a double-clad structure can improve the beam quality in the guided-axis for a diode-pumped waveguide laser. However, for power-scalable side-pumping arrangements, the laser output remains highly multimode in the non-guided plane. Unstable resonators are often a solution, to attain a large fundamental mode volume and good spatial mode selection. Nevertheless, the unstable resonator can be more sensitive to the misalignment in comparison to its stable counterpart and the advantage of a large mode volume is often achieved with a reduction of the mode quality [12].

Another approach is to expand the fundamental cavity mode using a telescopic resonator [13]. A variation of this technique, using an extended cavity consisting of two cylindrical lenses and a plane mirror, is expected to deliver high-brightness output from the non-guided axis. Stable extended-cavity configurations have previously been applied to direct-bonded multimode channel waveguide lasers at relatively low power [14-16]. In this chapter, an extended stable cavity combined with the double-clad waveguide is investigated, to achieve the output spatial mode control in both guided and non-guided axes.

4.2 Mode-selection in double-clad waveguides

4.2.1 Modelling of the propagation modes

Following the same methods and principles as in Chapter 2, it is necessary to discuss the guided mode solutions for the double-clad planar waveguide structures that are used in the devices reported in this and the next chapter. Mode solutions for the TE field are derived, from which, by the duality of Maxwell's equations, the corresponding TM mode solutions can be easily obtained.

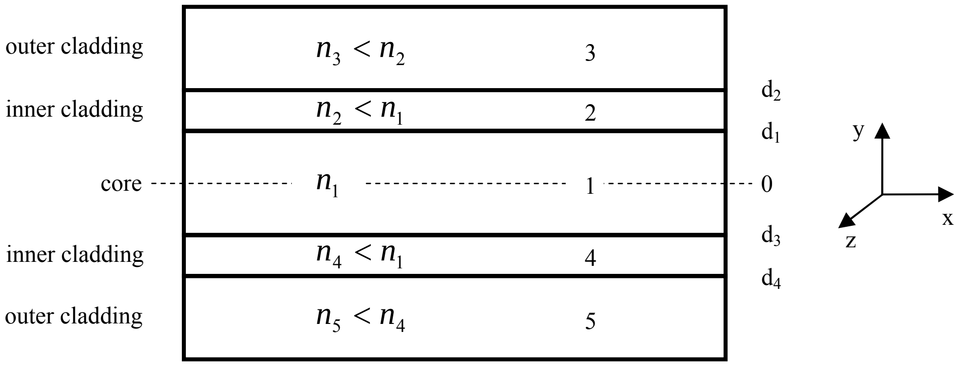

Figure 4.5 Schematic structure of a double-clad planar waveguide.

As shown in Fig. 4.5, the double-clad planar waveguide has a core layer surrounded by two lower refractive index materials. In our experiments, the structure is symmetric with $d_{1,2} = d_{3,4}$ and $n_{2,3} = n_{4,5}$, which is not necessary in the model investigated here. Solutions for E_x, in the separate waveguide regions, will be derived. Again, it is assumed that, in the core region, the guided waves produce a transverse standing wave pattern described by an oscillatory solution; whereas a general expression form is given for the inner cladding, depending on the wave guiding situation inside the region, either expressed by exponential decay or by an oscillatory solution, which is in contrast to the modelling in section 2.5.2; and finally, the solutions decay exponentially beyond the inner cladding region. Therefore, the tangential component of the E-field E_x can be written as,

$$E_x(y,z) = \begin{Bmatrix} A_3 e^{-\alpha_{3y} y} \\ A_2 e^{-\alpha_{2y} y} + A_2' e^{\alpha_{2y} y} \\ A_1 \cos(k_{1y} y + \psi) \\ A_4 e^{\alpha_{4y} y} + A_4' e^{-\alpha_{4y} y} \\ A_5 e^{\alpha_{5y} y} \end{Bmatrix} e^{-ik_z z} \qquad \begin{matrix} y \geq d_2 \\ d_1 \leq y \leq d_2 \\ y \leq |d_1| \\ d_4 \leq y \leq d_3 \\ y \leq d_4 \end{matrix} \qquad (4.3).$$

The parameters above follow the same definition principle as stated in Chapter 2: A_i is the field amplitude in the i$^{\text{th}}$ layer, ψ denotes the offset of the peak intensity from the centre of the core for region 1, due to the possibility of the non-symmetric nature, and α_{iy}, k_{1y} are the y-axis wave vectors in the i^th^ layer and the core respectively, which are expressed by

$$\alpha_{iy} = \sqrt{k_z^2 - \mu_i \varepsilon_i \omega^2} = k_0 \sqrt{n_{eff}^2 - n_i^2} \tag{4.4}$$

$$k_{1y} = \sqrt{\mu_1 \varepsilon_1 \omega^2 - k_z^2} = k_0 \sqrt{n_1^2 - n_{eff}^2} \tag{4.5}$$

where $n_{eff} = k_z / k_0$ is the effective refractive index experienced by the guided mode, and k_0 is the wave vector in free space.

According to (2.60), the tangential magnetic field is given by,

$$H_z(y,z) = \left\{ \begin{array}{ll} \dfrac{-i\alpha_{3y}}{\omega\mu_3} A_3 e^{-\alpha_{3y} y} & y \geq d_2 \\ \dfrac{-i\alpha_{2y}}{\omega\mu_2} (A_2 e^{-\alpha_{2y} y} - A_2' e^{\alpha_{2y} y}) & d_1 \leq y \leq d_2 \\ \dfrac{-ik_{1y}}{\omega\mu_1} A_1 \sin(k_{1y} y + \psi) & y \leq \left| d_1 \right| \\ \dfrac{i\alpha_{4y}}{\omega\mu_4} (A_4 e^{\alpha_{4y} y} - A_2' e^{-\alpha_{4y} y}) & d_4 \leq y \leq d_3 \\ \dfrac{i\alpha_{5y}}{\omega\mu_5} A_5 e^{\alpha_{5y} y} & y \leq d_4 \end{array} \right\} e^{-ik_z z} \tag{4.6}$$

The tangential components of E and H must be continuous at the interfaces, which produces eight equations at $y = d_2, d_1, d_3, d_4$:

$$y = d_2: \quad \begin{array}{l} A_3 e^{-\alpha_{3y} d_2} = A_2 e^{-\alpha_{2y} d_2} + A_2' e^{\alpha_{2y} d_2} \\ \dfrac{-i\alpha_{3y}}{\omega\mu_3} A_3 e^{-\alpha_{3y} d_2} = \dfrac{-i\alpha_{2y}}{\omega\mu_2} (A_2 e^{-\alpha_{2y} d_2} - A_2' e^{\alpha_{2y} d_2}) \end{array} \tag{4.7, 8}$$

$$y = d_1: \quad \begin{array}{l} A_2 e^{-\alpha_{2y} d_1} + A_2' e^{\alpha_{2y} d_1} = A_1 \cos(k_{1y} d_1 + \psi) \\ \dfrac{-i\alpha_{2y}}{\omega\mu_2} (A_2 e^{-\alpha_{2y} d_1} - A_2' e^{\alpha_{2y} d_1}) = \dfrac{-ik_{1y}}{\omega\mu_1} A_1 \sin(k_{1y} d_1 + \psi) \end{array} \tag{4.9, 10}$$

$$y = d_3: \qquad \begin{aligned} &A_1 \cos(k_{1y} d_3 + \psi) = A_4 e^{\alpha_{4y} d_3} + A_4' e^{-\alpha_{4y} d_3} \\ &\frac{-ik_{1y}}{\omega\mu_1} A_1 \sin(k_{1y} d_3 + \psi) = \frac{i\alpha_{4y}}{\omega\mu_4} (A_4 e^{\alpha_{4y} d_3} - A_4' e^{-\alpha_{4y} d_3}) \end{aligned} \qquad (4.11,\ 12)$$

$$y = d_4: \qquad \begin{aligned} &A_4 e^{\alpha_{4y} d_4} + A_4' e^{-\alpha_{4y} d_4} = A_5 e^{\alpha_{5y} d_4} \\ &\frac{i\alpha_{4y}}{\omega\mu_4} (A_4 e^{\alpha_{4y} d_4} - A_4' e^{-\alpha_{4y} d_4}) = \frac{i\alpha_{5y}}{\omega\mu_5} A_5 e^{\alpha_{5y} d_4} \end{aligned} \qquad (4.13,\ 14).$$

The amplitude coefficient A_i, $i = 2,3,4,5$, can be expressed in terms of A_1, and all of A s can be eliminated by dividing the 4 sets of boundary condition equations above. A phase delay is obtained that corresponds to the plane wave propagation through the upper and lower halves of the waveguide. After the derivation, similar to the asymmetric model discussed in Chapter 2, the TE mode guidance condition for the double-clad waveguide can be written as

$$2k_{1y} d_1 - \varphi_U - \varphi_L = n\pi \qquad n = 0,1,... \qquad (4.15),$$

where ϕ_U and ϕ_L are the phase delays for plane waves propagating through the upper and lower half of the waveguide:

$$\phi_U = \tan^{-1}\left(\frac{\mu_1 \alpha_{2y}}{\mu_2 k_{1y}} \left(\frac{\mu_2 \alpha_{3y} + \mu_3 \alpha_{2y} \tanh(\alpha_{2y}(d_2 - d_1))}{\mu_3 \alpha_{2y} + \mu_2 \alpha_{3y} \tanh(\alpha_{2y}(d_2 - d_1))} \right) \right) \qquad (4.16)$$

$$\phi_L = \tan^{-1}\left(\frac{\mu_1 \alpha_{4y}}{\mu_4 k_{1y}} \left(\frac{\mu_4 \alpha_{5y} + \mu_5 \alpha_{4y} \tanh(\alpha_{4y}(d_3 - d_4))}{\mu_5 \alpha_{4y} + \mu_4 \alpha_{5y} \tanh(\alpha_{4y}(d_3 - d_4))} \right) \right) \qquad (4.17).$$

Once the amplitude coefficients are written in terms of A_1 and the guidance condition is solved for a particular mode, the corresponding fields in all the five regions can then be obtained:

$$E_x(y,z) = A_1 \left\{ \begin{matrix} A_U e^{(\alpha_{2y}+\alpha_{3y})d_2}\left(\dfrac{2\mu_3\alpha_{2y}}{\mu_3\alpha_{2y}-\mu_2\alpha_{3y}}\right)e^{-\alpha_{3y}y} \\ A_U\left[\left(\dfrac{\mu_3\alpha_{2y}+\mu_2\alpha_{3y}}{\mu_3\alpha_{2y}-\mu_2\alpha_{3y}}\right)e^{\alpha_{2y}(2d_2-y)}+e^{\alpha_{2y}y}\right] \\ \cos(k_{1y}y+\psi) \\ A_L\left[\left(\dfrac{\mu_5\alpha_{4y}+\mu_4\alpha_{5y}}{\mu_5\alpha_{4y}-\mu_4\alpha_{5y}}\right)e^{\alpha_{4y}(-2d_4+y)}+e^{-\alpha_{4y}y}\right] \\ A_L e^{-(\alpha_{4y}+\alpha_{5y})d_4}\left(\dfrac{2\mu_5\alpha_{4y}}{\mu_5\alpha_{4y}-\mu_4\alpha_{5y}}\right)e^{\alpha_{5y}y} \end{matrix} \right\} e^{-ik_z z} \qquad \begin{matrix} y \ge d_2 \\ d_1 \le y \le d_2 \\ y \le |d_1| \\ d_4 \le y \le d_3 \\ y \le d_4 \end{matrix} \qquad (4.18)$$

where A_U and A_L are derived as:

$$A_U = \frac{\cos(k_{1y}d_1+\psi)e^{-\alpha_{2y}d_1}}{\left(\dfrac{\mu_3\alpha_{2y}+\mu_2\alpha_{3y}}{\mu_3\alpha_{2y}-\mu_2\alpha_{3y}}\right)e^{2\alpha_{2y}(d_2-d_1)}+1} \qquad (4.19)$$

$$A_L = \frac{\cos(k_{1y}d_3+\psi)e^{\alpha_{4y}d_3}}{\left(\dfrac{\mu_5\alpha_{4y}+\mu_4\alpha_{5y}}{\mu_5\alpha_{4y}-\mu_4\alpha_{5y}}\right)e^{2\alpha_{4y}(d_3-d_4)}+1} \qquad (4.20).$$

4.2.2 Gain mode selection

As stated in Chapter 2, for a uniformly side-pumped waveguide laser, the spatial rate equation analysis can be modified by relating the spatial pump variation to the doping concentration, and thereby the gain for each guided mode can be obtained for a given doping profile, lasing mode spatial distribution and the laser power.

Equation (2.9) is rewritten here in the form of G_{rel}, which is the relative gain for the pth mode,

$$G_{rel} = \frac{G_p}{L+T_{oc}} = \iiint \frac{d(x,y,z)\phi_p(x,y,z)}{\left[1+\dfrac{c\sigma\tau f}{n}\Phi\phi_0(x,y,z)\right]\left[\displaystyle\iiint \frac{d(x,y,z)\phi_0(x,y,z)}{1+\dfrac{c\sigma\tau f}{n}\Phi\phi_0(x,y,z)}dV\right]}dV \qquad (4.21).$$

Figure 4.6 One-dimensional step-function doping of a double-clad planar waveguide, with the doping ratio t_{core}/t_w.

With the one-dimensional step-function doping profile of the double-clad planar waveguides investigated in this chapter, as shown in Fig. 4.6, the normalised doping distribution $d(x,y,z)$ is then described by

$$d(x,y,z) = \frac{1}{w_c l t_{core}} \qquad |y| \le \frac{t_{core}}{2} \tag{4.22}$$

where w_c and l are the width and length of the waveguide crystal and t_{core} is the waveguide core thickness. The relative gain for each of the waveguide modes can be solved, by applying the normalized spatial distribution of photons $\phi_p(x,y,z)$ given by [17]:

$$\phi_{even}(x,y,z) = \frac{2}{w_c l t_w} \cos^2\left[\frac{(m+1)\pi y}{t_w}\right] \tag{4.23}$$

$$\phi_{odd}(x,y,z) = \frac{2}{w_c l t_w} \sin^2\left[\frac{(m+1)\pi y}{t_w}\right] \tag{4.24}$$

where m is the mode number ($m = 0,2,4\ldots$ for the even modes and $m = 1,3,5\ldots$ for the odd modes) and t_w is the waveguide thickness.

The relative gain G_{rel} of each mode could then be calculated using equations (4.21) to (4.24). It is understandable that the fundamental mode will always lase first at threshold level, due to the clear gain advantage. However, it is shown by the modelling that, as expected, heavy saturation can lead to the gain for the high-order modes becoming larger than that for the fundamental mode. Nevertheless, the calculation results show that, with a doping ratio t_{core}/t_w below 0.6, the fundamental mode always has the gain advantage over higher-order modes even for a highly saturated situation, as shown in Fig. 4.7 with the first 4 modes.

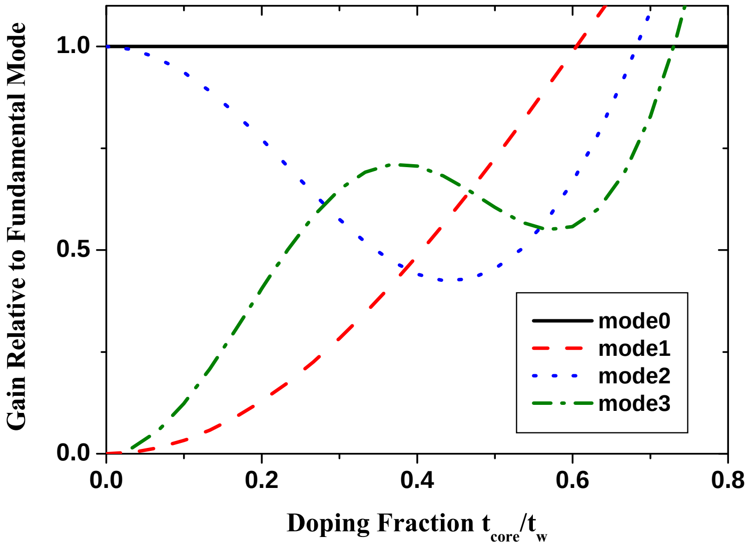

Figure 4.7 Relative gain for the first four guided modes at 1064nm against doping fraction for a resonating one-directional power 100 times greater than the saturation power.

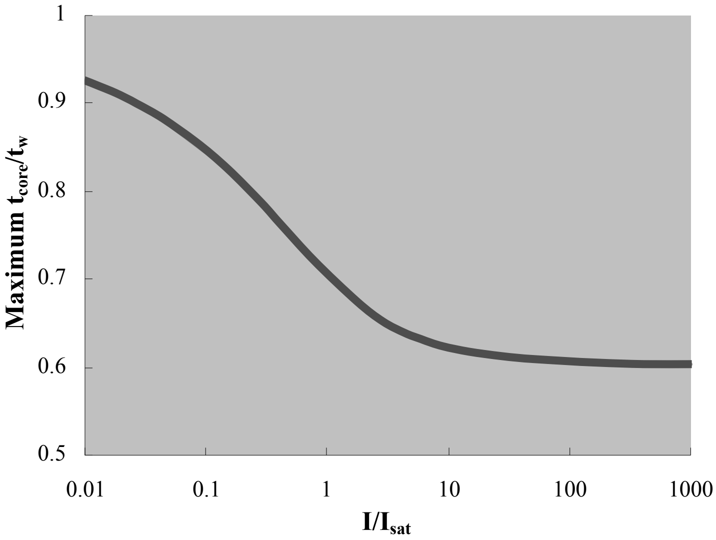

Figure 4.8 Doping fraction at which the gain for mode 1 becomes equal to that for mode 0, relative to value of I/I_{sat}.

Another calculation result is shown in Fig. 4.8, which plots the doping fraction at which high-order-mode oscillation occurs against the intracavity lasing intensity up to 1000 times the saturation intensity ($I/I_{sat} = 1000$). Again it proves that $t_{core}/t_w = 0.6$ is the critical point, below which the gain for $m = 1$ mode is always kept less than that for the $m = 0$ mode and then the fundamental–mode operation is strictly selected.

4.3 Laser operation

4.3.1 Extended cavity design

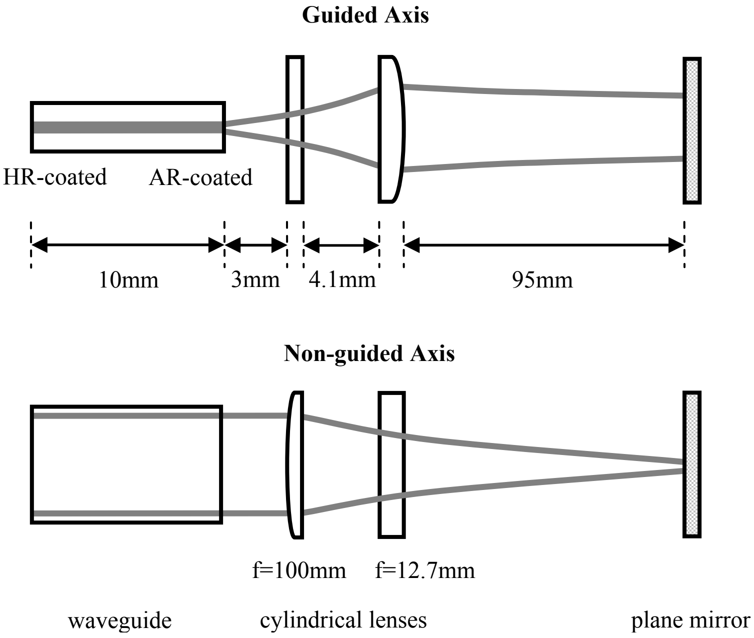

Figure 4.9 Extended stable cavity resonator design.

In this section, an extended stable cavity is described to produce a near diffraction-limited output mode and investigate its efficiency. The cavity design is based on the concept that the two orthogonal axes of the waveguide can be treated independently. Using an ABCD matrix model, a ~125mm long cavity was modelled, with the real lens thicknesses and curvatures taken into account. The schematic is illustrated in Fig. 4.9.

The two ends of the waveguide are coated by high-reflection and anti-reflection thin films, respectively. In the guided axis, due to its small mode size (~10μm), the beam exiting the waveguide is significantly divergent. A 12.7mm focal length cylindrical lens acts to roughly collimate the beam. The combination of waveguide and single positive lens can be regarded as a cylindrical beam expanding telescope [13]. The position of this y-axis cylindrical lens is determined by the condition that after a round trip through the cavity, from the waveguide output face to the output coupler (OC) mirror and back again, the beam radius must match that of the fundamental mode of the waveguide, which is preferentially selected by the double-clad geometry, as discussed in the previous section.

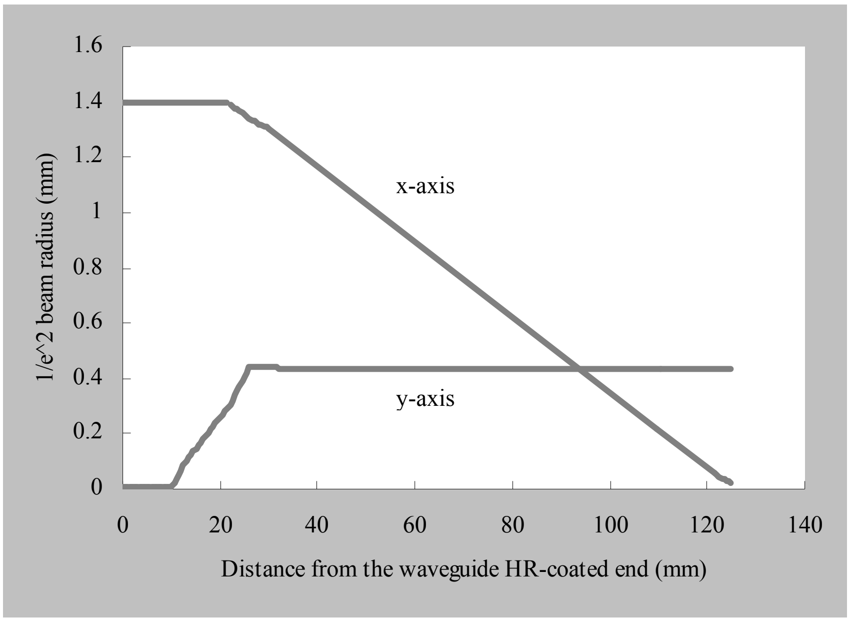

Figure 4.10 A computer modelling on the real lens extended cavity with two cylindrical lenses, showing beam radii for the two axes with the change of the cavity length.

In the non-guided axis, a 100mm focal length cylindrical lens forms a tightly focussed beam-waist at the external plane mirror and can be tailored such that a large cavity mode fills the 5mm-wide gain region by extending the cavity length (~120mm) near to the stability limit. Thus the beam waists in both axes are formed at the plane external mirror. The outside end-face of the waveguide was directly coated to complete the laser resonator. Fig. 4.10 shows the theoretical modelling on the beam radii in the two axes against the distance from the waveguide HR-coated face to the output coupler mirror.

4.3.2 Experimental set-up

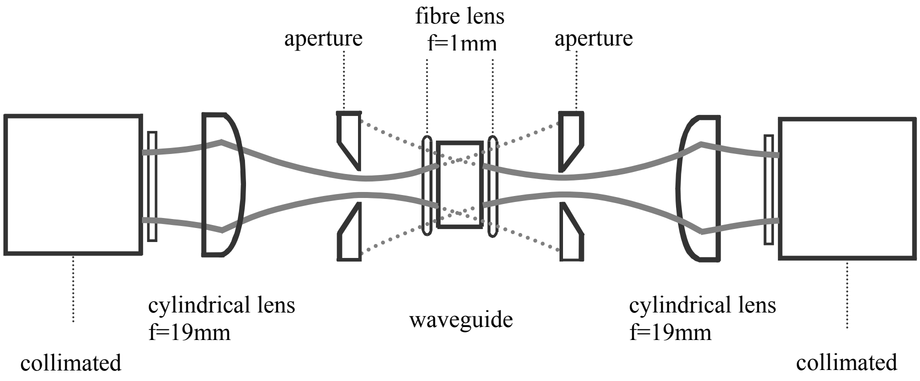

(a) Top view of the coupling optics arrangements.

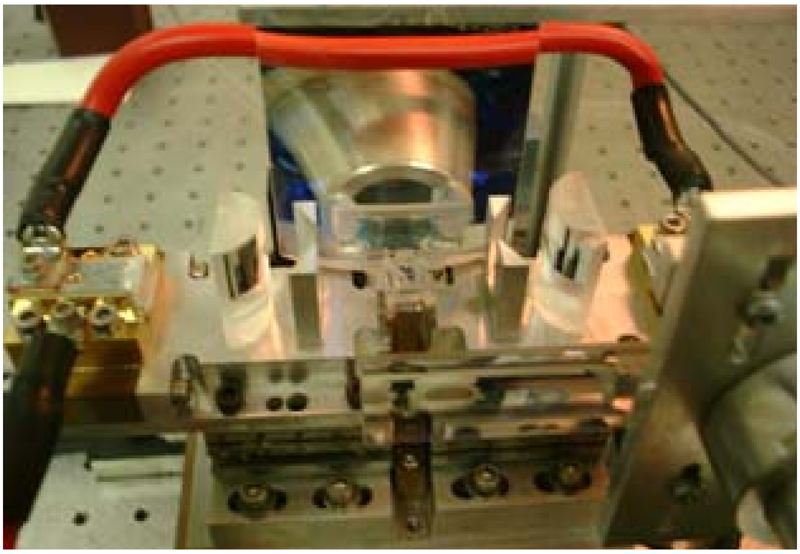

(b) Photo of optical coupling scheme.

Figure 4.11 Pump set-up of a diode-bar side-pumped Nd:YAG double-clad planar waveguide laser.

The waveguide used in these experiments is 5mm wide by 10mm long and consists of a 30μm-deep YAG region, of which the central 20μm is doped with 1at.% Nd, and sapphire cladding layers, fabricated by Onyx Optics via the direct bonding technique. The pump sources were two fast-axis collimated diode bars producing a total of 58W of output power together for 48A from the power supply. Fig. 4.11 (a) illustrates the experimental arrangement for side-pumping the double-clad Nd:YAG waveguide, and the real experimental set-up is shown in Fig. 4.11 (b).

Water-cooled and with a peak wavelength of 807nm at the maximum current, the two diode bars were both enclosed in a protective housing with an anti-reflection (AR) coated exit window. In the guided axis, a graded-refractive-index rod lens from Doric lenses of ~1mm focal length focussed the y-axis collimated beam, while a cylindrical lens of 19mm focal length focussed the diode slow axis through a 5mm-wide aperture, such that it is less than 10mm wide at the input side-face of the guide. The aim of focussing through the aperture is to break the symmetry of the pumping scheme and thus to minimize the coupling of unabsorbed pump light from one diode into the other. The waveguide was mounted on a precision 6-axis translation stage, with which the waveguide position could be precisely adjusted with respect to the focus of the pump beam, and with a thin layer of thermally conductive adhesive the bottom of the waveguide was attached to a copper block, which was not actively cooled.

4.3.3 Laser characterisation

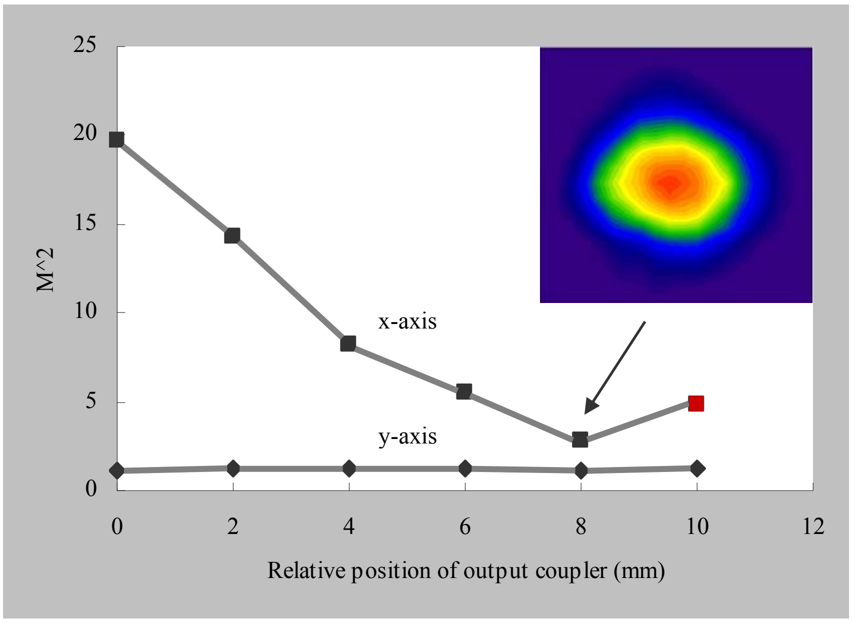

Figure 4.12 Output beam quality factor against relative position of the output coupler, with T=19% and an optimum cavity length of ~120mm. The inset shows the optimized collimated output captured on a CCD camera.

The laser performance was characterised by studying the output spatial mode and the slope efficiency. The laser output M^2 values were measured using a Coherent Modemaster M^2 meter for a cavity output coupling of 19%, plotted with varying cavity length. It should be mentioned here that the laser performance became unstable when the cavity length is beyond ~120mm, so that the plotted curve stops at the red point shown in Fig. 4.12.

It is shown that the guided axis remains diffraction-limited in all cases (M^2<1.2), while the best beam quality factor in the non-guided axis is M^2=2.8. At this position, the output beam profile appeared approximately Gaussian in both axes and the near diffraction-limited beam profile was observed from the extended cavity, after a single cylindrical lens was used to further collimate the output in the x-axis before a CCD camera. The beam profile is shown in the inset to Fig. 4.12.

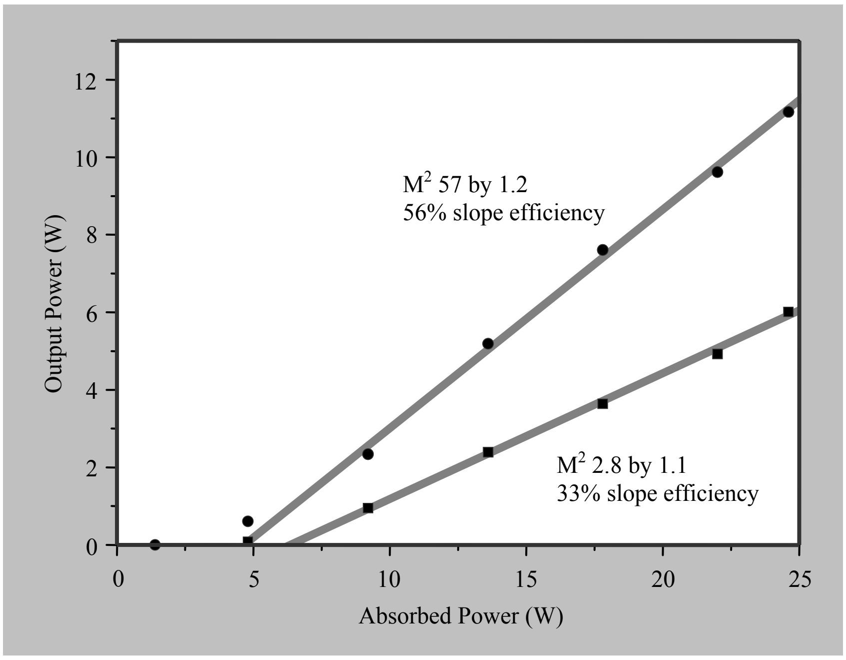

Figure 4.13 Output power against absorbed pumped power for the high-brightness and multimode cavities and an output coupling of R_{oc} = 0.70.

In the high brightness configuration, the output coupling was optimised and $R_{oc} = 0.70$ was found as the best value. With this output coupler, optimising the cavity length for output power rather than beam quality, a slope efficiency of 56% was gained with M^2 values as high as 57 in the slow axis. When the cavity length was adjusted in order to achieve high-brightness output, the slope efficiency was found to be 33%, as shown in Fig. 4.13.

This change in slope efficiency can be explained by considering the spatial mode overlap of the gain and the multimode or single mode laser signal. In the non-guided axis, the mode gives a worse spatial overlap with the step-like gain profile when it becomes near-Gaussian, as the fundamental mode cannot efficiently extract the gain at the edges of the waveguide.

By optimising the output coupling and cavity length for output power, the optimum $R_{oc} = 58\%$ was found, giving a maximum power of 12.2W, with a multimode profile in the non-guided axis as expected. However, by varying the cavity length to obtain the high-brightness operation with this output coupler, it was found that the beam quality in the non-guided axis became significantly degraded at higher pump powers with M_x^2 values of >6. It thus shows that the cavity with lower reflectivity seems to have a weaker control of the resonating spatial mode of the cavity and a tendency to go towards the behaviour of the multimode output of the monolithic waveguide.

4.3.4 Discussion

Now we compare the maximum possible slope efficiency for the Nd:YAG waveguide laser investigated here with its experimental value, at the high-brightness operation. For a four-level laser, the slope efficiency with respect to absorbed pump power is given by [18],

$$\eta_{slope} = \frac{\lambda_p}{\lambda_l}\left(\frac{-\ln R_{oc}}{-\ln R_{oc} + L}\right)\eta_{pl} \qquad (4.25),$$

where λ_p and λ_l are the pump and the laser wavelengths, respectively, R_{oc} is the reflectivity of the output coupler, L is the round-trip loss in the cavity excluding the output coupling, and η_{pl} is a spatial overlap factor which is dependent upon the spatial distributions of the pump beam and lasing mode in the laser medium and is given by [18],

$$\eta_{pl} \approx \frac{\left[\int_{cavity} r_p(x,y,z)\phi_0(x,y,z)dV\right]^2}{\int_{cavity} r_p(x,y,z)\phi_0^2(x,y,z)dV} \quad (4.26),$$

where $r_p(x,y,z)$ and $\phi_0(x,y,z)$ are normalised pump and laser spatial distributions. According to the experimental set-up it is assumed that the pump spatial distribution $r_p(x,y,z)$ is uniform with respect to the waveguide structure (width w_c, doped core thickness t_{core}, and length l),

$$r_p(x,y,z) = \frac{1}{w_c t_{core} l} \quad \text{for } |x| \le \frac{w_c}{2},\ |y| \le \frac{t_{core}}{2},\ 0 \le z \le l \quad (4.27),$$

and that the laser mode is an elliptical Gaussian distribution with beam waist, ω_{lx} and ω_{ly}, in the non-guided and guided axes respectively, averaged over waveguide length l,

$$\phi_0(x,y,z) = \frac{2}{\pi\omega_{lx}\omega_{ly} l} \exp\left[-2\left(\frac{x^2}{\omega_{lx}^2} + \frac{y^2}{\omega_{ly}^2}\right)\right] \quad (4.28).$$

In the guided axis, it is assumed that the lasing fundamental mode is well restricted within the 30μm-deep YAG layers in this experiment, so ω_{ly} is expected to be $1/3$ of this value (10μm), i.e. $\omega_{ly} = t_w/3 = t_{core}/2$. Correspondingly, in the non-guided axis, we assume that the full width of the fundamental mode fills the width of the waveguide, w_c, so that ω_{lx} can be written as $w_c/3$. With these two parameters substituted into equations (4.27) and (4.28), η_{pl} is calculated out to be 0.48. Therefore the maximum possible slope efficiency for this Nd:YAG waveguide laser lasing at 1064nm and pumped at 808nm, is 36% (assuming negligible cavity round trip-loss), which shows a good agreement with our experimental result ($\eta_{slope} = 33\%$). It is understandable that higher-order modes would fill out in plane to get better overlap with the step-profile pump distribution, which explains the higher slope efficiency ($\eta_{slope} = 56\%$) obtained with multimode operation.

4.4 Summary

In summary, the use of an extended cavity was demonstrated to control the output spatial mode of a diode bar side-pumped slab waveguide laser. Multimode output power larger than 10W was obtained from the waveguide with a slope efficiency of 56%, which is reduced to 33% when the external cavity was optimised for beam quality, obtaining M^2 values of 1.1 (in the guided axis) by 2.8 (in the non-guided axis).

The slope efficiency of the high-brightness operation could be improved by applying a zigzag lasing path in the non-guided axis, to optimise the spatial overlap of the pump volume and the lasing mode. It should be noted that this cavity scheme combined with side-pumping configuration is also compatible with diode-stack-pumping, which will be discussed in more detail in the next chapter.

4.5 References

[1] D. P. Shepherd, S. J. Hettrick, C. Li, J. I. Mackenzie, R. J. Beach, S. C. Mitchell, and H. E. Meissner, "High-power planar dielectric waveguide lasers," Journal of Physics D-Applied Physics, vol. 34, pp. 2420-2432, Aug 21 2001.

[2] J. R. Lee, H. J. Baker, G. J. Friel, G. J. Hilton, and D. R. Hall, "High-average-power Nd:YAG planar waveguide laser that is face pumped by 10 laser diode bars," Optics Letters, vol. 27, pp. 524-526, Apr 1 2002.

[3] J. I. Mackenzie, C. Li, D. P. Shepherd, H. E. Meissner, and S. C. Mitchell, "Longitudinally diode-pumped Nd:YAG double-clad planar waveguide laser," Optics Letters, vol. 26, pp. 698-700, May 15 2001.

[4] J. I. Mackenzie, S. C. Mitchell, R. J. Beach, H. E. Meissner, and D. P. Shepherd, "15W diode-side-pumped Tm:YAG waveguide laser at 2 µm," Electronics Letters, vol. 37, pp. 898-899, Jul 5 2001.

[5] J. Haisma, B. Spierings, U. K. P. Biermann, and A. A. Vangorkum, "Diversity and feasibility of direct bonding - a survey of a dedicated optical-technology," Applied Optics, vol. 33, pp. 1154-1169, March 1 1994.

[6] C. T. A. Brown, C. L. Bonner, T. J. Warburton, D. P. Shepherd, A. C. Tropper, D. C. Hanna, and H. E. Meissner, "Thermally bonded planar waveguide lasers," Applied Physics Letters, vol. 71, pp. 1139-1141, Sep 1 1997.

[7] J. I. Mackenzie, C. Li, and D. P. Shepherd, "Multi-Watt, high efficiency, diffraction-limited Nd:YAG planar waveguide laser," IEEE Journal of Quantum Electronics, vol. 39, pp. 493-500, Mar 2003.

[8] C. L. Bonner, T. Bhutta, D. P. Shepherd, and A. C. Tropper, "Double-clad structures and proximity coupling for diode-bar-pumped planar waveguide lasers," IEEE Journal of Quantum Electronics, vol. 36, pp. 236-242, Feb 2000.

[9] R. J. Beach, S. C. Mitchell, H. E. Meissner, O. R. Meissner, W. F. Krupke, J. M. McMahan, W. J. Bennett, and D. P. Shepherd, "Continuous-wave and passively Q-switched cladding-pumped planar waveguide lasers," Optics Letters, vol. 26, pp. 881-883, Jun 15 2001.

[10] J. I. Mackenzie, C. Li, D. P. Shepherd, R. J. Beach, and S. C. Mitchell, "Modeling of high-power continuous-wave Tm:YAG side-pumped double-cad waveguide lasers," IEEE Journal of Quantum Electronics, vol. 38, pp. 222-230, Feb 2002.

[11] V. Dominic, S. MacCormack, R. Waarts, S. Sanders, S. Bicknese, R. Dohle, E. Wolak, P. S. Yeh, and E. Zucker, "110W fibre laser," Electronics Letters, vol. 35, pp. 1158-1160, Jul 1999.

[12] W. Koechner, Solid-state laser engineering - Chapter 5, 5th ed. vol. 1: Springer-Verlag Berlin Heidelberg New York, 1999.

[13] D. C. Hanna, C. G. Sawyers, and M. A. Yuratich, "Telescopic resonators for large-volume TEM_{00}-mode operation," Optical and Quantum Electronics, vol. 13, pp. 493-507, Nov 1981.

[14] U. Griebner and H. Schonnagel, "Laser operation with nearly diffraction-limited output from a Yb : YAG multimode channel waveguide," Optics Letters, vol. 24, pp. 750-752, Jun 1 1999.

[15] U. Griebner, R. Grunwald, and H. Schonnagel, "Thermally bonded Yb : YAG planar waveguide laser," Optics Communications, vol. 164, pp. 185-190, Jun 15 1999.

[16] U. Griebner, R. Grunwald, H. Schonnagel, J. Huschke, and G. Erbert, "Laser with guided pump and free-propagating resonator mode using diffusion-bonded rectangular channel waveguides," Applied Physics Letters, vol. 77, pp. 3505-3507, Nov 27 2000.

[17] D. L. Lee, Electromagnetic principles of integrated optics - Chapter 4: John Wiley & Sons, 1986.

[18] K. Kubodera and K. Otsuka, "Single-transverse-mode $LiNdP_4O_{12}$ slab waveguide laser," Journal of Applied Physics, vol. 50, pp. 653-659, Feb 1979.

Chapter 5

Diode-stack side-pumped planar waveguide lasers

5.1 Introduction

Our previous work on side-pumped planar waveguide lasers concentrated on single or double-sided pumping by individual diode bars, and one fact that can be concluded from the work in Chapter 4 is that the output laser power from the waveguide was limited by the input power of laser diode bars, which typically ranges from 20 to 100W [1] from a commercially available 1-cm bar. As was discussed, the potential of power scaling ability from the planar waveguide lasers is highly supported by the waveguide geometry and the thermal handling properties. Therefore, the work that is demonstrated in this chapter was naturally motivated by the availability of high-power stacks of laser diodes, to achieve higher output power from these high-*NA* planar waveguide lasers.

A diode stack contains a number of diode bars, which are arranged in the form of a stack (see Fig. 5.1 for example). The number of the bars and how they are stacked up largely depend on the requirements of the laser system input power and the shape of the actual laser medium. Such an arrangement can then be fabricated by cleaving linear diode laser arrays from a wafer, attaching them to thin heat sinks, and stacking these assemblies so as to obtain a periodic array of diode bars and heat sinks. In the micro-channel cooling approach [2], each individual diode bar has its own internal liquid heat exchanger which consists of a silicon-glass-silicon structure. For higher power density from the array, the diode bars need to be as close to each other as possible, but on the other hand some reasonable thickness of the heat sinks must be assured to get efficient cooling. Micro-lenses are often used to collimate the output in the fast-axis of each bar.

Figure 5.1 A photo of a typical diode stack structure with the collimating micro-lenses, downloaded from www.nuvonyx.com.

Previous to this work, diode-stack pumping had only been demonstrated with relatively thick (200µm) planar waveguides, using a face pumping scheme with a reflective pump chamber to get reasonable absorption [3] in the waveguide. Nevertheless, it has been pointed out that in-plane pumping allows much thinner waveguides and thus provides access to the full range of waveguide advantages such as high optical gains, low threshold, and spatial-mode control, etc [4]. Moreover, the edge-pumping geometry promises better power scaling than face pumping in the important case of quasi-three-level systems, such as Yb^{3+} doped lasers, due to the greater freedom of choice over the doping level and thickness of the guide [5].

According to equation (4.1), a 30µm-thick, 0.46-NA YAG/sapphire guide with a Nd:YAG doping core would allow diode pumping with M^2 values in the fast axis of <17, for a pump wavelength of $\lambda \approx 0.81\mu\text{m}$.

The next section describes the design of the system of coupling optics, by applying both theoretical modelling and experimental characterisation, with the eventual aim of scaling a diode-stack-pumped planar waveguide laser to deliver more than 100 watts of output power.

5.2 Design of coupling optics

The diode stacks used in these experiments were made by Nuvonyx Inc., consisting of 3 micro-lens-collimated 1cm-long 60W-bars (thus offering a maximum power of 180W), with a 2.4mm pitch, and a fast axis $1/e^2$ divergence of $\theta \approx 3\,\text{mrad}$ (shown schematically in Fig. 5.2). The stacks available for test were divided into two groups by different wavelengths, which were around 808nm and 942nm, respectively. Therefore, it can be easily calculated that the stack shown here provides an approximate fast-axis M_y^2 value of $\theta D/\lambda \approx 22$, for example, at the wavelength of 808nm suitable for Nd^{3+} pumping.

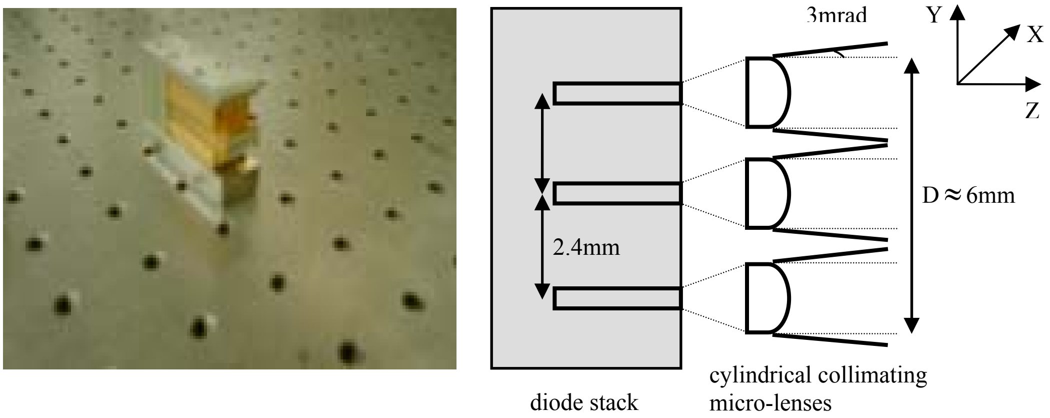

(a) (b)

Figure 5.2 (a) Photo and (b) schematic for the collimated diode stack structure.

Here we develop a theoretical design and carry out preliminary experimental work to successfully focus the 6mm-high pump beam into the waveguide (which typically has a core depth of tens of microns) without introducing significant aberrations; while on the x-axis it is relatively easy to maintain the 1cm beam width before the waveguide aperture (usually 1cm long according to our previous designs).

Three steps were taken to determine an appropriate lens system that would be applied into further experiments: (1) a commercially available optical propagation software ZEMAX® was used to trace the beam from the diode stack as it passes through various lens combinations in order to achieve the smallest possible y-axis beam waist (preferably less than 100μm diameter) incident on the waveguide side face; (2) the corresponding optical systems were then set up experimentally in order to measure the y-axis beam quality and the waist size, with the aid of a Gentec Beam-Scope; (3) after the first two steps, the lens combinations selected for the laser system was tested by the technique of knife-edge [6], to examine their power delivery efficiency through a slit that had the width of the desired waveguide aperture. It should be mentioned that the three steps were not completed strictly one after the other, because the experimental work would help to determine the right lens combination that could be modelled in theory, and vice versa (see Fig. 5.3). They will be introduced respectively next.

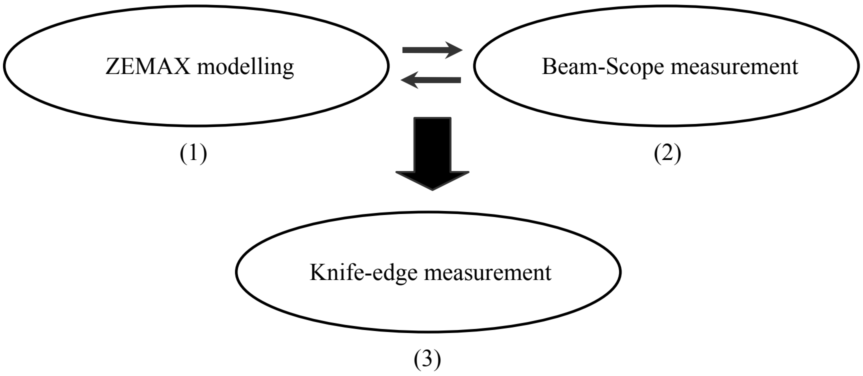

Figure 5.3 Procedure of the design of the diode-stack-to-waveguide coupling optics.

Zemax is a software package published by Zemax Development Corporation, USA. It is an optical propagation program which can model, analyse, and assist in the design of optical systems. Zemax Gaussian beam calculation provides detailed descriptions of both ideal and multi-mode M^2 Gaussian beam data, such as beam size, beam divergence, and waist locations, as a given input beam propagates through a certain lens system. The ability for Zemax to deal with the propagation of multimode beams was especially useful for the modelling of the beams from a diode stack. When the performances of different lens combinations were compared, it gave the right trends (as shown by later experiments), and also made useful suggestions on the relevant lens distances, which was one of the most important parts of the optical design. Nevertheless, this multi-mode beam calculation is based on paraxial ray data without introducing any aberration and cannot be trusted for systems that have large aberrations. Since the aberration factors must be taken into account in our real lens set-up and the light radiation from the diode stacks cannot be treated strictly as Gaussian in shape, Zemax modelling results can provide useful directions but should not be considered as the only source for the system design.

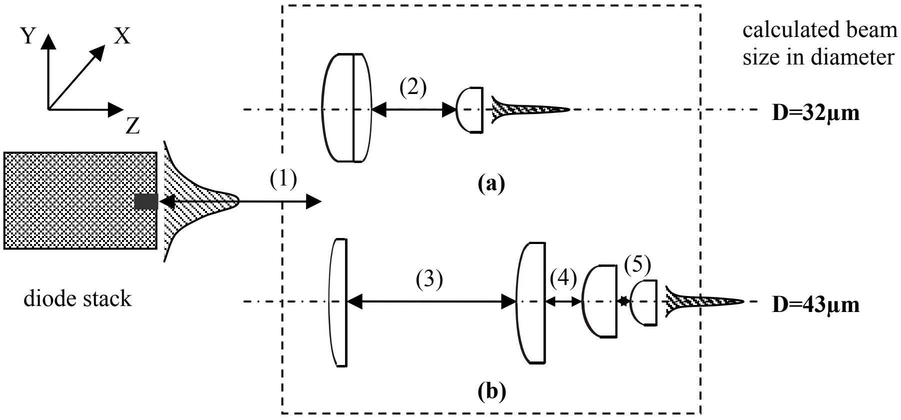

The distances above are: (1) 150mm, (2) 40mm, (3) 220mm, (4) 30mm, and (5) 3.25mm.

Figure 5.4 Two lens combination models on the y-axis of the diode and the beam size results given by Zemax. The two lens combinations are: (a) Doublet lens (focal length=60mm) + Cylindrical lens (f=4mm), and (b) Four cylindrical lens with focal lengths 300mm, 100mm, 12.7mm and 4mm from left to right.

Different lens combinations were explored in Zemax, using various commercially available lens types (spherical lenses, cylindrical lenses, and doublet lenses) and focal lengths, and the optimum combination with the relevant lens distances was found. During the modelling, cylindrical lenses, doublet lenses, and their combinations were preferred, due to the fact that cylindrical lenses introduce the least beam shaping and allow independent control on both axes, and that doublets outperform spherical lenses by their aberration correcting ability. According to the Gaussian beam calculation results, two combinations presented smaller beam waist after the lens system compared to others and were chosen to be tested experimentally. Fig. 5.4 shows these two coupling optics set-ups and the Gaussian beam calculation results.

The experiments were set up according to Fig. 5.4 as well, to measure the y-axis beam quality M_y^2 and the real beam sizes, which certainly would be different from the theoretical results due to the aberrations. Firstly, the x-axis was focussed with a cylindrical lens, which would guarantee that the considerably divergent beam in the x-axis can be completely caught by the beam scope for measurement precision. Secondly, after attenuating the beam via two wedge prisms to reduce the incident power and passing it through the focussing system described in Fig. 5.4, the beam width was measured with a Gentec Beam-Scope scanning slit, which was mounted on a translation stage to give the measurement across the beam Rayleigh range.

Owing to its diversity of possible definitions, the beam width can be measured by the beam scope in two ways, which gives "$1/e^2$" width and the "variance" width, respectively. The "$1/e^2$" width is the value at which the intensity falls to $1/e^2$ of the peak intensity, while the "variance" width σ_x is obtained by evaluating the second moment of the beam intensity profile $I(x,y)$ across the transverse coordinate x (or alternatively across the y coordinate) in the form [7],

$$\sigma_x^2 = \frac{\int_{-\infty}^{+\infty}(x-x_0)^2 I(x,y)dxdy}{\int_{-\infty}^{+\infty} I(x,y)dxdy} \qquad (5.1),$$

where x_0 is the centre of gravity of the beam, which travels rigorously in a straight line as the beam propagates. These two sets of beam widths were both measured by the Beam-Scope along the Rayleigh range, and then a Gaussian-propagation fitting function was then applied to determine the beam propagation factor M_y^2. The two sets of experimental results are shown in Table. 5.1.

Table 5.1 A comparison of the experimental results and Zemax modeling on the optimum lens combination for the diode-stack beam focusing, alongside the power delivery efficiency through a 50μm aperture and a 30μm aperture, respectively.

Combinations	Experimental results				Zemax Gaussian beam calculation (D)	Power-delivery efficiency of the 50μm slit (%)	Power-delivery efficiency of the 30μm slit (%)
	D_v	M_v^2	D_e	M_e^2			
D60mm+C4.0mm	96	42	40	9	32	80.6	53.6
C300mm+C100mm+ C12.7mm+C4.0mm	70	29	33	9	43	83.0	54.1

Notes:

a) For the lens combinations, the capital D denotes "doublet lens", while the capital C denotes "cylindrical lens", followed by the focal length of the corresponding lens.

b) In Zemax, the initial M^2 and the fast axis $1/e^2$ divergence for the diode source were set as 22 and 3mrad, respectively.

c) Unit for the diameter (D, D_v and D_e): μm. D_v denotes "variance" diameter, while D_e denotes "$1/e^2$" diameter. The corresponding M^2 values are M_v^2 ("variance") and M_e^2 ("$1/e^2$"), respectively.

From Table 5.1, it is shown that for both combinations D_v is larger than D_e, which indicates that the input beam that the beam scope measured in the experiment is not well fitted to a Gaussian shape, leading to a big variance in beam size. The fact that D_e is much smaller means that, although the beam shape is not "Gaussian-like", much of the power can be focussed into a relatively small aperture, as can be seen by later slit transmission results. The two significantly-different M^2 values gained from these two methods (42 and 9 for the first combination) prove again that the whole beam has a poor beam quality, due to its beam shape with two big wings at low intensity level, but the part of beam that contains more than 80% of the input power has got a much better propagation factor, which can satisfy the requirements of the waveguide aperture discussed previously. The all-cylindrical-lens system gives slightly better results, but has a more complicated set up.

As a final assessment, the two focussing systems were then tested to see how much power they could deliver through a 50μm slit. The slit took the place of the Beam-Scope and a thermal power meter was used to measure the powers in front of the slit and behind it, the ratio of which gave a power-delivery efficiency, which were 80.6% and 83.0% for the two lens systems listed in Table 5.1. This proved again that more than 80% of the power from the diode stack could be confined in a small area although the variance diameter could be much larger.

Hence, it can be concluded that these two designed lens systems could be applied to the real coupling system for diode-stack-pumping the waveguide, and should deliver more than 80 percent of the pump power after the coupling optics to a waveguide aperture of 50μm in depth. The doublet-and-cylindrical combination is preferred because it gives a more compact pumping system and easy set-up, although experimentally the four cylindrical lens system performs slightly better.

5.3 Laser operation

As stated in the last section, ideally a 50μm-thick waveguide is preferred to get good launch efficiency with the diode stack pumping system. Such a waveguide (corresponding to the design of section 5.4) was ordered from Onyx Optics to be fabricated via the direct bonding technique. However, a suitable guide was never delivered. Hence, the 30μm-thick Nd:YAG double-clad waveguide was characterised instead.

5.3.1 Pump and cooling set-up

The two diode stacks were cooled with the micro-channel cooling technique by running water that was maintained at 20°C, at which temperature they had a centre wavelength of 807nm and produced a maximum output power of 172W and 166W respectively at the maximum current of 69A from their individual power supplies. Therefore, the available pump power for the double-side pumping was 338W immediately after the two diodes. On each side of the waveguide, one diode stack was mounted together with the coupling lenses on a precision 5-axis translation stage allowing easy positioning with respect to the alignment of the pump beam.

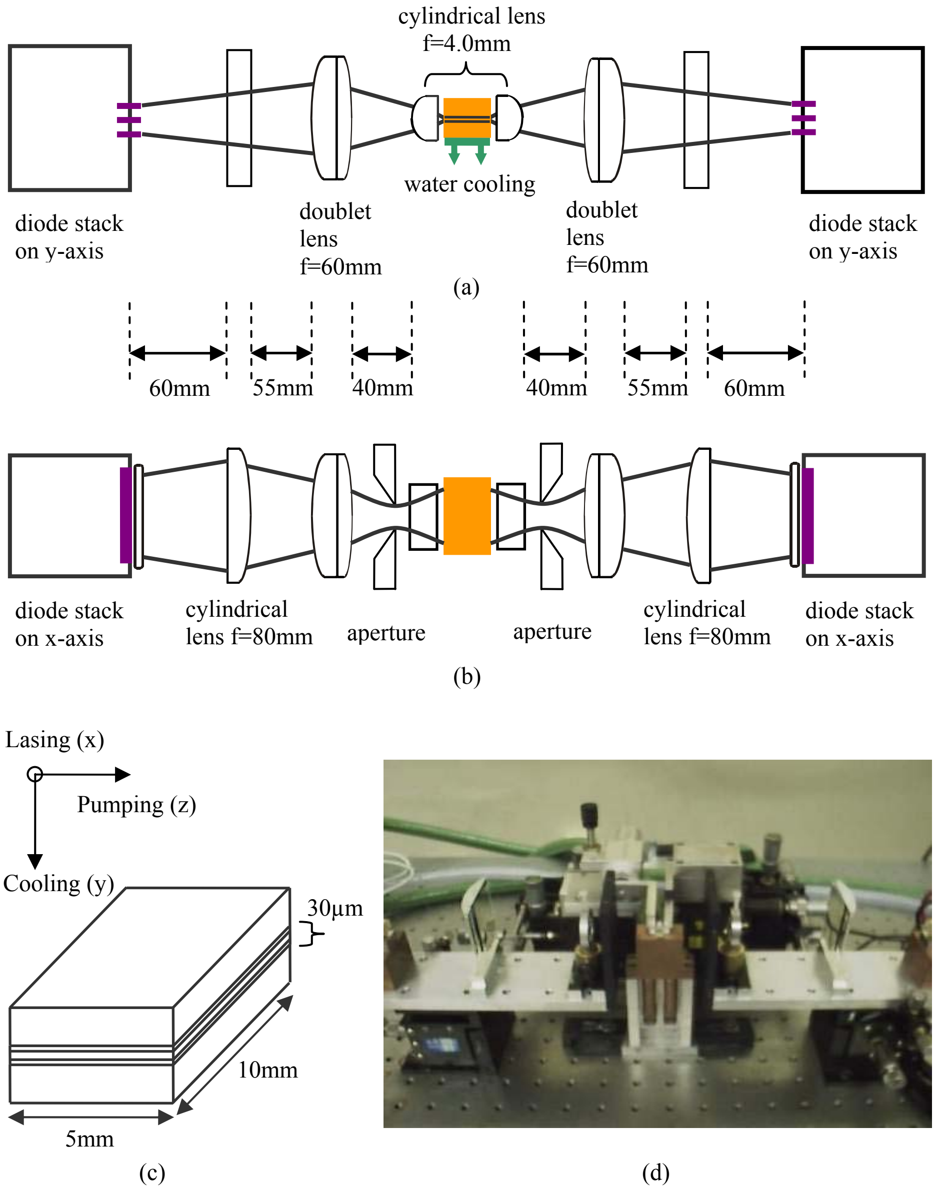

Figure 5.5 (a) Schematic of coupling optics on the y-axis and waveguide cooling scheme, and (b) coupling optics on the x-axis, for the diode-stack double-side-pumped waveguide laser; (c) the double-clad waveguide structure with the dimensions; and finally (d) a photo of the set-up.

The pump and cooling set-up is illustrated in Fig. 5.5. The waveguide crystal is 5mm wide, 7mm thick by 10mm long and consists of a 30μm-thick YAG region, of which the central 20μm is doped with 1at.% Nd, and sapphire cladding layers, fabricated by

Onyx Optics via the direct bonding technique. The bottom of the waveguide was fixed to a copper block via the direct contact with a thin layer of thermally conductive adhesive, and the copper block was water-cooled at 15°C by a recycling water loop. The side faces of the waveguide were anti-reflection (AR) coated at the pump wavelength. To set up a monolithic laser cavity, one lightweight high-reflection (HR) mirror was attached to the rear end-face of the waveguide via the surface tension of a thin layer of fluorinated liquid, and the other end face was coated directly with an output coupler transmission of 20% ($R_{oc} = 0.80$) at 1064nm.

As shown in Fig. 5.5 (a), on the y-axis (fast axis of the diode), a doublet lens (focal length f = 60mm) and a cylindrical lens (f = 4mm) reduced the y-axis pump beam size to ~40µm in diameter, which had a transmission efficiency of 53.6% through a 30µm-wide slit. Both lenses are AR coated at the pump wavelength. The f = 4mm cylindrical lens was mounted on a 5-axis translation stage to give precise focussing of the pump beam, while the diode stack and the doublet were mounted on a common stage along with the x-axis lens on each side, with relatively course adjustment. On the x-axis (see Fig. 5.5 (b)), a cylindrical lens of 80mm focal length combined with the doublet lens focussed the diode stack slow axis through a 4.5mm-wide aperture, such that it was about 8mm wide before the pump beam was incident on the side-face of the waveguide. As before, the apertures broke the symmetry of the pumping scheme and thus minimized the coupling of unabsorbed pump light from one diode into the other.

5.3.2 Laser operation with a monolithic cavity

5.3.2.1 Laser performance

The pump beams from the two diode stacks were launched into the two AR coated side faces of the waveguide separately and the launch efficiencies were optimised for each stack by adjusting the focussing optics to give the best single-side pumping laser performance. As shown in Fig. 5.6, the maximum output power of 35.3W and 23.5W were obtained in this way, with the diode pump power of 160W and 155W.

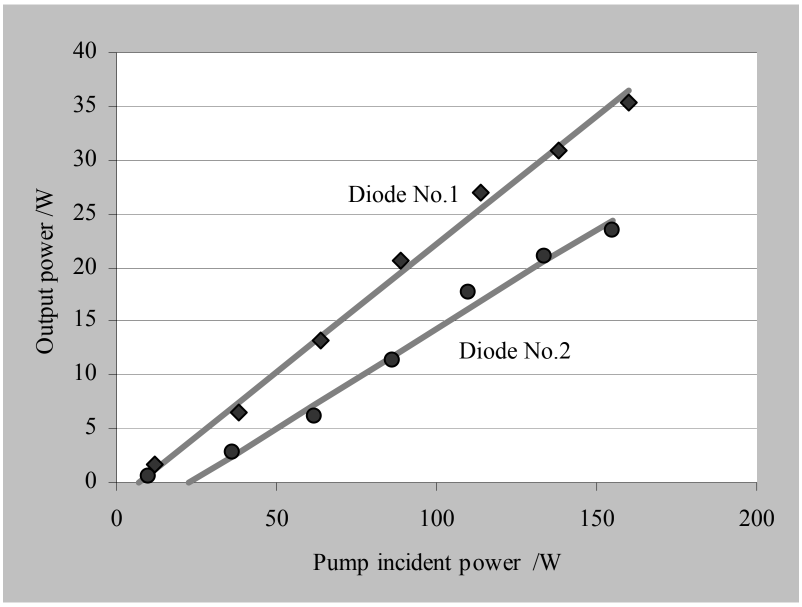

Figure 5.6 The 30µm Nd:YAG waveguide laser output power versus incident pump power with single-side pumping from two diode stacks No.1 and No.2, respectively.

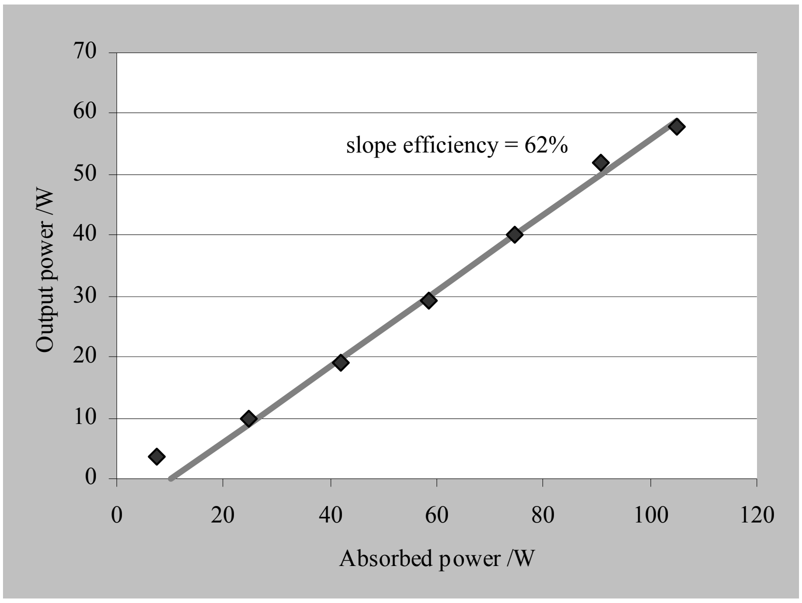

Figure 5.7 The 30µm Nd:YAG waveguide laser output power versus absorbed pump power with double-side pumping from two diode stacks.

After the focussing optical system was fully optimised from both sides of the waveguide, double-side pumping was then undertaken with the results shown in Fig.

5.7. 58W of output power was obtained, for a total incident diode power of 315W. The absorption length for the diode stacks in bulk 1at.% Nd:YAG is ~3mm at the pump wavelength, and it is expected that this length will increase by the ratio of the waveguide thickness to the doped region thickness. Therefore, it can be assumed that the 5mm width of the waveguide is approximately one absorption length, and double-side pumping helps to obtain a relatively uniform inversion with just a small dip in the centre. Given the absorption efficiency and the measured transmission through a 30μm aperture it is estimated that for these experiments 33.5% of the incident diode pump light is absorbed. Hence, a slope efficiency of 62% was gained with respect to absorbed power.

Two factors should be noted here, first the 20%-transmission output coupler was directly coated onto the waveguide end-face initially for the experiments carried out in Chapter 4, and was thus not optimised for this set-up to give the best performance, and secondly the temperature of the diodes, and hence the Nd^{3+} absorption efficiency, was optimised at relatively low output power from the stacks. Therefore, the slope efficiency may be even higher than this value as the diode wavelength and the output coupler may not the fully optimised, especially at the highest-power laser operation.

However, at the maximum power shown in Fig. 5.7, the upper sapphire cladding layer cleanly detached from the rest of the waveguide, which left the beam quality of the laser output unconfirmed, other than to note that it was single lobed. However we would expect that it was again diffraction-limited in the y-axis and highly multimode in the x-axis. Immediately after the waveguide damage, some fractures were observed under the microscope on the two end faces of the waveguide, as shown in Fig. 5.8.

It can be seen that, on the end face where the HR mirror was attached, there were some big chips found, however no significant damage was found on the two AR-coated side faces or the AR coated end-face, except that some coating had dropped off. A thermal analysis concerning this damage process will be included in the next section. The two end faces were then both re-polished to be damage-free, one of which was AR-coated at 1064nm afterwards, to be prepared for laser operation with an extended cavity. Therefore, the basic operation should remain the same as the sapphire outer cladding is just replaced by an air outer cladding.

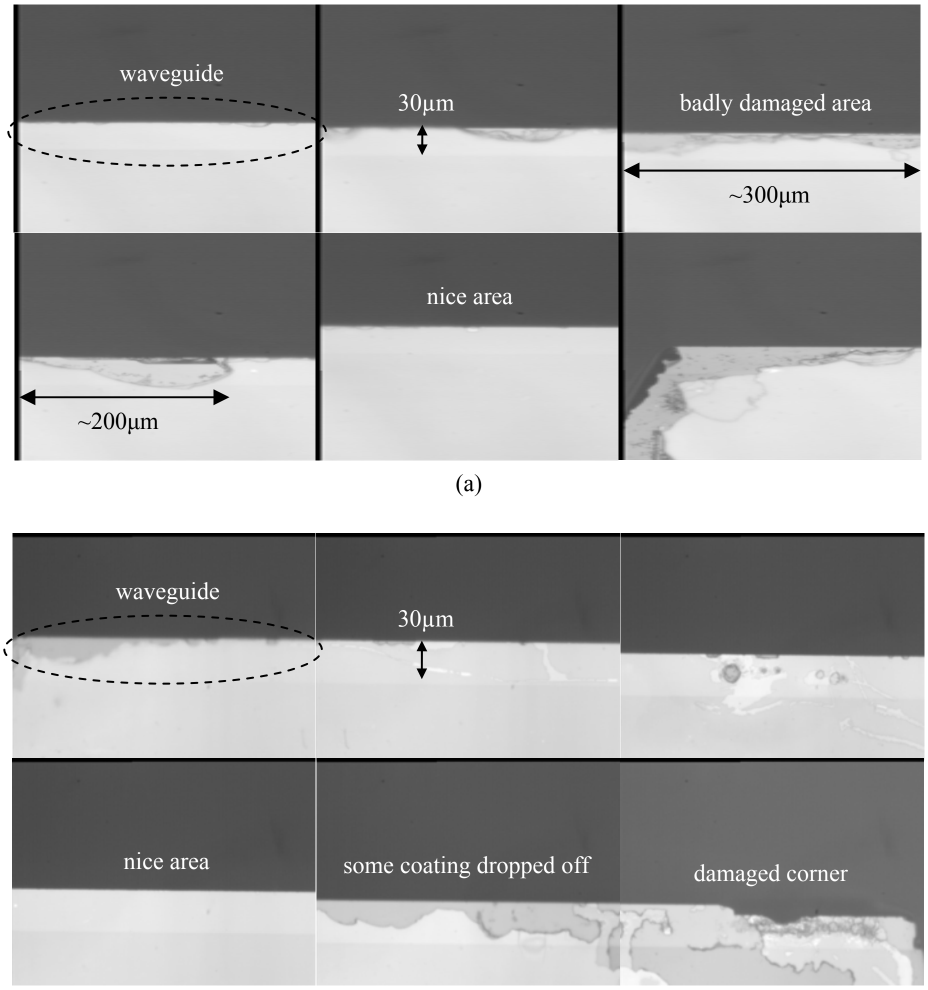

(a)

(b)

Figure 5.8 Some typical areas observed under microscope on (a) the HR-mirror-attached end face, and (b) the 20%-output-coupler end face of the waveguide after the upper sapphire cladding layer dropped off from the rest of the waveguide.

5.3.2.2 Discussion

As stated in section 4.3.4, the expected slope efficiency with respect to absorbed pump power, η_{slope}, can be calculated from,

$$\eta_{slope} = \frac{\lambda_p}{\lambda_l}\left(\frac{-\ln R_{oc}}{-\ln R_{oc} + L}\right)\eta_{pl} \qquad (5.2),$$

where R_{oc} is the reflectivity of the output coupler, L is the round trip propagation loss, λ_p is the pump wavelength, λ_l is the laser wavelength, and η_{pl} is the factor accounting for the spatial overlap of the pumped region and the laser radiation. As the pump region is fully within the lasing mode in the guided axis and highly multi-mode output is expected in the non-guided axis, it can be assumed that $\eta_{pl} \sim 1$. Therefore, the experimental value for the slope efficiency of 0.62 places an upper limit on the round trip loss exponent L of 0.05, which yields a waveguide propagation loss of ~0.1dBcm^{-1}, in good agreement with loss commonly found for this type of direct-bonded waveguide at 1μm [4]. It should be mentioned that this result is also similar to the 56% slope efficiency measured in this waveguide with diode bar pumping under multimode operation, as reported in Chapter 4.

The thermal load produced by the Nd:YAG waveguide core due to quantum defect can be written as,

$$P_{tl} = P_{abs}(1 - \frac{808}{1064}) \qquad (5.3),$$

where P_{abs} is the absorbed power. In this experiment the maximum absorbed power was 105W, which gave a thermal load of 25.3W when the damage happened. According to section 2.4 in Chapter 2, it can be calculated that with single-side cooling the maximum average temperature in the 30μm waveguide core was 151°C higher than that of the heatsink, which was set as 15°C. As far as the surface stress is concerned, the calculated thermal surface stress $\sigma_s << \sigma_{\max}$, which indicates that this clean detachment was not caused by surface stress fracture, but rather by the difference in thermal expansion coefficients of the YAG and sapphire layers, at an estimated thermal load of 50W per square cm of cooling area. According to the feedback from Onyx Optics, a thermal shock limit of about 190°C for this type of YAG/sapphire composites had been discovered before by other research groups; and it was suggested that temperatures beyond this limit could break the bonding between the YAG and sapphire layers for this direct-bonding regime. However, it is believed that the consequent limitation on pump power can be improved by cooling from both faces of the waveguide (in this case the core temperature drops from 169°C to 84°C) and by using Yb instead of Nd to lower the quantum defect by almost 2/3. With this in mind a design for a ~150W waveguide laser is developed in section 5.4.

It should also be noted that if we had been able to obtain 50μm-thick waveguides the efficiency with respect to incident diode power would be significantly higher as the launch efficiency would be expected to rise from ~50% to ~80% in accordance with our slit transmission measurements.

5.3.3 Laser operation with an extended cavity

Following the work in Chapter 4 to obtain near-diffraction limited performance in both axes, an extended cavity was set-up after the waveguide end faces were properly polished and one of them was coated with an anti-reflection thin film. The pump and cooling set-up had no difference from Fig. 5.5, while the extended cavity set-up, as shown in Fig. 5.9, aimed to produce a near-symmetric shaped output beam (see Fig. 5.10) using a spherical-and-cylindrical lens combination, which is of interest in many applications.

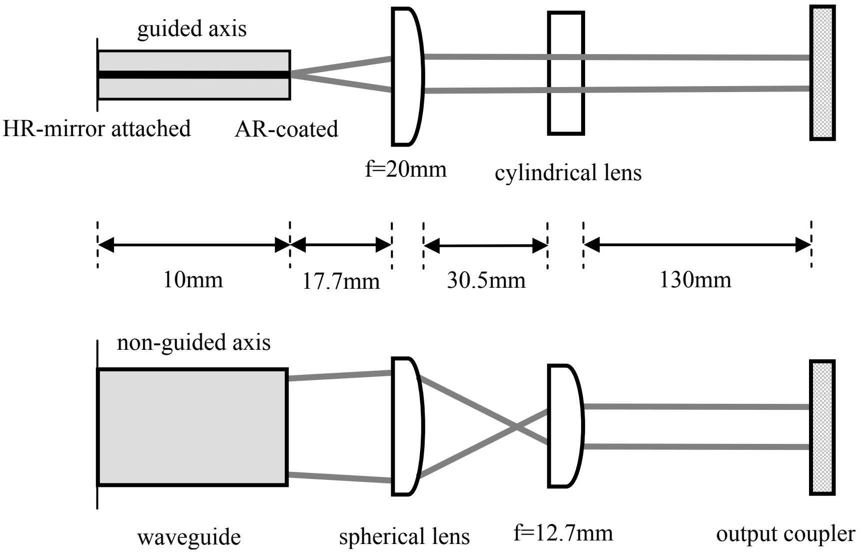

Figure 5.9 Schematic of the extended cavity configuration combined with the stack pumping.

The cavity set-up started with a HR mirror attached to one end of the waveguide, which was followed by two AR coated lenses, a spherical lens f=20mm and a cylindrical lens f=12.7mm, and an output coupler positioned such that the beam from the waveguide would be coupled back with the same size after a round trip to and from the output coupler mirror. Sharing the same principles with the cavity designed in Chapter 4, this cavity has two main advantages: (1) the first lens following the waveguide (spherical f=20mm in this case) is allowed more space from the waveguide and therefore enables easier optical alignment with more freedom, and (2) the beam radii at the output coupler position from both axes of the waveguide can be nearly equalised so that it gives a more circularised laser output. Fig. 5.10 shows a theoretical modelling result on the beam radii in the two axes against the distance from the waveguide HR-mirror-attached end to the output coupler mirror.

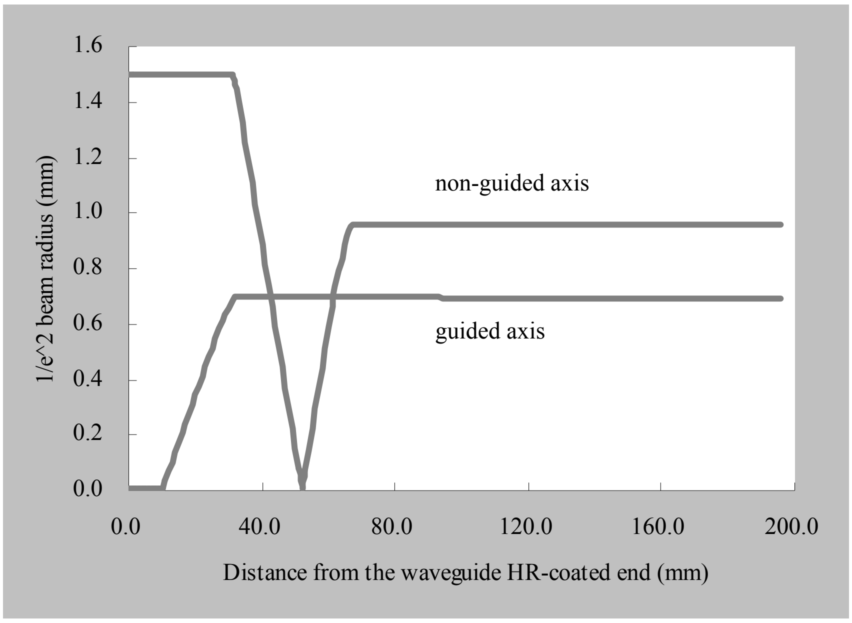

Figure 5.10 Modelling of the spherical+cylindrical lens extended cavity, showing beam radii for the two axes of the waveguide with the change of the cavity length.

With double-side pumping, nearly 20W was obtained with an incident pump power of 272W. However, this laser output power could not be achieved again, and thus it was suspected that the waveguide had been damaged again, especially when it was not protected by a cladding layer. Nevertheless, the experiments were carried on under these circumstances to optimise the laser output power and also the beam quality until the HR mirror dropped as the fluorinated liquid dried out. A slope efficiency of 22% was gained with respect to absorbed power with a 30%-transmission output coupler, giving a maximum output power of about 10W, as shown in Fig. 5.11.

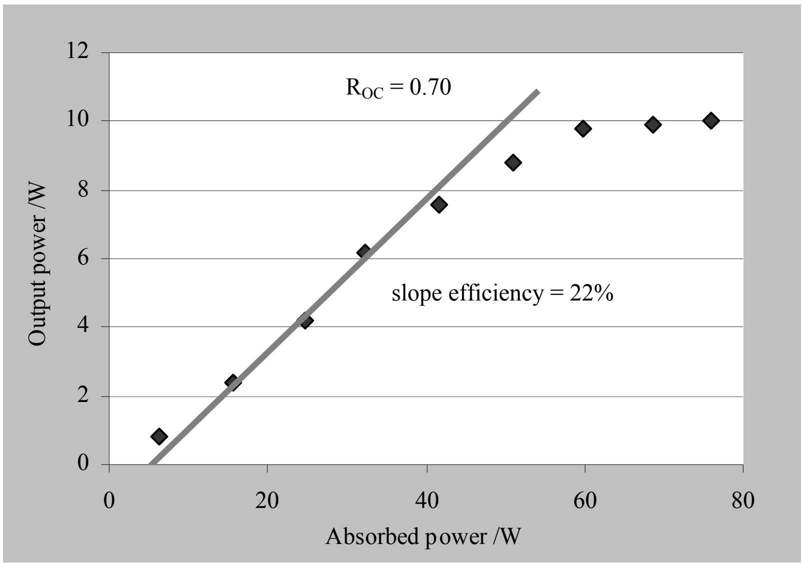

Figure 5.11 The output power against absorbed pump power of the diode-stack-pumped 30μm Nd:YAG Waveguide laser with a stable extended cavity.

The laser output M^2 values were measured using a Coherent Modemaster M^2 meter for cavity output coupling of 5% and 30%, respectively. It was found that, unlike the two-cylindrical-lens cavity discussed in Chapter 4, the position of the second lens (the cylindrical f=12.7mm lens in this case) is much more crucial to the beam quality optimisation rather than the cavity length varying by the position of the output coupler. Therefore, the beam quality was measured on both axes after the output coupler mirror in the far field, by changing the position of the second lens. M^2 values as good as 1.5 by 6.8 were obtained, but optimisation could not be properly carried out due to the damage to the waveguide, which is shown in Fig. 5.12. It should also be noted here that the measurement was under low-power operation (pump power about 22W), because difficulties were encountered at higher-power level as the HR mirror contact with the waveguide got significantly worse.

Finally, after the experiments it was confirmed under the microscope again that the two end faces of the waveguide had some serious damage that covered nearly 1/3 of the waveguide width, as shown in Fig. 5.12, which can explain the output power reduction after the first operation. Thus it suggests that the first cleaving of the sapphire cladding had left some unseen weakness in the overall structure such that it now damaged much more easily. Further experiments on this waveguide were therefore abandoned.

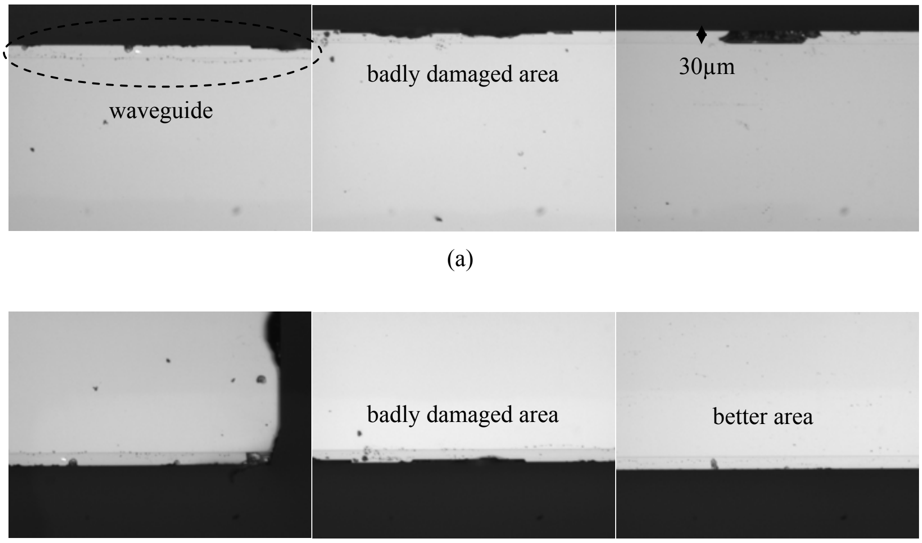

(a)

(b)

Figure 5.12 Some typical areas on (a) the HR-mirror-attached end face, and (b) the AR-coated end face of the waveguide after laser operation with an extended cavity.

5.4 Further power scaling expectations for planar waveguide lasers

Although no proper waveguide with a 50μm-thick core was fabricated in the end, for power scaling purposes here in this section a model will be presented on a diode-stack-pumped Yb:YAG planar waveguide laser, which is expected to produce more than 100W of output power from a single 10mm long and 5mm wide waveguide device. In this model, a double-clad high-*NA* (0.46) Yb:YAG planar waveguide is chosen as the laser medium, which can be fabricated with the direct-bonding technique from Onyx Optics, USA. The total depth of the core and inner cladding YAG layers is chosen as 50μm, which according to the experimental results in section 5.2 should allow ~80% launch efficiency for 3-bar 180W diode stacks. Based on the concept of spatial mode selection developed in [8], a 10at.% Yb-doped central portion of 30μm in depth was designed to give a rigorous fundamental mode selection in the multimode step-index waveguide. To avoid the relatively large doped central region (30µm) acting as an independent multimode waveguide itself, either a 15±1at.% Lu^{3+} doped YAG or an 8±1at.% Tm^{3+} doped YAG inner layer is chosen rather than undoped YAG to keep the index difference between the Yb-doped core and inner cladding regions to be less than 1×10^{-4} .The Lu^{3+} or Tm^{3+} doping would not absorb at the Yb^{3+}-ion pumping and lasing wavelengths. The two sapphire layers are designed to be ~0.45mm thick together, which makes the whole thickness of the structure to be about 0.5mm. The waveguide design is shown in Fig. 5.13. Theoretical expectation for the laser performance and thermal management will be discussed in the following sections under high-power diode-stack pump considerations.

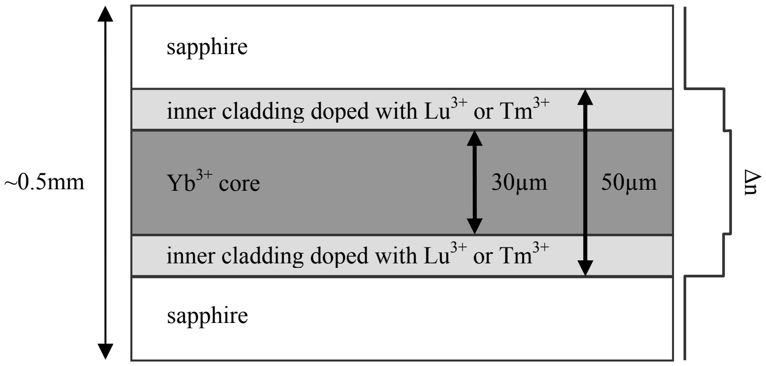

Figure 5.13 Design of the 50µm Yb:YAG planar waveguide structure.

5.4.1 Laser performance

Based on the plane-wave model [9] discussed in Chapter 2, laser performance can be predicted with the planar waveguide described above, with 360W incident pump power from two three-bar diode stacks at 942nm. Table 5.2 lists the Yb:YAG parameters used to model the lasing performance.

Table 5.2 Yb:YAG laser model parameters.

Pump 942nm photon energy	$h\nu_p$	$2.1\times10^{-19}\,J$
Laser 1030nm photon energy	$h\nu_l$	$1.9\times10^{-19}\,J$
Initial pump Stark level Boltzmann occupation factor	f_L^p	0.853

Terminal pump Stark level Boltzmann occupation factor	f_U^p	0.198
Initial laser Stark level Boltzmann occupation factor	f_U^l	0.752
Final laser Stark level Boltzmann occupation factor	f_L^l	0.054
Spectroscopic pump absorption cross section	σ_p	$7.7\times10^{-25}m^2$
Spectroscopic laser emission cross section	σ_l	$2.1\times10^{-24}m^2$
Waveguide length	l	$1\times10^{-2}m$
Waveguide width	w_c	$5\times10^{-3}m$
Doped core thickness	d_{core}	$3\times10^{-5}m$
Yb doping density	n_A	$1.38\times10^{27}m^{-3}$
Effective excited state storage lifetime	τ_{eff}	951µs
Mode fill efficiency	η_{mode}	1
Delivery efficiency	η_{del}	0.8
Pump overlap with the doped region	η_{po}	0.612
Laser overlap with the doped region	η_{lo}	0.818
Waveguide one-way cavity transmission	T_{ow}	0.91
Output coupler reflectivity	R_{oc}	0.7
Pump power from diode stack	P_p	360W
Average operating temperature	T_a	320K

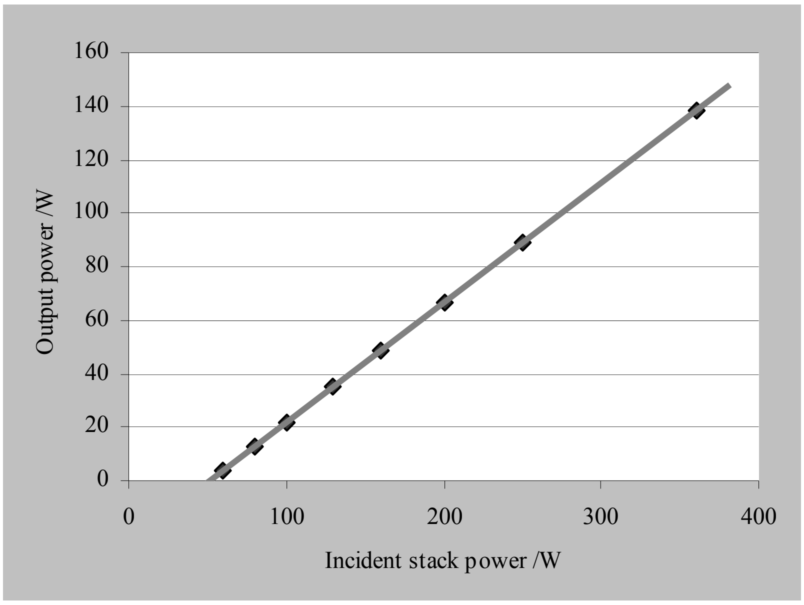

Figure 5.14 Theoretical modelling on the laser performance of a 50µm Yb:YAG planar waveguide laser pumped by two diode stacks with maximum incident power of 360W.

It should be mentioned here that: (1) the four Stark level Boltzmann occupation factors are calculated at an average operating temperature of 50°C, which is obtained from theory based on the thermal modelling in Chapter 2; (2) the delivery efficiency comes from the experimental results in section 5.2; (3) the overlap of the pump with the doped area is determined by the double-clad waveguide structure, and the overlap of the laser field with the doped area is calculated assuming that the laser operates on the fundamental guided mode. As a result, a laser threshold of 51W was calculated, and as shown in Fig. 5.14, nearly 140W of output power can be expected with the maximum incident power of 360W from two 3-bar stacks, which gives a slope efficiency of 45% with respect to incident pump power.

5.4.2 Thermal characteristics

One of the advantages of the Yb^{3+}-doped laser system is its small quantum defect and consequently low thermal load. Based on the theory in section 2.4, the temperature rise and thermal stress can be predicted in the double-clad Yb:YAG waveguide when pumped by the two diode stacks. A maximum thermal load of 22W can be calculated with the incident pump power of 360W, delivery efficiency of 80%, and the fraction of absorbed pump power of 0.903. In contrast, a Nd:YAG waveguide laser produces 49W of thermal load under the same pump conditions. The waveguide will be double-face-cooled by two heat sinks, of which the water temperatures are both set as 15°C. The waveguide structure is described in the last section. Table 5.3 lists the thermal model parameters that will be used in this model.

Table 5.3 Thermal parameters used in the Yb:YAG waveguide model described.

Heat sink temperature	T_{htsk}	$288K$
Water-cooled heat sink heat transfer coefficient	λ_{htsk}	$6000Wm^{-2}K^{-1}$
Thermal conductivity of YAG	k_y	$13Wm^{-1}K^{-1}$
Thermal conductivity of sapphire	k_s	$35Wm^{-1}K^{-1}$
Thermal load per unit volume	Q_T	$1.48\times10^{10}Wm^{-3}$
Thermal shock parameter of YAG	R_{sy}	$790Wm^{-1}$
Thermal shock parameter of sapphire	R_{ss}	$10000Wm^{-1}$

Following the equations in Chapter 2, the theoretical average temperatures of 53.7°C, 53.5°C and 52.7°C were obtained at the maximum pump power level, for the doped core, inner cladding and sapphire layer, respectively, which should be easily acceptable as to avoid similar waveguide damage stated in section 5.3.2.2. In addition, the “safety” factors on the four interfaces have values of at least ~10^2, i.e., far away from the surface stress facture limit. The modelling results show that double-face-cooling can effectively reduce the temperature in the waveguide, which points out the future direction of heat removal of this type of high-power waveguide lasers.

5.5 Summary

Firstly, a focussing optical system was developed to couple the non-diffraction-limited pump beam ($M_y^2 \approx 20$ in the guided axis) from 3-bar diode stacks into a multi-layer high-NA YAG/sapphire waveguide, with a 50µm-thick core. Secondly, a diode-stack side-pumped Nd:YAG planar waveguide has been demonstrated to produce 58W of output power with single-sided cooling. A slope efficiency of 62% was obtained, in good agreement with theoretical expectation. The limiting thermal process was found to be de-bonding of the sapphire and YAG layers at a temperature of 169°C, due to their different thermal expansion coefficients. Thirdly, a stable extended cavity was applied in this stack-pumped waveguide laser system, giving a minimum experimental M^2 value of ~7 in the non-guided axis, although these experiments were limited by further waveguide damage. Finally, a 50µm Yb:YAG waveguide laser was modelled, which can theoretically lead to ~140W of laser output power, when side-pumped by two diode stacks with incident power of 360W, and only has a maximum temperature of 54°C in the waveguide core.

5.6 References

[1] L. Marshall, "Laser Diode-Pumped Solid-State Lasers," in CLEO/QELS Baltimore, USA, 2005, p. SC165.

[2] S. A. Payne, R. J. Beach, C. Bibeau, C. A. Ebbers, M. A. Emanuel, E. C. Honea, C. D. Marshall, R. H. Page, K. I. Schaffers, J. A. Skidmore, S. B. Sutton, and W. F. Krupke, "Diode arrays, crystals, and thermal management for solid-state lasers," IEEE Journal of Selected Topics in Quantum Electronics, vol. 3, pp. 71-81, Feb 1997.

[3] J. R. Lee, H. J. Baker, G. J. Friel, G. J. Hilton, and D. R. Hall, "High-average-power Nd:YAG planar waveguide laser that is face pumped by 10 laser diode bars," Optics Letters, vol. 27, pp. 524-526, Apr 1 2002.

[4] D. P. Shepherd, S. J. Hettrick, C. Li, J. I. Mackenzie, R. J. Beach, S. C. Mitchell, and H. E. Meissner, "High-power planar dielectric waveguide lasers," Journal of Physics D-Applied Physics, vol. 34, pp. 2420-2432, Aug 21 2001.

[5] T. S. Rutherford, W. M. Tulloch, E. K. Gustafson, and R. L. Byer, "Edge-pumped quasi-three-level slab lasers: Design and power scaling," IEEE Journal of Quantum Electronics, vol. 36, pp. 205-219, Feb 2000.

[6] A. E. Siegman, M. W. Sasnett, and T. F. Johnston, "Choice of clip levels for beam width measurements using knife-edge techniques," IEEE Journal Of Quantum Electronics, vol. 27, pp. 1098-1104, Apr 1991.

[7] D. R. Hall and P. E. Jackson, The physics and technology of laser resonators - Chapter 9: IOP Publishing, 1989.

[8] T. Bhutta, J. I. Mackenzie, and D. P. Shepherd, "Spatial dopant profiles for transverse-mode selection in multimode waveguides," Journal of the Optical Society of America B-Optical Physics, vol. 19, pp. 1539-1543, Jul 2002.

[9] R. J. Beach, "CW Theory of quasi-three level end-pumped laser oscillators," Optics Communications, vol. 123, pp. 385-393, Jan 15 1995.

Chapter 6

Diode-stack-pumped pulsed-laser-deposited planar waveguide lasers

6.1 Introduction

Compared with the technique of direct bonding that was applied in the waveguide fabrication in the last two chapters, pulsed laser deposition (PLD) has several advantages to make itself a promising alternative to be used in high-power planar waveguide lasers. With a relatively fast growth rate, pulsed laser deposition can be less time consuming once the optimum growth conditions are found for different materials and be more flexible because during the whole procedure the film growth can be adjusted by varying the growth parameters to make custom designed planar waveguides. Moreover, PLD can produce multilayer planar waveguide structures, with different refractive index profiles (and therefore desired NAs) and deposit multi-component materials such as GGG, GSGG or YSGG on a YAG substrate, which can be successfully applied to the large-mode-area planar waveguide geometry with careful designs.

High-optical-quality thick films fabricated by the technique of PLD available at the ORC [1] allows the exploration of high-power diode-stack-pumped planar waveguide lasers. High numerical aperture GGG or YAG structures with film thickness up to 135μm were reported grown by PLD technique with high crystalline quality. In the same research group a 40μm-thick Nd:GGG film grown on YAG was operated as a laser by Ti:sapphire pumping [2], yielding low propagation loss (0.1dB/cm). Thus these films offer great potential as planar waveguide laser media in high-power diode-pumped laser systems.

A main disadvantage of the technique of PLD is the occurrence of the particulates [3] in the deposited films, which can cause scattering centres and therefore lead to additional optical propagation loss. However, it has been shown experimentally in [3] that as long as the lasing mode can be kept away from the high index difference interfaces then propagation losses can be kept low. This agrees well with the requirements for the thick multilayer waveguides for high-power diode pumping.

In this chapter, the initial diode-pumping experiments were carried out with a 50μm-thick Nd:GGG film fabricated by T. C. May-Smith, at the ORC. The waveguide was end-pumped using a diode stack that produces a maximum output power of 172W at the maximum current of 69A, with a centre wavelength of 808nm. Another 27μm-thick Nd:GGG film was fabricated with a YAG capping layer and was later characterised by Ti:sapphire pumping to confirm a self-imaging effect, which can be applied to make thick multimode planar waveguide amplifiers that re-image the input spatial properties at the exit face, and thus provide another option for spatial mode control for multimode planar waveguides. The experiments were also completed in collaboration with T. C. May-Smith.

6.2 Fabrication process

As discussed in the last section, two Nd:GGG PLD planar waveguides (50μm and 27 μm) were tested with diode-stack pumping and Ti:sapphire pumping respectively. In this section the fabrication procedure is described briefly, while more detailed discussions can be found in [4] on the deposition conditions and chosen parameters for the films.

The YAG substrate was prepared for deposition by polishing one of the side faces, followed by a thorough cleaning procedure similar to the one stated in section 3.3.2. The experimental set-up of the PLD chamber apparatus is shown in Fig. 6.1 for the deposition process. A 248nm KrF excimer laser (Lambda Physik, Germany) was set up with appropriate optics for beam transmission and focussing to produce the pulsed laser beam for ablation. The target consisted of a bulk single crystal of 1at.% Nd doped GGG and was mounted on a rotating holder (DC stepper motor in Fig. 6.1) that changed direction of rotation with a period of 1 minute, while a substrate blocker was remotely controlled to allow a pre-deposition cleaning of the target face without contaminating the substrate surface. The substrate was held by ceramic alumina half-cylinder tubes to yield minimal heat sinking, while a raster scanned CO_2 laser (Synrad, USA) was used for substrate heating.

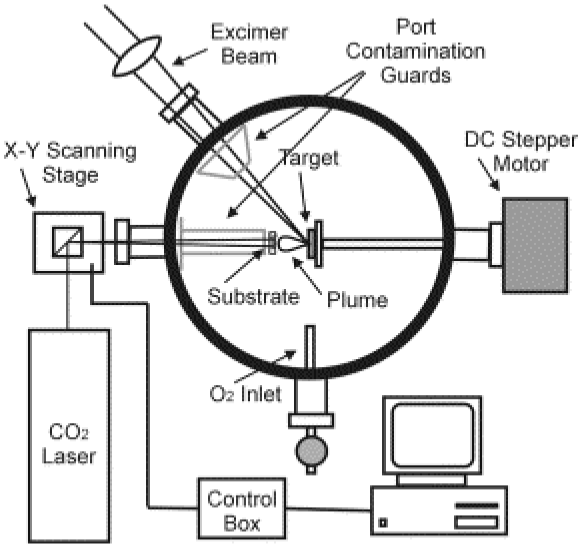

Figure 6.1 Experimental set-up of the PLD chamber apparatus [1].

Before deposition, the chamber atmosphere needed to be pumped down to below 5×10^{-3} Pa, while during the deposition process oxygen was introduced into the chamber and the pressure in the chamber was maintained at 2.0 ± 0.1 Pa by a vacuum pumping system. The excimer laser was set to produce a laser output of 200mJ per pulse at 10Hz, having an energy intensity of approximately 1.5Jcm^{-2} at the target surface. The distance between the surfaces of the target and substrate was 4cm and the substrate temperature was estimated to be between 650°C and 750°C when depositing.

The 50μm thick film was initially designed to be polished to 10mm in length and about 5-6mm in width to make it ideal for double-side pumping by 1cm-bar diode stacks. However, several cracks occurred during the polishing process on the corners of the waveguide so that the length was reduced to 7.0mm. Furthermore, more cracking could not be prevented with later polishing, and as a result the other set of opposing sides were left unpolished. Therefore, these preliminary experiments with diode-stack pumping were carried out with an end-pump configuration, as presented in the next section.

6.3 Laser operation with diode-stack pumping

6.3.1 Experimental set-up

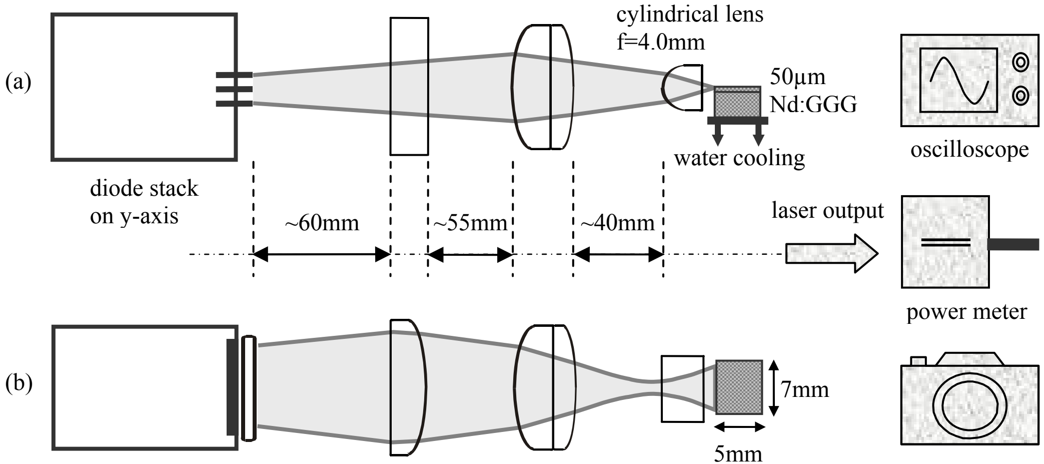

Figure 6.2 Experimental arrangement for the pump configuration and laser output analysis for the diode-stack end-pumped 50μm-thick Nd:GGG PLD waveguide laser.

The experimental set-up is shown in Fig. 6.2 for the end-pump configuration and laser output analysis for the diode-stack-pumped 50µm-thick Nd:GGG PLD waveguide laser. A three-bar diode stack was used as the pump source for the waveguide laser, mounted together with the first two coupling lenses (cylindrical lens f = 80mm and doublet lens f = 60mm) on a common stage to give relatively course adjustment, while the f = 4mm cylindrical lens was mounted on a precision 5-axis translation stage allowing easy positioning with respect to the alignment of the pump beam. The stack was cooled with the micro-channel cooling technique by running water, and once lasing was observed, the wavelength of the diode stack was tuned in a small range of about 2nm to optimise the laser threshold by changing the temperature of the cooling water. Thus, the water temperature was finally set at 24°C, where the pump source had a centre wavelength of 808nm and produced a maximum output power of 170W at the maximum current of 69A from its power supply.

The waveguide is 5mm wide by 7mm long and consists of a 50µm-thick Nd:GGG film layer on the top as the waveguide core. The bottom of the waveguide was fixed to a copper block via the direct contact with a thin layer of thermally conductive adhesive, and the copper block was water-cooled at 15°C by a recycling water loop. The pump set-up was nearly the same system as described in section 5.3.1, except that single-side pumping was required here due to the end pump arrangement. A pump launch efficiency of 77% was observed experimentally. To set up a monolithic laser cavity, one input HR mirror was attached to the incident end-face (polished, 7mm long, as discussed in the last section) of the waveguide via the surface tension of a thin layer of fluorinated liquid, while different output coupler mirrors were attached onto the other end face with the transmission ranging from 2% to 46%.

6.3.2 Laser performance

The laser output was first detected by a silicon photodiode connected to a digital oscilloscope that was triggered by a chopper placed in the pump beam, so that the laser thresholds could then be judged by the appearance of sharp peaks in the fluorescence decay profile. The optimum launch was found by adjusting the position of the second cylindrical lens to find the lowest threshold power. The absorbed laser thresholds are listed in Table 6.1 with different transmissions of the output couplers.

Table 6.1 Absorbed pump power threshold with different output coupler transmissions.

Output coupler transmission at 1.06μm (%)	Absorbed laser threshold (W)
2.00	7.44
4.75	7.97
12.86	8.32
24.30	11.80
46.07	21.54

After the focussing optical system was fully optimised by achieving optimal laser thresholds, the pump power was increased to measure the laser slope efficiency. It should be noted that some difficulties in holding the coupling mirrors were encountered by simply using the fluorinated fluid, as the end-pump configuration inevitably lets the pump beam pass through the laser cavity mirrors and thus dries out the liquid very fast, especially at high pump powers. This problem can be solved by either getting the waveguide end faces coated or adopting the side-pump configuration as described in the last two chapters. Due to this reason, only one complete set of laser output against absorbed pump power was obtained, with an output coupler of 12.86% transmission ($R_{oc} = 0.8714$) at the laser wavelength of 1.06μm.

As shown in Fig. 6.3, the last point was very unstable when the record was taken and it was when the incident coupling mirror actually dropped in just a few seconds. The 5mm length of the waveguide is approximately one absorption length, as confirmed by the launch efficiency measurements. Given the absorption efficiency and the launch efficiency, a slope efficiency of 11.2% was obtained with respect to absorbed power, which is found to be lower than the Ti:sapphire pumping results [4] with the same waveguide, possibly due to a poorer overlap of the pump and the laser modes.

The beam profile of the laser output was recorded by a CCD camera. Since higher pump power would lead to saturation of the camera and also overheating of the filters that were used to block the pump beam and reduce the laser output power, this beam profile had to be obtained at a low level of pump power close to laser threshold. As shown in Fig. 6.4, the laser output was highly multimode, as expected.

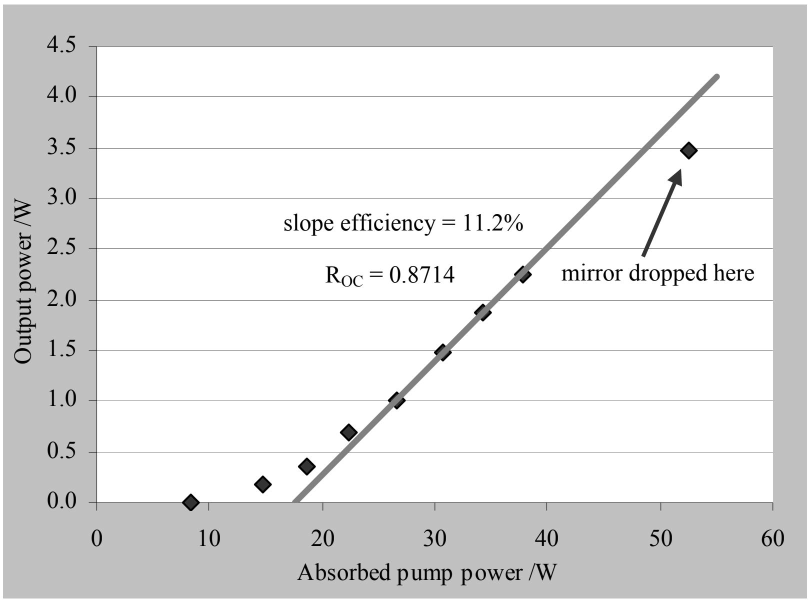

Figure 6.3 The 50µm Nd:GGG PLD waveguide laser output power versus absorbed pump power by diode-stack end pumping with a R$_{oc}$=0.8714 output coupler.

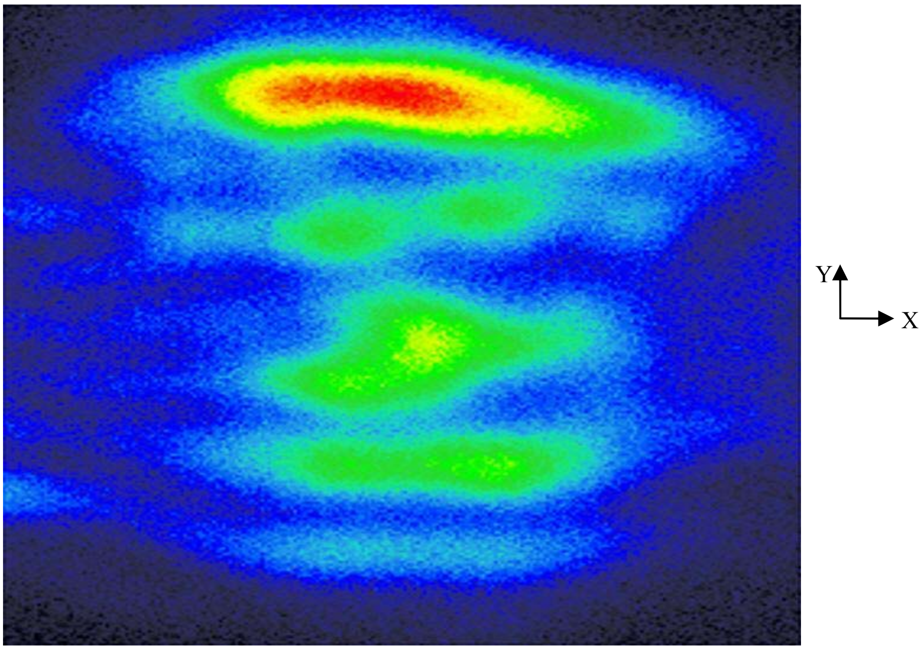

Figure 6.4 Output beam profile of the 50µm Nd:GGG PLD waveguide laser pumped by a three-bar diode stack.

6.3.3 Discussion

Based on the laser threshold results listed in Table 6.1, a Findlay-Clay plot can be drawn, which produces a propagation loss of 0.79dBcm^{-1} (see Fig. 6.5) for the waveguide, which seems much higher than the propagation loss obtained by Ti:sapphire pumping (~0.37dBcm^{-1}) for the same waveguide. However, it should be taken into account that the laser thresholds were measured at very narrow and selected places along the waveguide width to yield the minimum value, while diode pumping gave an average loss across nearly the whole width of the waveguide. Furthermore, due to the fact that the end-pumping is not an ideal solution in this case, the effective loss will be increased due to the poor contact of the mirror on the end face. Thus the 0.79dBcm^{-1} can be taken as an upper limit of this waveguide propagation loss.

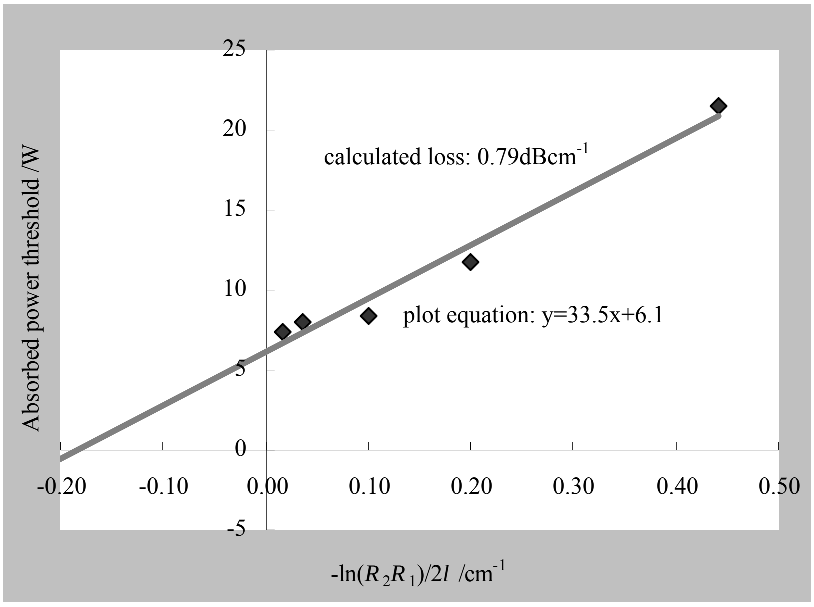

Figure 6.5 Findlay-Clay plot according to the laser threshold measurements of the 50μm Nd:GGG PLD waveguide laser, to estimate the propagation losses.

6.4 Multimode interference and self-imaging

6.4.1 Theory

As can be concluded from the operation of diode-pumped waveguide lasers presented in this thesis, an often-unavoidable solution leading to higher power lasers is to increase the thickness of the waveguide core, to couple more pump power into the waveguide. However, this usually comes at the cost of multimode propagation and laser output. To solve this problem, one interesting technique that can be used is multimode interference (MMI), based on the self-imaging principle, which has lent itself very well to the telecommunication industry [5, 6], making $N \times M$ couplers and power splitters, etc. With MMI, thick multimode planar waveguides can be made into amplifiers to generate high powers with excellent beam quality.

According to a definition given by Soldano and Pennings [7], ***self-imaging is a property of multimode waveguides by which an input field profile is reproduced in single or multiple images at periodic intervals along the propagation direction of the guide***. The images occur periodically along a waveguide as a result of multimode interference. The possibility of using the effect of self-imaging in planar waveguides was first suggested by Bryngdahl in 1973 [8] and then explained in more details by Ulrich in 1975 [9]. Self-imaging can occur in a symmetric planar waveguide, with a period of length L_{SI}, which should satisfy [10]

$$L_{SI} = \frac{4nD^2}{\lambda} \tag{6.1}$$

where n is the refractive index of the waveguide core, D is the waveguide thickness, and λ is the wavelength of the light guided into the waveguide.

According to equation (6.1), for a 50μm-thick Nd:GGG waveguide, for instance, the length over which self-imaging occurs is 18.4mm with a wavelength of 1.06μm, which can be theoretically plotted using the BPM software Prometheus introduced in section 3.2.3, as shown in Fig. 6.6. It can be seen that the first re-image of the input field profile happens at the position of $L_{SI}/4$, 4.6mm from the input-face in this case, given an axially symmetric input profile. This can significantly reduce the whole length required for the waveguide, and therefore provide a more compact geometry.

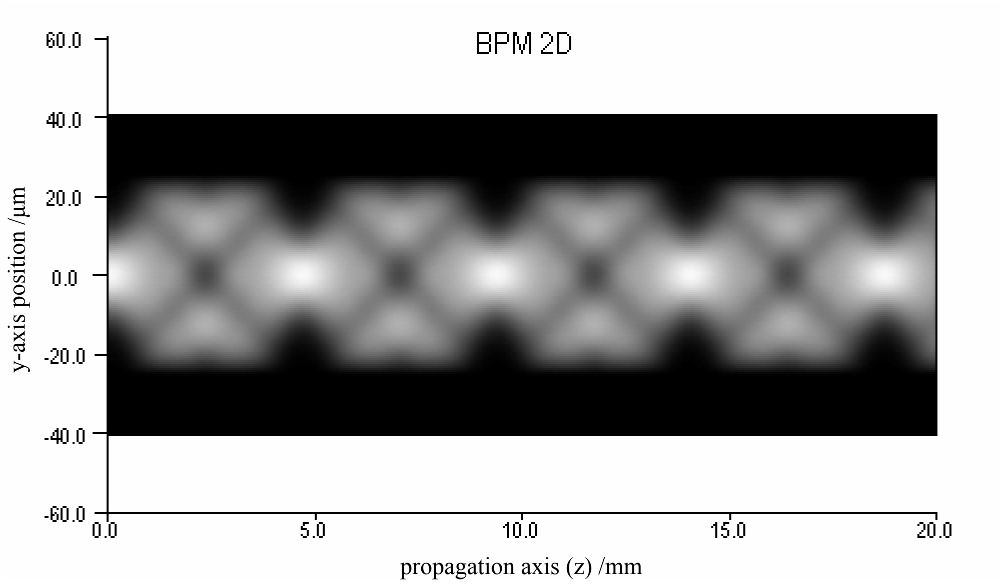

Figure 6.6 Theoretical plot for the field amplitude contours of a self-imaging multimode symmetric step-index Nd:GGG/YAG waveguide of depth 50μm, with an axially symmetric input beam.

6.4.2 Experimental characterisation

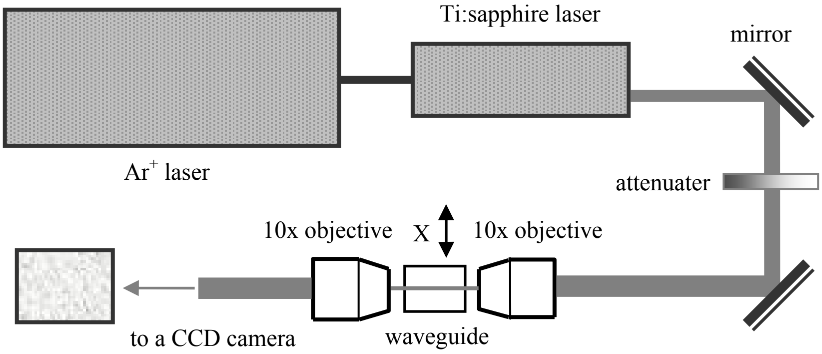

Figure 6.7 Schematic of the experimental set-up of the self-imaging effect observing.

As mentioned in Section 6.1, a Nd:GGG film was fabricated with a YAG capping layer to observe the effect of self-imaging in a symmetric waveguide structure. The Nd:GGG film was first face-polished at a slight angle before deposition of the YAG capping layer, thus to allow different waveguide thicknesses to be tested in one device. The average film thickness was about 27μm after polishing. The sample end faces were also polished at a slight angle to allow certain range of freedom with experimental adjustment to satisfy equation (6.1), after the deposition of the YAG capping layer.

A Ti:sapphire laser beam (pumped by an Ar^+ laser) was used to test the self-imaging properties of the waveguide. The experimental set-up is shown in Fig. 6.7. First of all, the Ti:sapphire laser beam was focussed tightly with a 10x microscope objective to make sure that highly multimode propagation took place in the waveguide, after which another 10x microscope objective was used to roughly collimate the output beam. The positions of both objectives can be adjusted by their individual translation stage. To observe the self-imaging effect, the launch position was changed in the x-axis so that the beam propagated through different thicknesses across the waveguide. In addition, the wavelength of the Ti:sapphire laser was also tunable. Hence, by varying these parameters in equation (6.1), different output profiles of the transmitted Ti:sapphire laser beam were obtained, and at certain points the self-imaging effect could be observed.

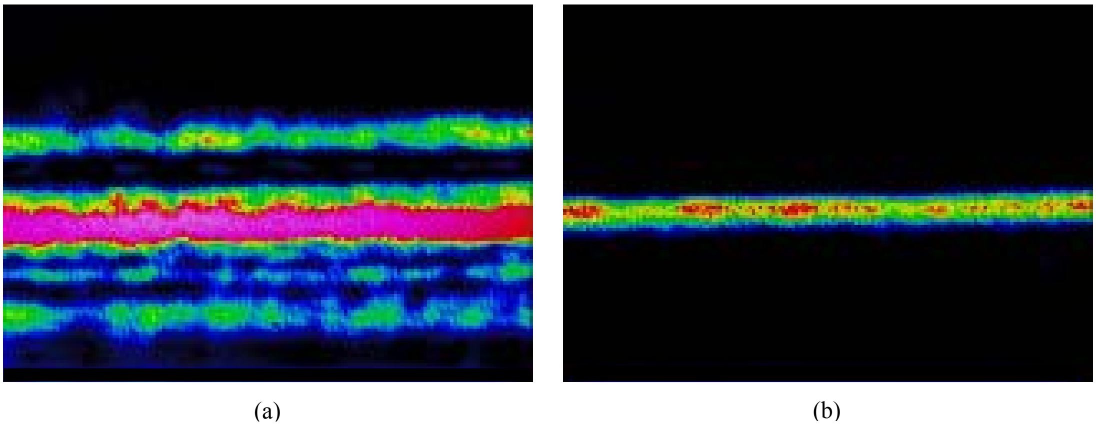

(a) (b)

Figure 6.8 Beam profile of (a) multimode propagation through the Nd:GGG waveguide, and (b) self-imaging propagation through the waveguide when the propagation parameters satisfied the self-imaging condition.

As shown in Fig. 6.8, both of the examples were obtained with a CCD camera, (a) when the parameter combination didn't satisfy the condition of self-imaging, resulting in multimode beam output; and (b) when the condition for self-imaging was qualified, which led to single-mode output in the guided direction. Meanwhile, it should be noted that a launched spot size of 6μm in diameter was reproduced (in terms of the self-imaged guided direction) at the output face.

6.5 Summary

As an initial demonstration, a diode-stack end-pumped 50μm-thick Nd:GGG PLD waveguide laser was presented with a slope efficiency of 11.2% with respect to the absorbed pump power. Double-sided side pumping could not be undertaken due to a problem of cracking encountered during the polishing stage of the waveguide fabrication. Nevertheless, the launch efficiency of ~80% with this waveguide shows good agreement with the requirement of a 50μm waveguide to operate with the three-bar diode stack pumping efficiently from section 5.2 and potential for multilayer structures if waveguides that can endure proper polishing without cracking can be produced.

As expected, the effect of self-imaging was observed with a 27μm Nd:GGG PLD waveguide with a YAG capping layer, which provides an alternative as to spatial mode control in high-power planar waveguide lasers.

6.6 References

[1] T. C. May-Smith, C. Grivas, D. P. Shepherd, R. W. Eason, and M. J. F. Healy, "Thick film growth of high optical quality low loss (0.1 dBcm-1) Nd:$Gd_3Ga_5O_{12}$ on $Y_3Al_5O_{12}$ by pulsed laser deposition," Applied Surface Science, vol. 223, pp. 361-371, Feb 29 2004.

[2] C. Grivas, T. C. May-Smith, D. P. Shepherd, and R. W. Eason, "Laser operation of a low loss (0.1 dB/cm) Nd : $Gd_3Ga_5O_{12}$ thick (40 μm) planar waveguide grown by pulsed laser deposition," Optics Communications, vol. 229, pp. 355-361, Jan 2 2004.

[3] S. J. Barrington, T. Bhutta, D. P. Shepherd, and R. W. Eason, "The effect of particulate density on performance of Nd:$Gd_3Ga_5O_{12}$ waveguide lasers grown by pulsed laser deposition," Optics Communications, vol. 185, pp. 145-152, Nov 1 2000.

[4] T. C. May-Smith, "Pulsed laser deposition of thick multilayer garnet crystal films for waveguide laser devices," in Optoelectronics Research Centre, Ph.D Thesis Southampton: University of Southampton, 2005.

[5] T. Niemeier and R. Ulrich, "Quadrature outputs from fiber interferometer with 4x4 coupler," Optics Letters, vol. 11, pp. 677-679, Oct 1986.

[6] J. M. Heaton, R. M. Jenkins, D. R. Wight, J. T. Parker, J. C. H. Birbeck, and K. P. Hilton, "Novel 1-To-N way integrated optical beam splitters using symmetrical mode mixing in GaAs/AlGaAs multimode waveguides," Applied Physics Letters, vol. 61, pp. 1754-1756, Oct 12 1992.

[7] L. B. Soldano and E. C. M. Pennings, "Optical multimode interference devices based on self-imaging - Principles and applications," Journal Of Lightwave Technology, vol. 13, pp. 615-627, Apr 1995.

[8] Bryngdahl.O, "Image formation using self-imaging techniques," Journal Of The Optical Society Of America, vol. 63, pp. 416-419, 1973.

[9] R. Ulrich and G. Ankele, "Self-imaging in homogeneous planar optical-waveguides," Applied Physics Letters, vol. 27, pp. 337-339, 1975.

[10] H. J. Baker, J. R. Lee, and D. R. Hall, "Self-imaging and high-beam-quality operation in multi-mode planar waveguide optical amplifiers," Optics Express, vol. 10, pp. 297-302, Mar 25 2002.

Chapter 7

Conclusions and future work

7.1 Conclusions

This thesis presents research work towards high-average-power diode-pumped planar waveguide lasers, which includes both introductory (Chapter 1 and 2) and experimental (chapter 3 to 6) parts.

7.1.1 Conclusions of the introductory chapters

With an overview of the academic publications with reference to the development of diode-pumped planar waveguide lasers, Chapter 1 described: (1) some general essential issues of building up efficient high-power diode-pumped solid-state lasers such as the pump source, laser medium and thermal problems; and more specifically (2) the key parameters of developing compact and high beam quality diode-pumped planar waveguide lasers, including waveguide fabrication and pump schemes. With regards to these main considerations, their experimental application can be found in later chapters, as summarized in Table 7.1.

Chapter 2 provided theoretical foundations for the whole project and specific discussions and solutions related to later experimental work, which included predicting and analyzing laser performances, characterising laser beam quality of both pump source and laser output, overcoming thermal problems especially when associated with high-power diode pumping, and finally studying the two basic waveguide structures (asymmetric slab waveguide and graded-index waveguide) that are applied in this work.

Table 7.1 The key parameters applied in the experimental chapters (Chapter 3 – 6) relating to the main considerations for developing a high-average-power planar waveguide laser that were introduced in Chapter 1.

Main considerations for developing a high-average-power planar waveguide laser	**Chapter 3**	**Chapter 4**	**Chapter 5**	**Chapter 6**
Pump source	Ti:sapphire, broad-stripe diode	Diode bar	Diode stack	Diode stack
Laser medium	Nd:BK7	Nd:YAG	Nd:YAG Yb:YAG	Nd:GGG
Cooling method	Conductive cooling	Conductive cooling	Water cooling	Water cooling
Waveguide fabrication	Ion exchange	Direct bonding	Direct bonding	Pulsed laser deposition
Pump scheme	End pumping	Side pumping	Side pumping	End pumping

7.1.2 Conclusions of the experimental chapters

In Chapter 3, ion-exchanged tapered waveguides were investigated to assess their compatibility with diode pumping and the performance of linear and parabolic tapers were compared, with fast taper expansion rates ($\alpha = 2$) to widths of 175μm to 250μm. The linear tapers maintained stable laser performance with independence of the taper width, while the parabolic tapers showed a remarkable degradation in both laser threshold and slope efficiency for larger guiding sizes. With further calculations, the additional round-trip loss γ over the background propagation loss of the ion-exchanged waveguides was compared between the two types of the tapers. A small and consistent γ of ≤ 1.4dB was found for the linear tapers up to the maximum taper widths of 250μm, whereas the additional loss γ could be over 10dB for the wider parabolic tapers. The low-loss nature of the linear tapers to widths of 250μm suggests an adiabatic quality and their ability to operate with high-average-power broad-stripe diode pumping, which should be of high interests for 1-Watt-level integrated-optics laser sources. As an initial demonstration, a broad-stripe diode-pumped tapered-waveguide laser with single-mode output was reported, which produced output power of nearly 100mW, and further improvements leading to output power of >0.5W is very plausible with this laser system.

In Chapter 4, we used two diode bars with a total power of 58W to pump a 30μm-thick Nd:YAG double-clad planar waveguide, with the attempt to achieve spatial mode control in both axes of the waveguide plane. Fundamental-mode operation was expected in the guided axis by gain mode selection through uniform doping of a central portion of 67% (20μm) of the full waveguide aperture. In the non-guided axis, however, the output spatial mode could be controlled by expanding the fundamental mode using an extended cavity, which consisted of two cylindrical lenses and a plane output mirror. Multimode output power larger than 10W was obtained from the waveguide, at a slope efficiency of 56% with respect to absorbed pump power. When the external cavity length was optimised for high beam quality, M^2 values of 1.1 (guided axis) by 2.8 (non-guided axis) were obtained and the slope efficiency was reduced to 33%, which was in good agreement with the theoretical expectation with regard to the spatial overlap of the uniformly pumped waveguide and the near-Gaussian lasing mode. The improvement in the non-guided axis beam quality has shown good prospects in future research, and scaling of the output power was expected by high-power diode-stack pumping.

In Chapter 5, a side-pumping scheme with higher-power diode stacks as the pump source was explored, with the large-mode-area double-clad planar waveguides available. An optical pump system was developed, with the aid of both computer modelling and experimental measurements, to couple the diode-stack pump beam ($M_y^2 \approx 20$ in the fast axis) into the high- NA (0.46) YAG/sapphire waveguide discussed in Chapter 4, preferably with a 50μm core in this case. Experimentally, a diode-stack side-pumped Nd:YAG planar waveguide laser was reported to produce 58W of output power with a slope efficiency of 62% with respect to absorbed power, in good agreement with theoretical expectation. Unfortunately, the upper sapphire cladding layer cleanly detached from the rest of the waveguide at the incident-power level of ~320W, and this left the beam quality of the laser output unmeasured.

After re-polishing the damaged end-faces of the waveguide, a stable extended cavity was set up following the concept of spatial mode control using a telescopic resonator discussed in Chapter 4, but the aim was to produce a near-symmetric shaped output beam this time. Nearly 20W was obtained with an incident pump power of 272W but this performance could not last due to waveguide damage. With the extended cavity, a minimum experimental M^2 value of ~7 in the non-guided axis was obtained, although the experiments had to be stopped as a result of further waveguide damage. To predict power scalability of this laser system, a 50μm Yb:YAG waveguide laser was modelled. Theoretically, ~140W of laser output power could be obtained with incident power of 360W from two diode stacks, and it could be expected that the generated heat be effectively removed by double-sided water cooling, which would only yield a maximum temperature of 54°C in the waveguide core. Therefore, it can be concluded that scaling of laser output to very high powers is very plausible for diode-stack side-pumped planar waveguide lasers.

In Chapter 6, pulsed-laser-deposited planar waveguides were investigated as a flexible alternative in high-power diode-stack-pumped laser systems. Since double-sided side pumping was not possible with the sample due to a cracking problem encountered during the waveguide polishing process, the experiments were carried out by end-pumping a 50μm-thick Nd:GGG PLD waveguide with a 180W diode stack. A launch efficiency of ~80% was achieved with the pump system used in Chapter 5 and a slope efficiency of 11.2% was obtained with respect to absorbed pump power. As an initial demonstration, this first diode-stack-pumped PLD waveguide laser showed good capability of PLD waveguides to operate with very-high-power pumps. Progress could be expected from both improved fabrication procedures and multilayer-structure waveguides that can take full advantage of the stack pumping. Furthermore, the effect of self-imaging was observed with a 27μm Nd:GGG PLD waveguide, which demonstrates the potential of another way of spatial mode control in high-power planar waveguide laser systems.

7.2 Future work

7.2.1 High-brightness >100W planar waveguide lasers

Since the 30μm double-clad waveguide used in Chapter 5 was not the ideal design for the 3-bar diode-stack pumping, further experiments are required once a proper 50μm YAG/sapphire double-clad waveguide is made according to the design given in section 5.4. The GGG/YAG PLD waveguides, with similar losses and even higher NAs (0.73), offer a good alternative for high-power diode-stack pumping and can be grown in-house with ORC facilities. For laser operation, the first step is to develop a CW waveguide oscillator operating at >100W using a monolithic cavity with directly-coated end faces. It can be expected that the output from this monolithic cavity would be diffraction-limited in the guided axis but highly multimode in the non-guided plane. In order to obtain near-diffraction-limited operation in both axes, a stable extended cavity is then required, preferably to produce a near-symmetric shaped laser output beam using a spherical-and-cylindrical lens combination, as discussed in section 5.3.3.

Further steps can be taken to enhance the laser performance. The use of zigzag lasing paths, for example, can fully extract the available power and improve the spatial overlap of the cavity mode and excited region, which then leads to higher extraction efficiencies and better non-guided-axis beam quality. Unstable resonators can be another approach, which can more easily reach the large mode sizes required in the non-guided plane, as developed in face-pumped waveguides lasers [1]. Gain limiting effects such as amplified spontaneous emission (ASE) and parasitic lasing will probably define the final configurations investigated.

7.2.2 Towards 1kW planar waveguide lasers

There are ways to scale the output power of the 100W-level waveguide lasers discussed above, by increasing the thickness of the waveguide core to allow pumping by the one-dimensional diode-stack with more bars, or by increasing the length of the waveguide and building a two-dimensional diode-array pump source. Although the first method can maintain the usual overall size of the waveguide, it has every possibility to cause serious thermal problems with the increased pump power, owing to the great thermal load in a relatively small device. The second method has the advantage of keeping the waveguide as thin as possible and allows the use of coupling optics of the same design that is used in earlier work. However, even this method can not be a realistic way to scale the laser output power to kW levels from a single device, because it would require waveguides of ~10cm in length, which would push the capabilities of the waveguide fabrication techniques. To obtain a design for a 1kW planar waveguide laser, one possible way is to use separate gain modules in a master oscillator - power amplifier (MOPA) configuration, which can in turn be aided by increasing the waveguide length reasonably and the use of two-dimensional diode arrays.

7.3 References

[1] J. R. Lee, H. J. Baker, G. J. Friel, G. J. Hilton, and D. R. Hall, "High-average-power Nd:YAG planar waveguide laser that is face pumped by 10 laser diode bars," Optics Letters, vol. 27, pp. 524-526, Apr 1 2002.

Appendix A

Publications

A.1 Journal articles

C. Li, J. I. Mackenzie, **J. Wang**, and D. P. Shepherd, “A diode-bar side-pumped waveguide laser with an extended stable cavity for spatial mode control”, *Optics Communications,* vol. 226, pp. 317-321, Oct 15 2003.

S. J. Hettrick, **J. Wang**, C. Li, J. S. Wilkinson, and D. P. Shepherd, “An experimental comparison of nonlinear and parabolic tapered waveguide lasers and a demonstration of broad-stripe diode pumping”, *IEEE Journal of Lightwave Technology,* vol. 22, pp. 845-849, Mar 2004.

A.2 Conferences

J. I. Mackenzie, C. Li, **J. Wang**, and D. P. Shepherd, “Multi-watt diffraction-limited CW and Q-switched diode-end-pumped double-clad waveguide lasers”, *CLEO/Europe EQEC 2003,* Munich, 22-27 Jun 2003, CL1-1-THU.

S. J. Hettrick, **J. Wang**, C. Li, J. S. Wilkinson, and D. P. Shepherd, “An experimental comparison of linear and parabolic tapered waveguide lasers”, *ECIO 2003,* Prague, 2-4 Apr 2003, ThA2.5.

C. Grivas, T. C. May-Smith, **J. Wang**, M. S. B. Darby, D. P. Shepherd, and R. W. Eason, "A low-loss PLD fabricated garnet planar waveguide laser", *EPS-QEOD Europhoton Conference,* Lausanne, 29 Aug-3 Sep 2004, ThD2.

J. Wang, J. I. Mackenzie, and D. P. Shepherd, "An efficient high-power waveguide laser side-pumped by two diode-stacks", *ECIO 2005,* Grenoble, 6-8 April 2005, ThPo21.

J. Wang, J. I. Mackenzie, and D. P. Shepherd, "A diode-stack side-pumped waveguide laser", *CLEO/QELS 2005,* Baltimore, 22-27 May 2005, CTh16.

T. C. May-Smith, **J. Wang**, J. I. Mackenzie, D. P. Shepherd, and R. W. Eason, "Diode-pumped garnet crystal waveguide structures fabricated by pulsed laser deposition", *CLEO/QELS 2006,* Long Beach, California, 21-25 May 2006, CMFF7.